January 2016

MITIGATION OF DC-LINK VOLTAGE OSCILLATIONS CAUSED BY RESOLVER ERROR IN AN ELECTRIC VEHICLE DRIVETRAIN

Ayesha Sayed
Purdue University

Graduate School Form
30 Updated 12/26/2015

PURDUE UNIVERSITY
GRADUATE SCHOOL
Thesis/Dissertation Acceptance

This is to certify that the thesis/dissertation prepared

By Ayesha Sayed

Entitled

MITIGATION OF DC-LINK VOLTAGE OSCILLATIONS CAUSED BY RESOLVER ERROR IN AN ELECTRIC VEHICLE DRIVETRAIN

For the degree of Master of Science in Electrical and Computer Engineering

Is approved by the final examining committee:

Dionysios C. Aliprantis
Chair

Gregory M. Shaver

Steven D. Pekarek

To the best of my knowledge and as understood by the student in the Thesis/Dissertation Agreement, Publication Delay, and Certification Disclaimer (Graduate School Form 32), this thesis/dissertation adheres to the provisions of Purdue University's "Policy of Integrity in Research" and the use of copyright material.

Approved by Major Professor(s): Dionysios C. Aliprantis

Approved by: Venkataramanan Balakrishnan 12/5/2016

Head of the Departmental Graduate Program Date

MITIGATION OF DC-LINK VOLTAGE OSCILLATIONS CAUSED BY RESOLVER ERROR IN AN ELECTRIC VEHICLE DRIVETRAIN

A Thesis

Submitted to the Faculty

of

Purdue University

by

Ayesha Sayed

In Partial Fulfillment of the

Requirements for the Degree

of

Master of Science in Electrical and Computer Engineering

December 2016

Purdue University

West Lafayette, Indiana

To my parents.

ACKNOWLEDGMENTS

I would like to express my gratitude towards Prof. Dionysios Aliprantis, the major advisor of my Masters thesis for guiding my research with his ingenious thinking. I highly appreciate all his contributions in making this research valuable.

I would also like to thank Prof. Steve Pekarek and Prof. Gregory Shaver for serving as members of my graduate advisory committee.

I would especially like to thank Michael Hayashi for his good advice. Thanks to my friends Harshita, Alpana and Manoj for making this journey memorable.

I am indebted to my parents and my brother for supporting me in all my pursuits.

This project is sponsored by John Deere. I would like to thank Dr. Long Wu, Dr. Sumit Dutta and Guozhen Zhou for their technical assistance throughout and further offering me an opportunity to join their team as an intern. The experimental tests would not have been possible without their aid. Last, but not the least, I thank Dr. Scott Johnson for his insightful comments during my internship at John Deere in Summer 2016.

TABLE OF CONTENTS

Page

LIST OF TABLES

LIST OF FIGURES

NOMENCLATURE

θ_r	actual rotor position in electrical radians
$\hat{\theta}_r$	measured electrical rotor position (from resolver) in electrical radians
θ_{r0}	equilibrium electrical rotor position (linear function of time) in electrical radians
$\delta\theta_r = \theta_r - \theta_{r0}$	deviation of rotor position from equilibrium value (due to rotor shaft oscillation)
$\delta\hat{\theta}_r = \hat{\theta}_r - \theta_{r0}$	deviation of estimated rotor position from equilibrium value
$e_\theta = \hat{\theta}_r - \theta_r$	resolver error in electrical radians
i_a, i_b, i_c	actual stator phase currents
i_q, i_d	actual q- and d-axis stator current (in rotor reference frame)
i_q^*, i_d^*	commanded q- and d-axis stator current (in rotor reference frame)
$\hat{i}_q, \hat{i}_d$	estimated q- and d-axis current obtained using $\hat{\theta}_r$ in Park's transformation
i_{q0}^*, i_{d0}^*	commanded q- and d-axis stator current at equilibrium
$\delta i_q^* = i_q^* - i_{q0}^*$	deviation of commanded q-axis current from equilibrium value
$\delta i_d^* = i_d^* - i_{d0}^*$	deviation of commanded d-axis current from equilibrium value
$\delta i_q = i_q - i_{q0}$	deviation of actual q-axis current from equilibrium value
$\delta i_d = i_d - i_{d0}$	deviation of actual d-axis current from equilibrium value
$\delta\hat{i}_q = \hat{i}_q - \hat{i}_{q0}$	deviation of estimated q-axis current from equilibrium value
$\delta\hat{i}_d = \hat{i}_d - \hat{i}_{d0}$	deviation of estimated d-axis current from equilibrium value

v_{q0}^*, v_{d0}^*	commanded q- and d-axis stator voltage at equilibrium
v_q, v_d	actual q- and d-axis stator voltage (inverter output)
$\delta v_q^* = v_q^* - v_{q0}^*$	deviation of commanded q-axis voltage from equilibrium value
$\delta v_d^* = v_d^* - v_{d0}^*$	deviation of commanded d-axis voltage from equilibrium value
$\delta v_q = v_q - v_{q0}$	deviation of actual q-axis voltage from equilibrium value
$\delta v_d = v_d - v_{d0}$	deviation of actual d-axis voltage from equilibrium value
ω_r	actual electrical speed in rad/s
$\hat{\omega}_r$	estimated electrical speed in rad/s
$\delta\omega_r = \omega_r - \omega_{r0}$	deviation of rotor speed from equilibrium value (due to rotor shaft oscillation)
$\delta\hat{\omega}_r = \hat{\omega}_r - \omega_{r0}$	deviation of estimated electrical speed from equilibrium value
v_{dc0}	equilibrium dc-link voltage
$\delta v_{dc} = v_{dc} - v_{dc0}$	deviation of dc-link voltage from nominal value

ABSTRACT

Ayesha Sayed M.S.E.C.E, Purdue University, December 2016. Mitigation of DC-Link Voltage Oscillations Caused by Resolver Error in an Electric Vehicle Drivetrain. Major Professor: Dionysios Aliprantis.

Resolvers are commonly used to measure the rotor position in motor drive applications. However, manufacturing imperfections introduce a position measurement error, which manifests itself as relatively small oscillations primarily at the fundamental and second harmonic frequencies. This affects the field orientation control in machines, leading to oscillations in currents and electromagnetic torque. This research focuses on the impact of position error in a series-hybrid drivetrain architecture. In this topology, substantial oscillations in dc-link voltage are induced, which are further exacerbated by reducing the dc-link capacitance in a bid to lower the overall inverter size and weight.

This work sets forth various methods to mitigate the aforementioned dc-link oscillations based on control modifications. To this end, a linearized small-signal detailed model of the drivetrain is developed first to support the analysis of the phenomenon. The effectiveness of these techniques is validated by analytical and experimental results.

1. INTRODUCTION

Recent advances in wide-bandgap (WBG) power semiconductor devices, such as silicon carbide (SiC) and gallium nitride (GaN) devices, have been driven by their superior properties, which include high switching frequencies, high blocking voltages, and high junction temperatures. These devices can improve the electrical and thermal performance of power electronic converters, and thus find a very promising application domain in vehicle electrification [1]. A particular outcome of increasing the switching frequency, which is most relevant for this thesis, is the benefit of reducing the capacitance of the dc link, which in turn lowers the size and weight of an inverter thereby increasing its power density.

On the other hand, sensing the rotor position of electric motors is a necessary functionality for control in a wide range of motor drive configurations. This includes permanent magnet (PM) ac traction applications, which is the particular motor type that this thesis focuses on. Resolvers are used extensively in high-performance motor drive applications due to their ability to function in harsh environments [2]. The output signals of a resolver contain absolute position information. The signals, which are modulated using a high-frequency excitation, are processed using specialized resolver-to-digital (R/D) converter circuits. Conventional tracking R/D converters operate under the assumption that ideal resolver signals are supplied to the R/D converter. However, in practice, various manufacturing imperfections in resolvers are always present, such as amplitude imbalance and imperfect quadrature. In turn, these lead to nonideal resolver signals, which induce a periodic error in position measurement [3]. This affects the field orientation control in PM machines, creating substantial oscillations on dc-link voltage.

The dc-link voltage oscillations are further amplified when the dc-link capacitance is reduced, which is the case in WBG applications. This could have several negative

effects; for instant, since other components may be powered from the dc-link in a hybrid electric vehicle, power quality issues may arise. In addition, the lifetime of the dc-link capacitor may be decreased, and the operating range of the machines may become limited. Therefore, addressing the problem of dc-link voltage oscillations is important and timely, as the automotive industry is rapidly adopting WBG devices.

1.1 Background on Resolvers

Here, we describe the basic working principle of a resolver. Subsequently, a few nonidealities in resolver manufacturing are analyzed, to understand the type of position error introduced.

Ideal Resolver Operation

The most commonly used variable reluctance (VR) resolvers do not have windings on the rotor. Their primary and secondary windings are all on the stator. Fig. 1.1 shows the rotor structure for 2, 3, and 4 lobes. The number of rotor lobes are usually set equal to the motor pole pairs, so that the induced output in secondary windings varies as a sinusoidal function of electrical rotor angle θ_r.

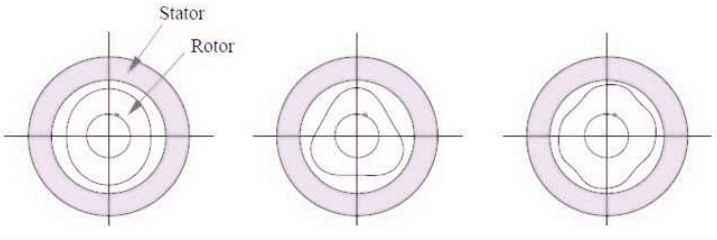

Fig. 1.1. Variable-reluctance resolver cross-sectional view, illustrating rotor lobes.

The basic principle of VR resolver is shown in Fig. 1.2. The excited primary voltage and induced secondary voltages are given by

$$V_p = V_0 \sin(\omega_c t) \tag{1.1}$$

$$V_{\sin} = KV_0 \sin(\theta_r) \sin(\omega_c t) \tag{1.2}$$

$$V_{\cos} = KV_0 \cos(\theta_r) \sin(\omega_c t) \tag{1.3}$$

where K is the transformation ratio.

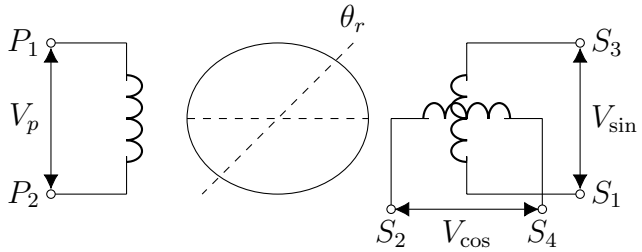

Fig. 1.2. Basic operating principle of resolver.

The induced voltages in the secondary windings are shown in Fig. 1.3 for the corresponding primary excitation. The modulated signals, which are the outputs of the resolver, are demodulated to obtain the rotor position. The tracking mechanism is explained in the block diagram shown in Fig. 1.4 where the modulated signals $V_{\sin}$ and $V_{\cos}$ are multiplied by $\cos\hat{\theta}_r$ and $\sin\hat{\theta}_r$ respectively and then subtracted, which results: $V_{\sin}\cos\hat{\theta}_r - V_{\cos}\sin\hat{\theta}_r = KV_0\sin(\omega_c t)\sin(\theta_r - \hat{\theta}_r)$ where $\hat{\theta}_r$ is the estimated rotor position. Demodulating the above signal using the primary signal V_p yields $KV_0\sin(\theta_r - \hat{\theta}_r)$. Generally, this signal is driven to zero using a controller to estimate the rotor position [4], [5].

Non-ideal Characteristics

The measured rotor position $\hat{\theta}_r$ deviates from the true position value θ_r due to various non-idealities [6], [7] such as the misalignment of the sensor components or

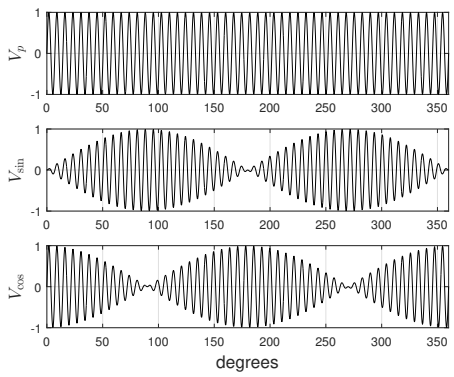

Fig. 1.3. Resolver signals.

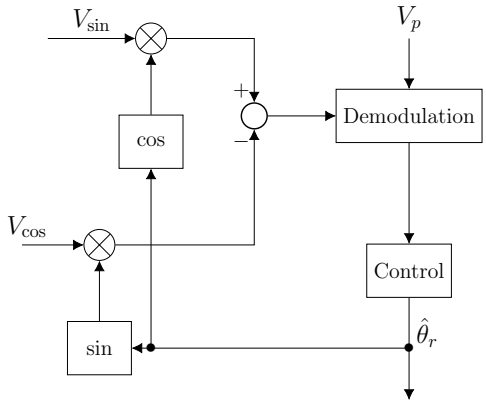

Fig. 1.4. Block diagram of resolver-to-digital converter.

manufacturing imperfections. This section sets forth a survey on the effects of non-ideal resolver signal characteristics.

1. Amplitude Imbalance: This occurs when the two resolver output signals have different amplitudes and is caused due to unequal inductances [3]. The modulated signals are shown in Fig. 1.5. This can be modeled as follows:

$$V_{\sin} = KV_0 \sin(\theta_r) \sin(\omega_c t) \tag{1.4}$$

$$V_{\cos} = KV_0(1+\zeta) \cos(\theta_r) \sin(\omega_c t)\,. \tag{1.5}$$

Input to the demodulation block is given by

$$V_{\sin} \cos\hat{\theta}_r - V_{\cos} \sin\hat{\theta}_r = KV_0 \sin(\omega_c t)[\sin\theta_r \cos\hat{\theta}_r - (1+\zeta)\cos\theta_r \sin\hat{\theta}_r]\,. \tag{1.6}$$

The signal obtained after demodulation is $KV_0[\sin\theta_r\cos\hat{\theta}_r-(1+\zeta)\cos\theta_r\sin\hat{\theta}_r]$. Driving this signal to zero to estimate the rotor position yields,

$$\sin(\theta_r-\hat{\theta}_r)=\zeta\cos\theta_r\sin\hat{\theta}_r\,. \tag{1.7}$$

The error in position is represented as $e_\theta=\hat{\theta}_r-\theta_r$. Using the small-angle approximations $\sin e_\theta\approx e_\theta$ and neglecting higher order terms, we obtain

$$\sin(-e_\theta)=\frac{1}{2}\zeta\left[\sin(\theta_r+\hat{\theta}_r)+\sin(\hat{\theta}_r-\theta_r)\right] \tag{1.8}$$

$$e_\theta\approx-\frac{\zeta}{2}\sin 2\theta_r\,. \tag{1.9}$$

In this case, the position error is introduced at the second harmonic.

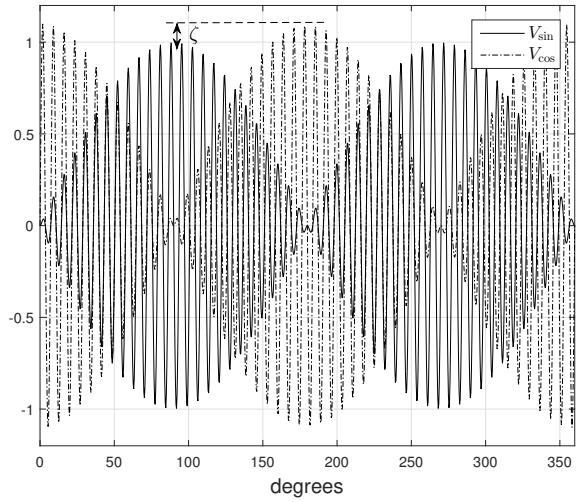

Fig. 1.5. Amplitude imbalance in resolver signals.

2. Imperfect Quadrature: This is caused when the output phases are not in perfect spatial quadrature with each other [3]. The modulated signals are shown in Fig. 1.6.

$$V_{\sin}=KV_0\sin(\theta_r)\sin(\omega_c t) \tag{1.10}$$

$$V_{\cos}=KV_0\cos(\theta_r+\xi)\sin(\omega_c t)\,. \tag{1.11}$$

Input to the demodulation block is given by

$$V_{\sin}\cos\hat{\theta}_r - V_{\cos}\sin\hat{\theta}_r = KV_0\sin(\omega_c t)[\sin\theta_r\cos(\hat{\theta}_r) - \cos(\theta_r+\xi)\sin\hat{\theta}_r] \quad (1.12)$$

The signal obtained after demodulation is $KV_0[\sin\theta_r\cos(\hat{\theta}_r) - \cos(\theta_r+\xi)\sin\hat{\theta}_r]$. Driving the demodulated signal to zero yields,

$$\sin\theta_r\cos\hat{\theta}_r = \cos(\theta_r+\xi)\sin\hat{\theta}_r\,. \quad (1.13)$$

Using the small-angle approximations $\sin\xi \approx \xi, \cos\xi \approx 1, \sin e_\theta \approx e_\theta$, we obtain

$$e_\theta \approx \frac{\xi}{2}(1-\cos 2\theta_r)\,. \quad (1.14)$$

This imperfection also introduces a second harmonic position error.

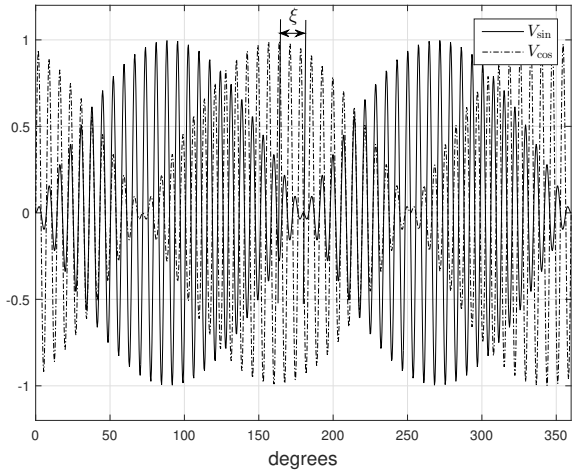

Fig. 1.6. Imperfect quadrature in resolver signals.

3. DC Offset: A dc offset occurs in the output phases either due to asymmetrical coil locations due to three layers of winding on stator tooth or occurrence of rotor eccentricity during assembly or operation. Fig. 1.7 shows the rotor eccentricity. The modulated signals are modeled as follows:

$$V_{\sin} = KV_0\left[\frac{K_1}{K} + \sin(\theta_r)\right]\sin(\omega_c t) \quad (1.15)$$

$$V_{\cos} = KV_0\left[\frac{K_2}{K} + \cos(\theta_r)\right]\sin(\omega_c t)\,. \quad (1.16)$$

In a special case when $K_1 = K_2 = K_0$, driving the output of the demodulator block to zero yields,

$$\frac{K_0}{K}(\cos\hat{\theta}_r - \sin\hat{\theta}_r) + (\sin\theta_r\cos\hat{\theta}_r - \cos\theta_r\sin\hat{\theta}_r) = 0 \tag{1.17}$$

$$\sqrt{2}\frac{K_0}{K}\cos\left(\theta_r + \frac{\pi}{4}\right) + \sin\left(\theta_r - \hat{\theta}_r\right) = 0\,. \tag{1.18}$$

Using the small-angle approximations $\sin e_\theta \approx e_\theta$,

$$e_\theta \approx \sqrt{2}\frac{K_0}{K}\cos\left(\theta_r + \frac{\pi}{4}\right). \tag{1.19}$$

This causes a position error at the fundamental.

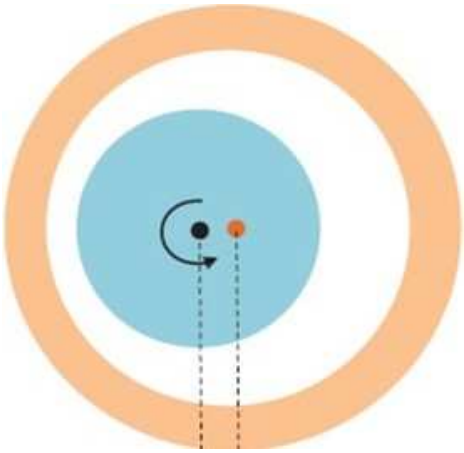

Fig. 1.7. Rotor eccentricity in resolver [8].

1.2 Literature Survey

Several compensation algorithms have been proposed to reduce the position error caused by the manufacturing imperfections in resolvers. A conventional method of compensating the position error is by using a high-resolution look-up table (LUT) [9–12]. However, a large amount of memory is required to store the data, which could be problematic in embedded applications where hardware resources are limited. The creation of the LUT may also be challenging, as each resolver will differ slightly from the next.

Efforts to compensate the non-ideal characteristics in resolver signals are also reported in the earlier works. The method proposed in [13] employs an integrating operation of the d-axis current to compute the errors caused by the amplitude imbalance and imperfect quadrature. However, this method is based on a constant d-axis current, hence it is applicable only in surface-mount PM motors. In [14], a method is introduced to reduce the torque ripple caused by only the amplitude imbalance. This method needs an additional position sensor which has no periodic position error in order to reduce the torque ripple. In [15], a method is introduced based on peak values of resolver output signals to compute the magnitude of dc offset error, amplitude imbalance and imperfect quadrature. However the technique proposed needs to be implemented in the R/D. In [16], an algorithm for compensating the errors in modulated signals of the resolver is presented. This method first demodulates the resolver signals and computes the error by comparing with the ideal signals. The coefficients to best fit these error signals are computed using the polynomial approximations based on the least mean squares. However, the ideal signals are synthesized assuming a constant speed which might not be the case in practice. Also, this method needs to be implemented in the R/D.

Also, a patent [17] was filed to compensate the position error adaptively through a controller. In the method proposed, the resolver signals are initially demodulated and normalized, then each of the signals are squared and their sum is subtracted from a constant value 1 to estimate an error factor. The non-ideal characteristic parameters in resolver such as amplitude error, phase error and dc-offset values are estimated from the error factor and subsequently compensated to obtain the corrected signals. However, this controller is to be implemented in the R/D. All the past techniques have either not eliminated all possible errors types introduced due to resolver manufacturing imperfection or have modified the R/D converter.

An other problem of VR resolvers is its complex winding structure. The asymmetrical coil structure in resolvers due to three layers of coils on each stator tooth causes a dc offset in the resolver signals. This in turn leads to an error in position es-

timation. Furthermore, output windings are usually sinusoidally distributed and the number coil turns is different from one to another, which makes the winding process more complicated. In [8], a VR resolver with nonoverlapping toothcoil windings is proposed which simplifies the manufacturing process; however, this increases an error in rotor position.

In this disseration, a technique that is simple to implement is proposed. The algorithm can eliminate the position error at any desired harmonic order, which might be introduced due to any type of manufacturing imperfection in the resolver or from R/D converter.

1.3 Thesis Outline

This work begins with a description of the series hybrid drivetrain architecture in Chapter 2. It proceeds with the development of linearized small-signal model of each subsystem in detail. Then, the state-space model of the entire system is derived by combining the models of each subsystem. Two state-space models are presented; one considering the position error as a state and the other considering the position error as an input disturbance. Transfer functions are derived for each of the input disturbances to the dc-link voltage from the state-space models. Lastly, this chapter discusses the selection of gains in the current regulator.

Numerical results illustrating the impact of the input disturbances on the dc-link voltage are presented in Chapter 3. This includes the frequency response plots for each of the disturbances for both the models and also the impact of position error and slot harmonics over the operating range.

In Chapter 4, the proposed mitigation strategies to reduce the dc-link voltage oscillations are set forth. Each of the methods is supported by the simulation results obtained from the derived small-signal model and also by experimental results.

2. SYSTEM DESCRIPTION AND SMALL-SIGNAL MODEL

The structure of a conventional series-hybrid drivetrain is shown in Fig. 2.1. The system described here has four interior permanent magnet (IPM) machines, converters, and dc-link. The prime mover (Machine 1) is speed-controlled. Machine 2 (generator drive) generates the electrical power necessary to maintain the dc-link at constant voltage. Machine 3 (traction drive) absorbs electrical power from the dc-link to provide the desired torque demanded by the load. The load (Machine 4) is running in speed control mode. The energy from the machines to the dc-link is supplied/absorbed via the converters. The analysis herein is based on modeling Machine 2, Machine 3, and the dc-link. A block diagram of these machines (with their controller) along with the dc-link is shown in Fig. 2.2. Note that a subscript '2' and '3' represents the variables corresponding to Machine 2 and Machine 3 respectively. This model analyzes the impact of possible disturbance sources on this system by formulating the transfer functions with dc-link voltage variation as output and each of the disturbances as inputs.

A linearized small-signal model is set forth to analyze the drivetrain system. The inputs to the small-signal model represent various external disturbances (e.g., a mechanical shaft oscillation). The model outputs the dc-link voltage oscillation around its nominal value. The system equations are linearized around a given steady-state operating point, which is defined in terms of (i) torque and speed of the motor, and (ii) speed of the generator. This equilibrium point corresponds to an ideal case when there is neither resolver error nor any other disturbances. The equilibrium values at any particular operating point are computed using an initialization script. A pseudocode of this script is included in the Appendix A.

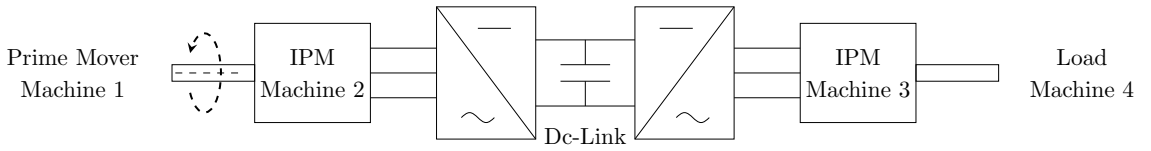

Fig. 2.1. System architecture.

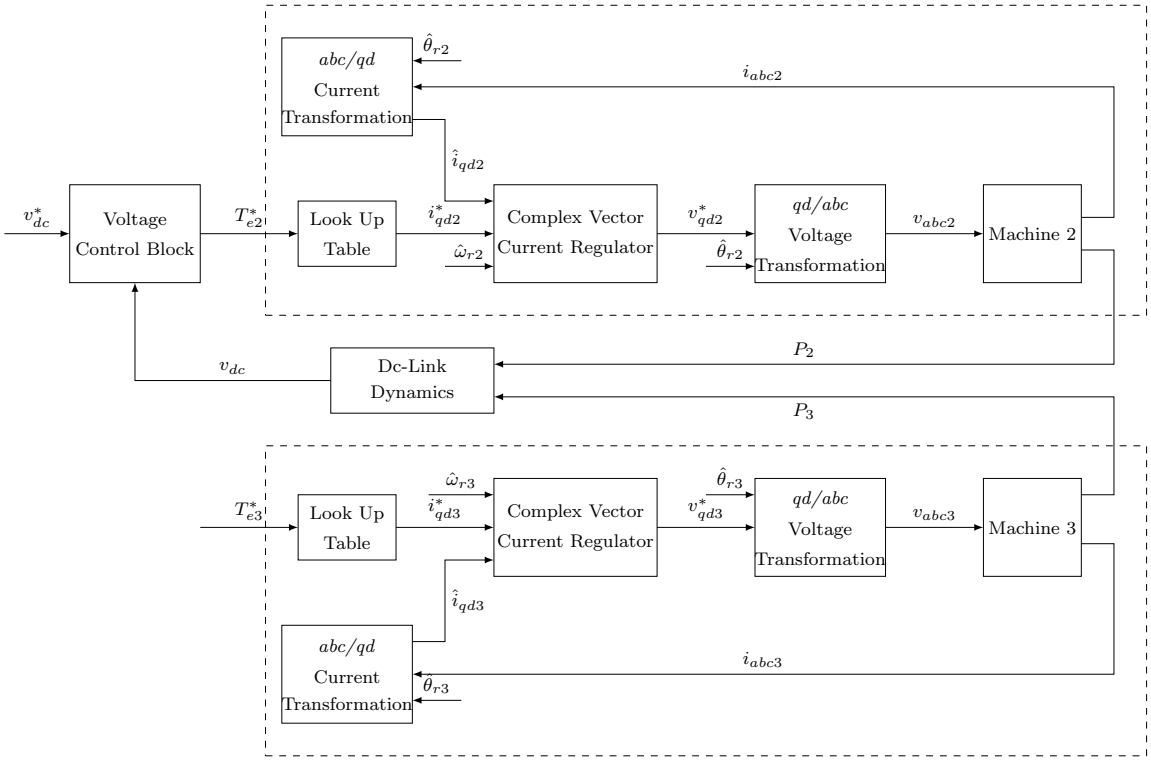

Fig. 2.2. Block diagram of detailed model.

The following notation is used throughout this thesis. The perturbation of any variable x around its equilibrium point is defined as $\delta x = x - x_0$, i.e., the subscript '0' represents equilibrium value. In general, equilibrium values will be constant. A notable exception to this is the rotor angle, which at equilibrium is a linear function of time (assuming constant rotor speed). The position error is represented as e_θ, which is defined as the deviation of estimated rotor position ($\hat{\theta}_r$) from actual rotor position

(θ_r), i.e., $e_\theta = \hat{\theta}_r - \theta_r$. Variables with a hat, e.g., $\hat{x}$, denote estimated (e.g., directly measured) values. Variables with an asterisk, e.g., x^*, denote commanded values.

The controller of each motor comprises: i) a transformation of *abc* currents to *qd*, ii) a CVCR (Complex Vector Current Regulator) block, which outputs commanded *qd* voltages, iii) a transformation of commanded *qd* voltages to *abc*. The three phase voltages are then applied to the machine through an inverter. The inverter is assumed to be ideal. Switching is not modeled, i.e., the inverter is modeled by an average-value model.

In what follows, the various subsystems that have time-domain dynamics are linearized and modeled in canonical form, e.g., as $\dot{x} = Ax + Bu$, $y = Cx + Du$ (although minor variations to this notation will be introduced). As usual, u represents input, y represents output, and x represents the state. Some subsystems are purely algebraic, and are modeled as, e.g., $y = Fu$.

2.1 DC-Link Dynamics

The dc-link is modeled as an ideal capacitor C in parallel with a (small) admittance G, which is physically present as a "bleeder" resistance. The equivalent series resistance of the capacitor is neglected. Since the machine powers P_2 and P_3 are defined as positive when power flows into the machine terminals, we have

$$-\left(\eta P_2 + \frac{P_3}{\eta}\right) = v_{dc} i_{dc} = C v_{dc} \frac{d}{dt} v_{dc} + G v_{dc}^2 \tag{2.1}$$

where i_{dc} is the total current flowing through the capacitor and parallel admittance, and where $\eta < 1$ is the efficiency of the inverter, which is assumed to be constant.[1]

Expressing the dynamics in the neighborhood of an equilibrium point, yields

$$-\left[\eta(P_{20} + \delta P_2) + \frac{P_{30} + \delta P_3}{\eta}\right] = C(v_{dc0} + \delta v_{dc})\left(\frac{d}{dt} v_{dc0} + \frac{d}{dt}\delta v_{dc}\right) + G(v_{dc0} + \delta v_{dc})^2 . \tag{2.2}$$

[1]Efficiency is considered equal for both converters (for simplicity).

To linearize, we neglect the second-order terms $\delta v_{dc}\frac{d}{dt}\delta v_{dc}$ and δv_{dc}^2, which leads to

$$\frac{d}{dt}\delta v_{dc} = -\frac{1}{Cv_{dc0}}\left(\eta\,\delta P_2 + \frac{1}{\eta}\delta P_3\right) - \frac{2G}{C}\delta v_{dc}\,. \tag{2.3}$$

Hence, the state-space model of the dc-link is given by,

$$\frac{d}{dt}\delta v_{dc} = A_{dc}\delta v_{dc} + B_{dc}\begin{bmatrix}\delta P_2\\ \delta P_3\end{bmatrix} \tag{2.4}$$

where

$$A_{dc} = -\frac{2G}{C},\quad B_{dc} = -\frac{1}{Cv_{dc0}}\begin{bmatrix}\eta & \frac{1}{\eta}\end{bmatrix}\,. \tag{2.5}$$

2.2 Voltage Control Block

The voltage control block is present only in the generator (machine 2). This block performs proportional-integral (PI) control of the dc-link voltage, or more precisely, of the capacitor energy. Here, z_v denotes the integral output of the PI controller, which is the only state of the voltage control subsystem.

Two different versions of a voltage controller are set forth. The PI controller in the first version outputs a torque command, whereas in the second version it outputs a power command.

2.2.1 Version 1

The torque command to the generator, T_{e2}^*, is negative for generator action. The PI controller equations are:

$$e_v = 1 - \left(\frac{v_{dc}}{v_{dc0}}\right)^2 \tag{2.6}$$

$$\frac{d}{dt}z_v = K_{iv}e_v \tag{2.7}$$

$$T_{e2}^* = -K_{pv}e_v - z_v - K_{ffv}\left(\frac{T_{e3}^*\hat{\omega}_{r3}}{\hat{\omega}_{r2}}\right) \tag{2.8}$$

where $K_{pv} > 0$ and $K_{iv} > 0$ are PI gains,[2] and $K_{ffv} > 0$ is a feed-forward gain (its value is somewhat arbitrary, but it should be slightly greater than 1.0 to account for power loss). Note that the motor commanded torque T^*_{e3} is assumed to remain constant. Also note that the two machines are assumed identical, hence the number of pole pairs does not appear explicitly in (2.8). The small-signal model of this subsystem is obtained by linearizing the above equations, i.e.,

$$\delta e_v = -\frac{2}{v_{dc0}}\delta v_{dc} \tag{2.9}$$

$$\frac{d}{dt}\delta z_v = K_{iv}\delta e_v \tag{2.10}$$

$$\delta T^*_{e2} = -K_{pv}\delta e_v - \delta z_v - K_{ffv}T^*_{e3}\left(\frac{\omega_{r20}\delta\hat{\omega}_{r3} - \omega_{r30}\delta\hat{\omega}_{r2}}{\omega^2_{r20}}\right) \tag{2.11}$$

The state-space representation of this block is obtained by using equation (2.9) in equations (2.10) and (2.11):

$$\frac{d}{dt}\delta z_v = B_{vc}\begin{bmatrix}\delta v_{dc}\\ \delta\hat{\omega}_{r2}\\ \delta\hat{\omega}_{r3}\end{bmatrix} \tag{2.12}$$

$$\delta T^*_{e2} = C_{vc}\delta z_v + D_{vc}\begin{bmatrix}\delta v_{dc}\\ \delta\hat{\omega}_{r2}\\ \delta\hat{\omega}_{r3}\end{bmatrix} \tag{2.13}$$

where

$$B_{vc} = \begin{bmatrix}-\frac{2K_{iv}}{v_{dc0}} & 0 & 0\end{bmatrix},\quad C_{vc} = -1,\quad D_{vc} = \begin{bmatrix}\frac{2K_{pv}}{v_{dc0}} & \frac{K_{ffv}T^*_{e3}\omega_{r30}}{\omega^2_{r20}} & \frac{-K_{ffv}T^*_{e3}}{\omega_{r20}}\end{bmatrix}. \tag{2.14}$$

2.2.2 Version 2

The voltage controller described in this section outputs a power command. First, a method to select the PI gains is described, and then a state-space model of the

[2]The numerical values of these gains are provided by John Deere. They have been determined experimentally.

controller is developed. To this end, we analyze the voltage controller with the dc-link model (plant model) assuming the inner torque loop is very fast.

The block diagram of the voltage controller with the plant model is shown in Fig. 2.3. An active feedback G_a is introduced in the controller. The value of G_a is generally chosen to be 5-10 times G. The closed-loop transfer function of this system is given by

$$\frac{v_{dc}^2}{v_{dc}^{*2}} = \frac{K_{pv}s + K_{iv}}{\frac{C}{2}s^2 + [K_{pv} + (G + G_a)]s + K_{iv}}\,. \tag{2.15}$$

The PI gains are selected as follows

$$K_{pv} = \omega_{bv}\frac{C}{2} \tag{2.16}$$

$$K_{iv} = \omega_{bv}(G + G_a)\,. \tag{2.17}$$

These gains reduce the transfer function (2.15) to a first order response as

$$\frac{v_{dc}^2}{v_{dc}^{*2}} = \frac{\omega_{bv}}{s + \omega_{bv}} \tag{2.18}$$

where ω_{bv} represents the bandwidth of the voltage regulator.

Now, we develop a state-space linearized model of this controller. The PI controller equations are

$$e_v = v_{dc0}^2 - v_{dc}^2 \tag{2.19}$$

$$\frac{d}{dt}z_v = K_{iv}e_v \tag{2.20}$$

$$P_2^* = -z_v - K_{pv}e_v - K_{ffv}T_{e3}^*\hat{\omega}_{rm3} + G_a v_{dc}^2 \tag{2.21}$$

where $\hat{\omega}_{rm3} = \hat{\omega}_{r3}/pp_3$,[3] denotes the estimated mechanical rotor speed of machine 3. The above equations are linearized to obtain the small-signal model of this subsystem:

$$\delta e_v = -2v_{dc0}\delta v_{dc} \tag{2.22}$$

$$\frac{d}{dt}\delta z_v = K_{iv}\delta e_v \tag{2.23}$$

$$\delta P_2^* = -\delta z_v - K_{pv}\delta e_v - K_{ffv}T_{e3}^*\delta\hat{\omega}_{rm3} + 2G_a v_{dc0}\delta v_{dc}\,. \tag{2.24}$$

[3] pp_3 is the number of pole pairs in machine 3.

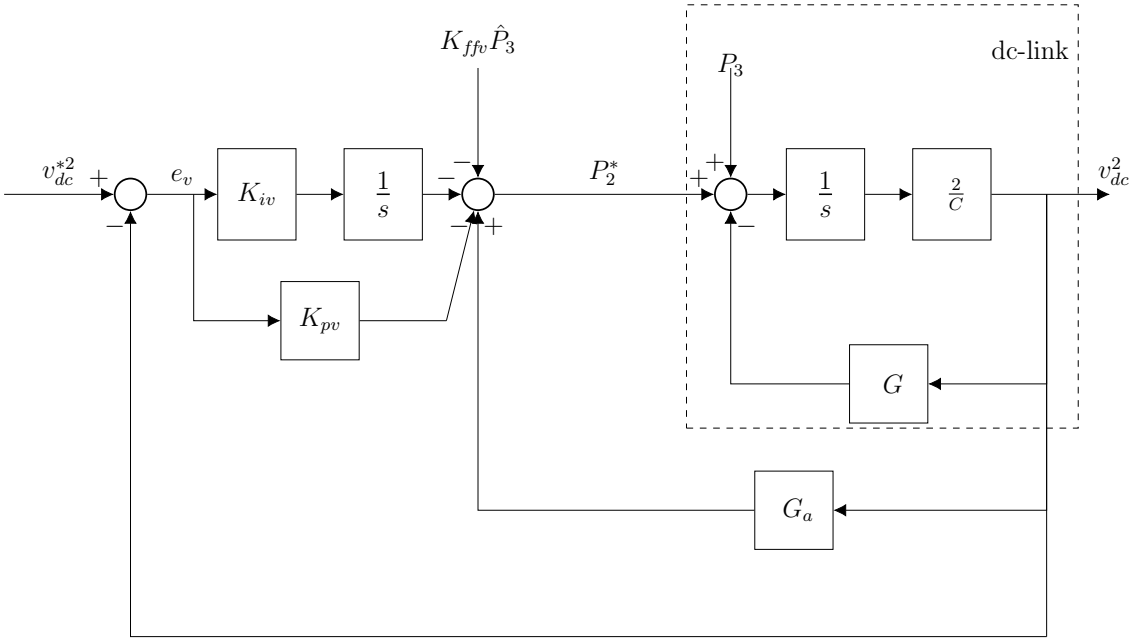

Fig. 2.3. Block diagram of voltage controller and dc-link dynamics.

The torque command is obtained from the power command by

$$T_{e2}^* = \frac{P_2^*}{\hat{\omega}_{rm2}} = pp_2 \frac{P_2^*}{\hat{\omega}_{r2}} \,. \tag{2.25}$$

where pp_2 is the number of pole pairs in machine 2. The variation in commanded torque is obtained by linearizing the above equation,

$$\delta T_{e2}^* = pp_2 \frac{\omega_{r20}\delta P_2^* - P_{20}^*\delta\hat{\omega}_{r2}}{\omega_{r20}^2} \,. \tag{2.26}$$

The state-space model of this system is obtained from (2.23) and (2.26) using (2.22) and (2.24)

$$\frac{d}{dt} z_v = B_{vc} \begin{bmatrix} \delta v_{dc} \\ \delta\hat{\omega}_{r2} \\ \delta\hat{\omega}_{r3} \end{bmatrix} \tag{2.27}$$

$$\delta T_{e2}^* = C_{vc}\delta z_v + D_{vc} \begin{bmatrix} \delta v_{dc} \\ \delta\hat{\omega}_{r2} \\ \delta\hat{\omega}_{r3} \end{bmatrix} \tag{2.28}$$

where

$$B_{vc} = \begin{bmatrix} -2K_{iv}v_{dc0} & 0 & 0 \end{bmatrix}, \quad C_{vc} = -\frac{pp_2}{\omega_{r20}},$$
$$D_{vc} = \begin{bmatrix} pp_2\frac{2v_{dc0}(K_{pv}+G_a)}{\omega_{r20}} & -pp_2\frac{P^*_{20}}{\omega^2_{r20}} & -\frac{K_{ffv}T^*_{e3}}{\omega_{r20}} \end{bmatrix}. \quad (2.29)$$

2.2.3 Comparison of Voltage Controllers

Here, we compare the response of the two voltage control strategies that have been presented. To this end, we illustrate the dc-link voltage response to a step change in voltage command, which is stepped from 700 V to 900 V. The response at various operating speeds for Version 1 is shown in Fig. 2.4(a). The response depends on the operating speed (of machine 2) because this version outputs a torque command, whereas the dc-link voltage depends on power drawn by the motors. The response for Version 2 is independent of operating speed per (2.18), as can be seen in Fig. 2.4(b). These plots were generated by simulating a simplified system consisting of the voltage control and dc link only. The detailed motor drive models were not included. It should be noted that the actual system response may differ from what these plots are showing, once the inner control loops and machine dynamics are considered.

2.3 Commanded Currents from Commanded Torque

The voltage control block outputs a variation in commanded torque, which affects the qd commanded currents. Specifically, a maximum torque per ampere (MTPA) control strategy is implemented (as a look-up table) in hardware. The MTPA functions g_q and g_d that yield the qd current commands are defined as

$$i^*_q = g_q(T^*_e, \omega^*_r) \quad (2.30)$$
$$i^*_d = g_d(T^*_e, \omega^*_r)\,. \quad (2.31)$$

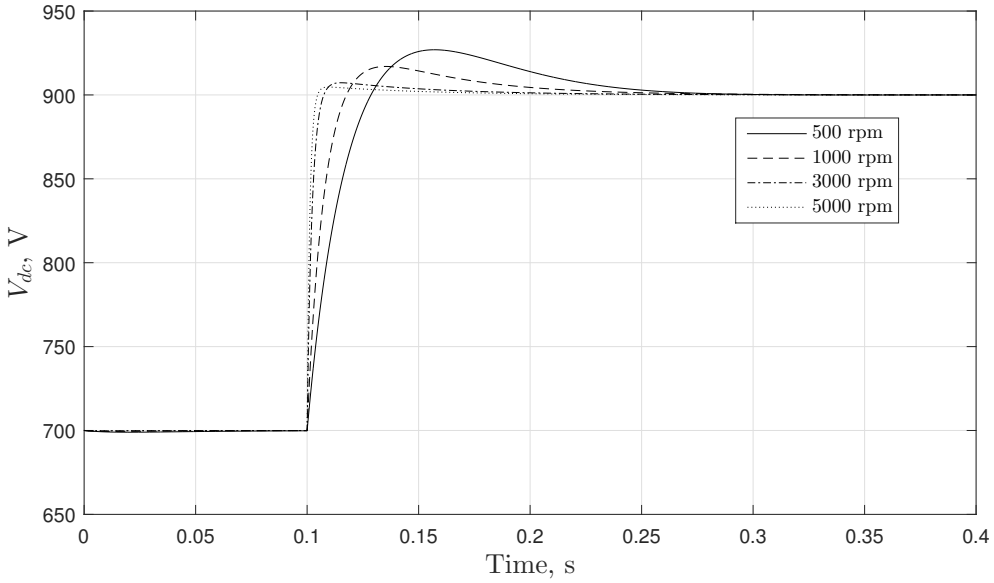

(a)

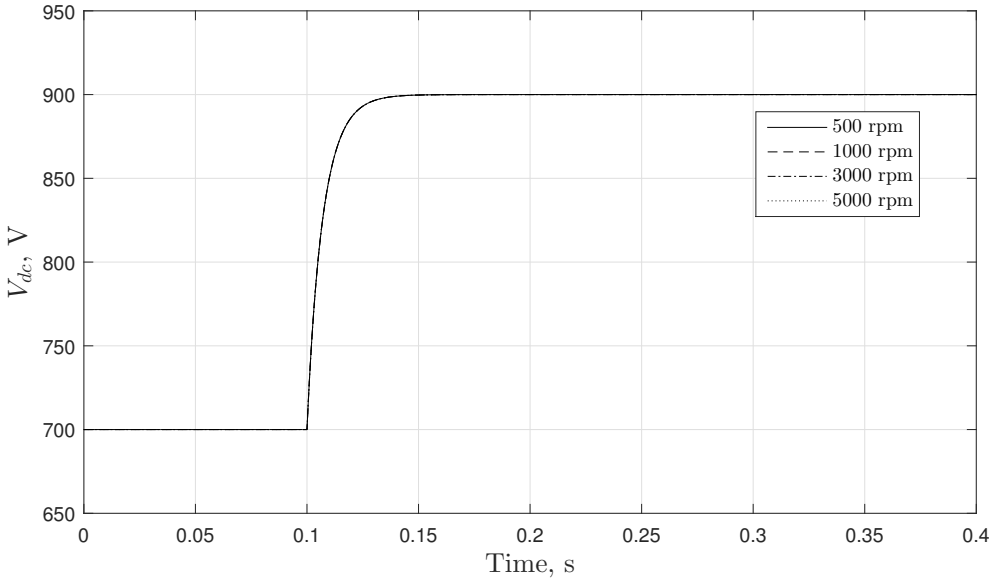

(b)

Fig. 2.4. Step response of voltage controller (a) Version 1 (b) Version 2.

Smooth (differentiable) functions are obtained by curve fitting the look-up table data (obtained from motor characterization as discussed in Appendix A.2) with a fourth degree polynomial for a given rotor speed command. For example,

$$g_q(T_e^*, \omega_r^*) = a_4(T_e^*)^4 + a_3(T_e^*)^3 + a_2(T_e^*)^2 + a_1 T_e^* + a_0 \tag{2.32}$$

Note that, for MTPA control, $a_0 = 0$ for both g_q and g_d. Hence, the variation in commanded currents using equations (2.30) and (2.31) is given by:

$$\begin{bmatrix} \delta i_q^* \\ \delta i_d^* \end{bmatrix} = \underbrace{\begin{bmatrix} \partial g_q / \partial T_e^* \\ \partial g_d / \partial T_e^* \end{bmatrix}}_{M} \delta T_e^* \,. \tag{2.33}$$

For machine 3, the partial derivative is calculated at the given value of load torque, whereas for machine 2 the equilibrium value of torque is calculated from an initialization script (see Appendix A). The variation in commanded currents becomes an input to the current control block.

2.4 Impact of Position Error on abc/qd Transformation of Stator Currents

This transformation takes place inside the controllers of both generator and motor machines, as it is an integral part of the current control strategy. The actual qd currents are found by taking the actual rotor angle θ_r in Park's transformation [18]:

$$\begin{bmatrix} i_q \\ i_d \end{bmatrix} = \frac{2}{3} \begin{bmatrix} \cos\theta_r & \cos(\theta_r - 2\pi/3) & \cos(\theta_r - 4\pi/3) \\ \sin\theta_r & \sin(\theta_r - 2\pi/3) & \sin(\theta_r - 4\pi/3) \end{bmatrix} \begin{bmatrix} i_a \\ i_b \\ i_c \end{bmatrix} \,. \tag{2.34}$$

On the other hand, the estimated qd currents are calculated using the resolver angle $\hat{\theta}_r$, which yields

$$\begin{bmatrix} \hat{i}_q \\ \hat{i}_d \end{bmatrix} = \frac{2}{3} \begin{bmatrix} \cos\hat{\theta}_r & \cos(\hat{\theta}_r - 2\pi/3) & \cos(\hat{\theta}_r - 4\pi/3) \\ \sin\hat{\theta}_r & \sin(\hat{\theta}_r - 2\pi/3) & \sin(\hat{\theta}_r - 4\pi/3) \end{bmatrix} \begin{bmatrix} i_a \\ i_b \\ i_c \end{bmatrix} \,. \tag{2.35}$$

Subtracting equation (2.34) from (2.35), and under the assumption of a small resolver angle error e_θ, so that

$$\sin(e_\theta/2) \approx e_\theta/2 \tag{2.36}$$

$$(\hat{\theta}_r + \theta_r)/2 \approx \theta_r \tag{2.37}$$

leads, after trigonometric manipulations (see Appendix C), to

$$\hat{i}_q - i_q = -i_d\, e_\theta \tag{2.38}$$

$$\hat{i}_d - i_d = i_q\, e_\theta\,. \tag{2.39}$$

Introducing variations around the corresponding equilibrium points yields

$$(\hat{i}_{q0} + \delta\hat{i}_q) - (i^*_{q0} + \delta i_q) = -(i^*_{d0} + \delta i_d)e_\theta \tag{2.40}$$

$$(\hat{i}_{d0} + \delta\hat{i}_d) - (i^*_{d0} + \delta i_d) = (i^*_{q0} + \delta i_q)e_\theta \tag{2.41}$$

Hence[4], the estimated currents are related to the actual currents and the rotor angle error by

$$\begin{bmatrix} \delta\hat{i}_q \\ \delta\hat{i}_d \end{bmatrix} = F \begin{bmatrix} \delta i_q \\ \delta i_d \\ e_\theta \end{bmatrix} \tag{2.42}$$

where higher-order terms have been neglected, and with

$$F = \begin{bmatrix} 1 & 0 & -i^*_{d0} \\ 0 & 1 & i^*_{q0} \end{bmatrix}\,. \tag{2.43}$$

2.5 Complex Vector Current Regulator (CVCR)

This block regulates the qd machine currents via PI control. Here, z_q and z_d denote the outputs of the q- and d-axis integrators, respectively. The current regulation errors are

$$e_{iq} = i^*_q - \hat{i}_q \tag{2.44}$$

$$e_{id} = i^*_d - \hat{i}_d\,. \tag{2.45}$$

[4]The equilibrium values of estimated, commanded and actual currents are equal, i.e, $\hat{i}_{q0} = i^*_{q0} = i_{q0}$ and $\hat{i}_{d0} = i^*_{d0} = i_{d0}$.

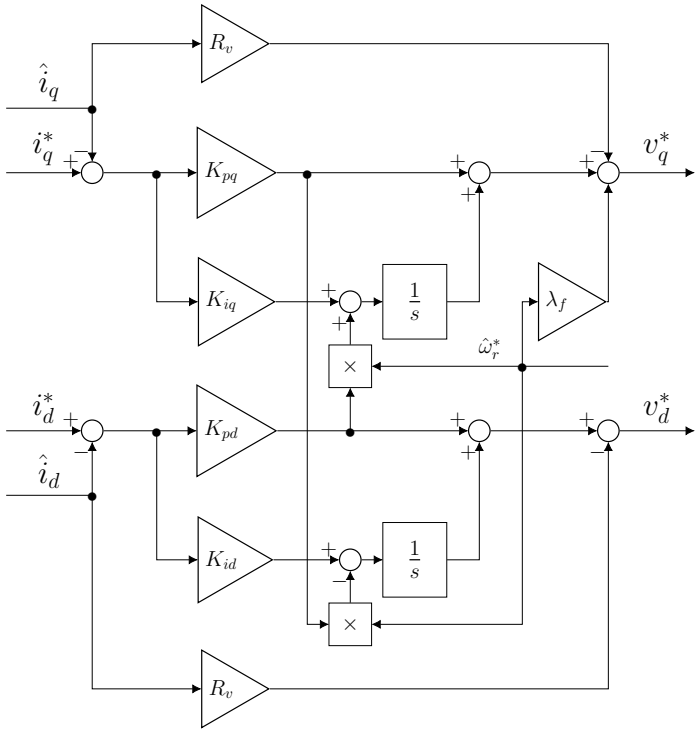

Fig. 2.5. Block diagram of complex vector current regulator.

Note that these equations are using the estimated current values, i.e., not the actual currents. Linearizing the errors about the equilibrium point yields

$$\delta e_{iq} = \delta i_q^* - \delta \hat{i}_q \tag{2.46}$$

$$\delta e_{id} = \delta i_d^* - \delta \hat{i}_d \,. \tag{2.47}$$

The CVCR control is described by the following set of equations for the integral regulator dynamics and the voltage commands as shown in Fig. 2.5, [19]:

$$\frac{d}{dt} z_q = K_{iq} e_{iq} + K_{pd} \hat{\omega}_r e_{id} \tag{2.48}$$

$$\frac{d}{dt} z_d = -K_{pq} \hat{\omega}_r e_{iq} + K_{id} e_{id} \tag{2.49}$$

$$v_q^* = K_{pq} e_{iq} + z_q - R_v \hat{i}_q + \lambda_f \hat{\omega}_r \tag{2.50}$$

$$v_d^* = K_{pd} e_{id} + z_d - R_v \hat{i}_d \tag{2.51}$$

where $\hat{\omega}_r$ is the estimated electrical rotor speed (in rad/s), λ_f is a constant that approximates the flux linkage created in the d-axis by the permanent magnets, and

R_v is a 'virtual resistance'(generally chosen to be 5 times the stator resistance). Note that the PI gains are operating point-dependent.

The linearized CVCR equations thus become[5]

$$\frac{d}{dt}\delta z_q = K_{iq}\delta e_{iq} + K_{pd}\omega_{r0}\delta e_{id} + K_{pd}e_{d0}\delta\hat{\omega}_r \tag{2.52}$$

$$\frac{d}{dt}\delta z_d = -K_{pq}\omega_{r0}\delta e_{iq} - K_{pq}e_{q0}\delta\hat{\omega}_r + K_{id}\delta e_{id} \tag{2.53}$$

$$\delta v_q^* = K_{pq}\delta e_{iq} + \delta z_q - R_v\delta\hat{i}_q + \lambda_f\delta\hat{\omega}_r \tag{2.54}$$

$$\delta v_d^* = K_{pd}\delta e_{id} + \delta z_d - R_v\delta\hat{i}_d \tag{2.55}$$

Note that the error signals

$$e_{iq} = e_{iq0} + \delta e_{iq}, \quad e_{id} = e_{id0} + \delta e_{id} \tag{2.56}$$

satisfy the steady-state equation $e_{iq0} = e_{id0} = 0$ (due to integral regulator action). This leads to

$$\frac{d}{dt}\delta z_q = K_{iq}\delta e_{iq} + K_{pd}\omega_{r0}\delta e_{id} \tag{2.57}$$

$$\frac{d}{dt}\delta z_d = -K_{pq}\omega_{r0}\delta e_{iq} + K_{id}\delta e_{id}\,. \tag{2.58}$$

Manipulating equations (2.54), (2.55), (2.57), and (2.58) using (2.46)-(2.47) results in

$$\frac{d}{dt}\begin{bmatrix}\delta z_q\\ \delta z_d\end{bmatrix} = \begin{bmatrix}B_{cr} & -B_{cr} & 0\end{bmatrix}\begin{bmatrix}\delta i_q^*\\ \delta i_d^*\\ \delta\hat{i}_q\\ \delta\hat{i}_d\\ \delta\hat{\omega}_r\end{bmatrix} \tag{2.59}$$

$$\begin{bmatrix}\delta v_q^*\\ \delta v_d^*\end{bmatrix} = C_{cr}\begin{bmatrix}\delta z_q\\ \delta z_d\end{bmatrix} + \begin{bmatrix}D_{cr} & (E_{cr}-D_{cr}) & F_{cr}\end{bmatrix}\begin{bmatrix}\delta i_q^*\\ \delta i_d^*\\ \delta\hat{i}_q\\ \delta\hat{i}_d\\ \delta\hat{\omega}_r\end{bmatrix} \tag{2.60}$$

[5]Recall $\hat{\omega}_{r0} = \omega_{r0}$.

where

$$B_{cr} = \begin{bmatrix} K_{iq} & K_{pd}\omega_{r0} \\ -K_{pq}\omega_{r0} & K_{id} \end{bmatrix}, \quad C_{cr} = \begin{bmatrix} 1 & 0 \\ 0 & 1 \end{bmatrix}, \quad D_{cr} = \begin{bmatrix} K_{pq} & 0 \\ 0 & K_{pd} \end{bmatrix},$$

$$E_{cr} = \begin{bmatrix} -R_v & 0 \\ 0 & -R_v \end{bmatrix}, \quad F_{cr} = \begin{bmatrix} \lambda_f \\ 0 \end{bmatrix}. \quad (2.61)$$

In summary, the CVCR subsystem has four inputs, $\delta i_q^*, \delta i_d^*, \delta\hat{i}_q$ and $\delta\hat{i}_d$, and one disturbance $\delta\hat{\omega}_r$.

2.6 Impact of Position Error on qd/abc Transformation of Commanded Voltages

The inverse transformation is used to determine the actual voltages supplied to the machine by the inverter. This block exists in both generator and motor. Assuming an ideal inverter without switching effects, the voltages supplied to the machine, v_{abc}, are calculated based on the estimated rotor position $\hat{\theta}_r$ by

$$v_a = v_q^* \cos\hat{\theta}_r + v_d^* \sin\hat{\theta}_r \quad (2.62)$$

$$v_b = v_q^* \cos(\hat{\theta}_r - 2\pi/3) + v_d^* \sin(\hat{\theta}_r - 2\pi/3) \quad (2.63)$$

$$v_c = v_q^* \cos(\hat{\theta}_r + 2\pi/3) + v_d^* \sin(\hat{\theta}_r + 2\pi/3)\,. \quad (2.64)$$

However, the actual machine qd voltages are based on the real value of θ_r, i.e.,

$$\begin{bmatrix} v_q \\ v_d \end{bmatrix} = \frac{2}{3} \begin{bmatrix} \cos\theta_r & \cos(\theta_r - 2\pi/3) & \cos(\theta_r - 4\pi/3) \\ \sin\theta_r & \sin(\theta_r - 2\pi/3) & \sin(\theta_r - 4\pi/3) \end{bmatrix} \begin{bmatrix} v_a \\ v_b \\ v_c \end{bmatrix}. \quad (2.65)$$

Substituting (2.62)–(2.64) in (2.65) and using trigonometric identities (see Appendix B) results in

$$v_q = v_q^* + v_d^*\, e_\theta \quad (2.66)$$

$$v_d = v_d^* - v_q^*\, e_\theta \quad (2.67)$$

which were obtained with the approximations $\cos e_\theta \approx 1$ and $\sin e_\theta \approx e_\theta$.

Linearizing about the equilibrium point,

$$v_{q0} + \delta v_q = v^*_{q0} + \delta v^*_q + (v^*_{d0} + \delta v^*_d)e_\theta \tag{2.68}$$

$$v_{d0} + \delta v_d = v^*_{d0} + \delta v^*_d - (v^*_{q0} + \delta v^*_q)e_\theta \,. \tag{2.69}$$

Neglecting the second-order terms $\delta v^*_d e_\theta$ and $\delta v^*_q e_\theta$ leads to an algebraic relationship between the actual and commanded voltages, which are not equal due to resolver position error,[6]

$$\begin{bmatrix} \delta v_q \\ \delta v_d \end{bmatrix} = G \begin{bmatrix} \delta v^*_q \\ \delta v^*_d \\ e_\theta \end{bmatrix} \tag{2.70}$$

where

$$G = \begin{bmatrix} 1 & 0 & v^*_{d0} \\ 0 & 1 & -v^*_{q0} \end{bmatrix} \,. \tag{2.71}$$

It should be noted that the resolver error is typically of the fundamental or second harmonic. Therefore, this oscillation will pass through an inverter that switches at adequately high frequency.[7]

2.7 Machine Model

The flux linkages of an electric machine (in this case, an interior permanent magnet synchronous machine) with nonlinear magnetics and spatial harmonics can be expressed in the rotor reference frame as the functions[8]

$$\lambda_q = f_q(i_q, i_d, \theta_r) \tag{2.72}$$

$$\lambda_d = f_d(i_q, i_d, \theta_r) \,. \tag{2.73}$$

[6]The equilibrium values of commanded and actual voltages are equal, i.e, $v^*_{q0} = v_{q0}$ and $v^*_{d0} = v_{d0}$.

[7]For example, at 10,000 rpm (using a high speed as an extreme case), we get 1.66 kHz for the 2nd harmonic in a 10-pole machine. If the inverter switches at 20 kHz, this voltage oscillation will impact the machine.

[8]The zero-axis flux linkage, $\lambda_0 = f_0(i_q, i_d, \theta_r)$, does not enter the system equations, since the machine is assumed to be Y-connected. Hence, $i_0 = 0$, even though $\lambda_0 \neq 0$.

Normally, when machine equations are written in the rotor reference frame, the dependence of these functions on rotor angle is eliminated. However, here it is still present in order to capture the impact of slot effects. It is important to note that the dependence on θ_r is periodic.[9] Hence, we can rewrite these equations as

$$\lambda_q(i_q, i_d, \theta_r) = \bar{f}_q(i_q, i_d) + \phi_q(i_q, i_d, \theta_r) \tag{2.74}$$

$$\lambda_d(i_q, i_d, \theta_r) = \bar{f}_d(i_q, i_d) + \phi_d(i_q, i_d, \theta_r) \tag{2.75}$$

where $\bar{f}_q$ and $\bar{f}_d$ represent average flux linkage over a period, e.g.,

$$\bar{f}_q(i_q, i_d) = \frac{1}{2\pi} \int_0^{2\pi} f_q(i_q, i_d, \theta_r)\, d\theta_r \,. \tag{2.76}$$

Therefore, ϕ_q and ϕ_d are functions of zero mean (with respect to θ_r) that represent the flux ripple. The functions $\bar{f}_q$, $\bar{f}_d$, ϕ_q, and ϕ_d can be obtained by running a series of finite element analyses (e.g., using the JMAG machine model) over the entire operating range. In particular, the periodic flux ripple terms are expressed as Fourier series as

$$\phi_q(i_q, i_d, \theta_r) = \sum_{n=1}^{\infty} a_{qn}(i_q, i_d) \cos n\theta_r + b_{qn}(i_q, i_d) \sin n\theta_r \tag{2.77}$$

$$\phi_d(i_q, i_d, \theta_r) = \sum_{n=1}^{\infty} a_{dn}(i_q, i_d) \cos n\theta_r + b_{dn}(i_q, i_d) \sin n\theta_r \,. \tag{2.78}$$

After a small change *of the currents* from an equilibrium (i_{q0}, i_{d0}), the flux linkages can be expressed as the first-order Taylor expansion[10]

$$\lambda_q(i_{q0} + \delta i_q, i_{d0} + \delta i_d, \theta_r) \approx \bar{f}_q(i_{q0}, i_{d0}) + \frac{\partial \bar{f}_q}{\partial i_q}\delta i_q + \frac{\partial \bar{f}_q}{\partial i_d}\delta i_d + \phi_q(i_{q0}, i_{d0}, \theta_r) \tag{2.79}$$

$$\lambda_d(i_{q0} + \delta i_q, i_{d0} + \delta i_d, \theta_r) \approx \bar{f}_d(i_{q0}, i_{d0}) + \frac{\partial \bar{f}_d}{\partial i_q}\delta i_q + \frac{\partial \bar{f}_d}{\partial i_d}\delta i_d + \phi_d(i_{q0}, i_{d0}, \theta_r) \tag{2.80}$$

where partial derivatives are evaluated at the equilibrium point (i_{q0}, i_{d0}). Here, we have ignored the contributions of the flux ripple terms, e.g., $(\partial\phi_q/\partial i_q)\delta i_q$, which have been assumed to be negligible.

[9]The period depends on the machine design. It is highly possible that the period is one electrical cycle, which will be the case if the stator design is identical over every electrical cycle. It will be assumed that this is the case here.

[10]It is implicitly assumed that all functions are differentiable.

For the sake of analysis, the flux ripple terms are considered as small disturbances to the system. In other words, they are not present at the equilibrium condition.[11] Therefore, we can write

$$\delta\phi_q = \phi_q(i_{q0}, i_{d0}, \theta_r) \tag{2.81}$$

$$\delta\phi_d = \phi_d(i_{q0}, i_{d0}, \theta_r)\,. \tag{2.82}$$

Hence, we have

$$\delta\lambda_q = \lambda_q(i_{q0} + \delta i_q, i_{d0} + \delta i_d, \theta_r) - \bar{f}_q(i_{q0}, i_{d0}) = L_{qq}\delta i_q + L_{qd}\delta i_d + \delta\phi_q \tag{2.83}$$

$$\delta\lambda_d = \lambda_d(i_{q0} + \delta i_q, i_{d0} + \delta i_d, \theta_r) - \bar{f}_d(i_{q0}, i_{d0}) = L_{qd}\delta i_q + L_{dd}\delta i_d + \delta\phi_d \tag{2.84}$$

The incremental inductances that appear in these equations are defined as

$$L_{qq} = \frac{\partial \bar{f}_q}{\partial i_q}, \quad L_{dd} = \frac{\partial \bar{f}_d}{\partial i_d}, \quad L_{qd} = \frac{\partial \bar{f}_q}{\partial i_d} = \frac{\partial \bar{f}_d}{\partial i_q} \tag{2.85}$$

where partial derivatives are evaluated at the equilibrium point (i_{q0}, i_{d0}). The equality of the mutual incremental inductances ($L_{qd} = L_{dq}$) is enforced so that the model is representative of a device with a conservative electromagnetic field.

Starting from the voltage equations in the rotor reference frame,

$$v_q = r_s i_q + \omega_r \lambda_d + \frac{d}{dt}\lambda_q \tag{2.86}$$

$$v_d = r_s i_d - \omega_r \lambda_q + \frac{d}{dt}\lambda_d \tag{2.87}$$

we obtain the small-signal voltage equations

$$\delta v_q = r_s \delta i_q + \delta\omega_r \lambda_{d0} + \omega_{r0}\delta\lambda_d + \frac{d}{dt}\delta\lambda_q \tag{2.88}$$

$$\delta v_d = r_s \delta i_d - \delta\omega_r \lambda_{q0} - \omega_{r0}\delta\lambda_q + \frac{d}{dt}\delta\lambda_d \tag{2.89}$$

where we have introduced for notational convenience

$$\lambda_{d0} = \bar{f}_d(i_{q0}, i_{d0}) \tag{2.90}$$

$$\lambda_{q0} = \bar{f}_q(i_{q0}, i_{d0})\,. \tag{2.91}$$

[11] This is merely a mathematical artifact in order to obtain constant electrical quantities at equilibrium, as we cannot physically eliminate the slot harmonics from the machine.

Substituting equations (2.83) and (2.84) results in

$$\delta v_q = r_s \delta i_q + \omega_{r0}(L_{dd}\delta i_d + L_{qd}\delta i_q) + \left(L_{qq}\frac{d}{dt}\delta i_q + L_{qd}\frac{d}{dt}\delta i_d\right) + \delta v_{qh} + \lambda_{d0}\delta\omega_r \quad (2.92)$$

$$\delta v_d = r_s \delta i_d - \omega_{r0}(L_{qq}\delta i_q + L_{qd}\delta i_d) + \left(L_{qd}\frac{d}{dt}\delta i_q + L_{dd}\frac{d}{dt}\delta i_d\right) + \delta v_{dh} - \lambda_{q0}\delta\omega_r \,. \quad (2.93)$$

Here, we have introduced two "back-emfs due to spatial harmonics" as the terms δv_{qh} and δv_{dh}, which are defined as

$$\delta v_{qh} = \omega_{r0}\,\delta\phi_d + \frac{d}{dt}\delta\phi_q \quad (2.94)$$

$$\delta v_{dh} = -\omega_{r0}\,\delta\phi_q + \frac{d}{dt}\delta\phi_d \,. \quad (2.95)$$

The terms $\delta\phi_q$, $\frac{d}{dt}\delta\phi_q$, $\delta\phi_d$, and $\frac{d}{dt}\delta\phi_d$ are evaluated by setting the rotor angle (in the corresponding Fourier series expressions) equal to

$$\theta_r(t) = \int_0^t \omega_r(\xi)\,d\xi + \theta_r(0) \quad (2.96)$$

where $\omega_r(t) = \omega_{r0} + \delta\omega_r(t)$. The choice of initial rotor angle $\theta_r(0)$ is arbitrary. For example, this leads to

$$\frac{d}{dt}\delta\phi_q = \omega_r\frac{\partial}{\partial\theta_r}\phi_q(i_{q0}, i_{d0}, \theta_r) = (\omega_{r0} + \delta\omega_r)\frac{\partial}{\partial\theta_r}\phi_q(i_{q0}, i_{d0}, \theta_r) \,. \quad (2.97)$$

This derivative can be analytically evaluated using (2.77),

$$\frac{d}{dt}\delta\phi_q = \omega_r \sum_{n=1}^{\infty} -n a_{qn}\sin n\theta_r + n b_{qn}\cos n\theta_r \,. \quad (2.98)$$

In summary, δv_{qh} and δv_{dh} can be pre-calculated given a steady-state operating point and a rotor speed disturbance (if any) as

$$\delta v_{qh} = \sum_{n=1}^{\infty} [\omega_{r0}a_{dn} + n(\omega_{r0} + \delta\omega_r)b_{qn}]\cos n\theta_r + [\omega_{r0}b_{dn} - n(\omega_{r0} + \delta\omega_r)a_{qn}]\sin n\theta_r \quad (2.99)$$

$$\delta v_{dh} = \sum_{n=1}^{\infty} [-\omega_{r0}a_{qn} + n(\omega_{r0} + \delta\omega_r)b_{dn}]\cos n\theta_r - [\omega_{r0}b_{qn} + n(\omega_{r0} + \delta\omega_r)a_{dn})]\sin n\theta_r \,. \quad (2.100)$$

They are input as disturbances to the small-signal system model.

The state-space model of the machine is defined with the qd currents as the state variables. By manipulating (2.92)-(2.93), we have

$$\frac{d}{dt}\begin{bmatrix}\delta i_q\\ \delta i_d\end{bmatrix} = A_m\begin{bmatrix}\delta i_q\\ \delta i_d\end{bmatrix} + B_m\begin{bmatrix}\delta v_q\\ \delta v_d\end{bmatrix} - B_m\begin{bmatrix}\delta v_{qh}\\ \delta v_{dh}\end{bmatrix} + E_m\delta\omega_r \tag{2.101}$$

The model outputs the electric power absorbed by the stator,

$$\delta P = C_m\begin{bmatrix}\delta i_q\\ \delta i_d\end{bmatrix} + D_m\begin{bmatrix}\delta v_q\\ \delta v_d\end{bmatrix} \tag{2.102}$$

It should be noted that any harmonics associated with inverter switching, dead-time compensation, etc. can be added to δv_{qd} in (2.101).

In these equations, the various matrices are given by

$$A_m = \begin{bmatrix}A_{m1} & A_{m2}\\ A_{m3} & A_{m4}\end{bmatrix} \tag{2.103}$$

$$A_{m1} = \frac{-r_s L_{dd} - \omega_{r0} L_{qd}(L_{dd} + L_{qq})}{L_{dd}L_{qq} - L_{qd}^2} \tag{2.104}$$

$$A_{m2} = \frac{r_s L_{qd} - \omega_{r0}(L_{dd}^2 + L_{qd}^2)}{L_{dd}L_{qq} - L_{qd}^2} \tag{2.105}$$

$$A_{m3} = \frac{r_s L_{qd} + \omega_{r0}(L_{qq}^2 + L_{qd}^2)}{L_{dd}L_{qq} - L_{qd}^2} \tag{2.106}$$

$$A_{m4} = \frac{-r_s L_{qq} + \omega_{r0} L_{qd}(L_{dd} + L_{qq})}{L_{dd}L_{qq} - L_{qd}^2} \tag{2.107}$$

$$B_m = \frac{1}{L_{dd}L_{qq} - L_{qd}^2}\begin{bmatrix}L_{dd} & -L_{qd}\\ -L_{qd} & L_{qq}\end{bmatrix} \tag{2.108}$$

$$E_m = \frac{1}{L_{dd}L_{qq} - L_{qd}^2}\begin{bmatrix}-(L_{dd}\lambda_{d0} + L_{qd}\lambda_{q0})\\ L_{qd}\lambda_{d0} + L_{qq}\lambda_{q0}\end{bmatrix} \tag{2.109}$$

$$C_m = \frac{3}{2}\begin{bmatrix}v_{q0}^* & v_{d0}^*\end{bmatrix}, \quad D_m = \frac{3}{2}\begin{bmatrix}i_{q0}^* & i_{d0}^*\end{bmatrix}. \tag{2.110}$$

2.8 State-Space Model of the Entire Drivetrain

2.8.1 Model 1: Formulation of System Equations with Position Error as a State

The subsystem equations that were derived in the previous section are used to assemble the state-space model for the entire drivetrain system. This is accomplished in two steps, briefly outlined as follows:

1. The state-space model for an electric machine including the CVCR control is assembled in the form: $\dot{x}_M = A_M x_M + B_M u_M + B_T \delta T_e^*$, $y_M = C_M x_M + D_M u_M + D_T \delta T_e^*$. This model is identical for both machines. The model has 5 states, $x_M = [\delta i_q, \delta i_d, \delta z_q, \delta z_d, e_\theta]$; 5 inputs, $u_M = [\delta\hat{\omega}_r, \delta\omega_r, \delta v_{qh}, \delta v_{dh}]$ and δT_e^*; and a single output, $y_M = \delta P$. Note that the torque is treated separately than the other inputs, as it will be eliminated from the equations in the next step.

2. The machine equations are combined with the dc-link and voltage control block equations. Note that for machine 3, $\delta T_{e3}^* = 0$, whereas for machine 2, δT_{e2}^* is obtained from the voltage control block.

Step 1. Combined Machine/Current Control Model in Canonical Form

In this section, we describe how to combine a single machine model with its controller model, as depicted by the dashed box in Fig. 2.2. The system equations of this combined model are obtained by cascading state-space models of each component.

From equation (2.42),[12]

$$\delta\hat{i}_{qd} = \delta i_{qd} + F_3 e_\theta \tag{2.111}$$

[12]Here, we introduce the short-hand notation $x_{qd} = [x_q \quad x_d]^T$. Also, note that the i^{th} column of any matrix A is represented by A_i.

since $\begin{bmatrix} F_1 & F_2 \end{bmatrix} = \mathbf{I}_2$ (a 2x2 identity matrix). Manipulating (2.60) using (2.33) and (2.111), the variation in commanded voltages from the output of CVCR becomes

$$\delta v_{qd}^{*} = \begin{bmatrix} (E_{cr} - D_{cr}) & \mathbf{I}_2 & (E_{cr} - D_{cr})F_3 \end{bmatrix} \begin{bmatrix} \delta i_{qd} \\ \delta z_{qd} \\ e_\theta \end{bmatrix} + \begin{bmatrix} D_{cr}M & F_{cr} \end{bmatrix} \begin{bmatrix} \delta T_e^{*} \\ \delta \hat{\omega}_r \end{bmatrix} \tag{2.112}$$

The variation of inverter output voltage is obtained by substituting the above equation in (2.70):

$$\delta v_{qd} = \begin{bmatrix} (E_{cr} - D_{cr}) & \mathbf{I}_2 & (E_{cr} - D_{cr})F_3 + G_3 \end{bmatrix} \begin{bmatrix} \delta i_{qd} \\ \delta z_{qd} \\ e_\theta \end{bmatrix} + \begin{bmatrix} D_{cr}M & F_{cr} \end{bmatrix} \begin{bmatrix} \delta T_e^{*} \\ \delta \hat{\omega}_r \end{bmatrix} . \tag{2.113}$$

Substituting (2.113) in (2.101),

$$\frac{d}{dt}\delta i_{qd} = \begin{bmatrix} A_m + B_m(E_{cr} - D_{cr}) & B_m & B_m\left[(E_{cr} - D_{cr})F_3 + G_3\right] \end{bmatrix} \begin{bmatrix} \delta i_{qd} \\ \delta z_{qd} \\ e_\theta \end{bmatrix} + \begin{bmatrix} B_m D_{cr}M & B_m F_{cr} & E_m & -B_m \end{bmatrix} \begin{bmatrix} \delta T_e^{*} \\ \delta \hat{\omega}_r \\ \delta \omega_r \\ \delta v_{qdh} \end{bmatrix} . \tag{2.114}$$

The integrator equations of the CVCR block are written in terms of state variables using (2.33), (2.59), and (2.111):

$$\frac{d}{dt}\delta z_{qd} = \begin{bmatrix} -B_{cr} & \mathbf{0}_2 & -B_{cr}F_3 \end{bmatrix} \begin{bmatrix} \delta i_{qd} \\ \delta z_{qd} \\ e_\theta \end{bmatrix} + \begin{bmatrix} B_{cr}M & \mathbf{0}_{2,4} \end{bmatrix} \begin{bmatrix} \delta T_e^{*} \\ \delta \hat{\omega}_r \\ \delta \omega_r \\ \delta v_{qdh} \end{bmatrix} \tag{2.115}$$

where $\mathbf{0}_2$ is the 2x2 zero matrix and $\mathbf{0}_{2,4}$ is the 2x4 zero matrix. Grouping (2.114) and (2.115) yields the motor equations in the desired form, $\dot{x}_M = A_M x_M + B_M u_M + B_T \delta T_e^*$:[13]

$$\underbrace{\frac{d}{dt}\begin{bmatrix}\delta i_{qd}\\ \delta z_{qd}\\ e_\theta\end{bmatrix}}_{x_M} = \underbrace{\begin{bmatrix}A_m + B_m(E_{cr} - D_{cr}) & B_m & B_m\left[(E_{cr} - D_{cr})F_3 + G_3\right]\\ -B_{cr} & \mathbf{0}_2 & -B_{cr}F_3\\ \mathbf{0}_{1,2} & \mathbf{0}_{1,2} & 0\end{bmatrix}}_{A_M}\begin{bmatrix}\delta i_{qd}\\ \delta z_{qd}\\ e_\theta\end{bmatrix} + \underbrace{\begin{bmatrix}B_m F_{cr} & E_m & -B_m\\ \mathbf{0}_{2,1} & \mathbf{0}_{2,1} & \mathbf{0}_2\\ 1 & -1 & \mathbf{0}_{1,2}\end{bmatrix}}_{B_M}\underbrace{\begin{bmatrix}\delta\hat{\omega}_r\\ \delta\omega_r\\ \delta v_{qdh}\end{bmatrix}}_{u_M} + \underbrace{\begin{bmatrix}B_m D_{cr} M\\ B_{cr} M\\ 0\end{bmatrix}}_{B_T}\delta T_e^* . \quad (2.116)$$

Substituting (2.113) in (2.102) gives the oscillations in the input power of the machine, which is the output of this model, in the form $y_M = C_M x_M + D_M u_M + D_T \delta T_e^*$:

$$y_M = \delta P = \underbrace{\begin{bmatrix}C_m + D_m(E_{cr} - D_{cr}) & D_m & D_m[(E_{cr} - D_{cr})F_3 + G_3]\end{bmatrix}}_{C_M}\underbrace{\begin{bmatrix}\delta i_{qd}\\ \delta z_{qd}\\ e_\theta\end{bmatrix}}_{x_M} + \underbrace{\begin{bmatrix}D_m F_{cr} & \mathbf{0}_{1,3}\end{bmatrix}}_{D_M}\underbrace{\begin{bmatrix}\delta\hat{\omega}_r\\ \delta\omega_r\\ \delta v_{qdh}\end{bmatrix}}_{u_M} + \underbrace{\begin{bmatrix}D_m D_{cr} M\end{bmatrix}}_{D_T}\delta T_e^* . \quad (2.117)$$

Step 2. Grouping Machine Equations with DC-Link and Voltage Control

The system equations for machines 2 and 3 can be written explicitly using (2.116) and (2.117) as

$$\frac{d}{dt}x_{M2} = A_{M2}\, x_{M2} + B_{M2}\, u_{M2} + B_{T2}\, \delta T_{e2}^* \quad (2.118)$$

$$\delta P_2 = C_{M2}\, x_{M2} + D_{M2}\, u_{M2} + D_{T2}\, \delta T_{e2}^* \quad (2.119)$$

[13]From the definition of resolver error $e_\theta = \hat{\theta}_r - \theta_r = \delta\hat{\theta}_r - \delta\theta_r$, we obtain $\frac{d}{dt}e_\theta = \delta\hat{\omega}_r - \delta\omega_r$.

and[14]

$$\frac{d}{dt}x_{M3} = A_{M3}\,x_{M3} + B_{M3}\,u_{M3} \tag{2.120}$$

$$\delta P_3 = C_{M3}\,x_{M3} + D_{M3}\,u_{M3}\,. \tag{2.121}$$

Combining equations (2.119) and (2.121) with the dc-link dynamics (2.4), we get

$$\frac{d}{dt}\delta v_{dc} = A_{dc}\delta v_{dc} + B_{dc}\begin{bmatrix} C_{M2}\,x_{M2} + D_{M2}\,u_{M2} + D_{T2}\,\delta T^*_{e2} \\ C_{M3}\,x_{M3} + D_{M3}\,u_{M3} \end{bmatrix}. \tag{2.122}$$

Grouping equations (2.118), (2.120), and (2.122) yields

$$\frac{d}{dt}\begin{bmatrix} x_{M2} \\ x_{M3} \\ \delta v_{dc} \end{bmatrix} = \begin{bmatrix} A_{M2} & \mathbf{0}_5 & \mathbf{0}_{5,1} \\ \mathbf{0}_5 & A_{M3} & \mathbf{0}_{5,1} \\ B_{dc_1}C_{M2} & B_{dc_2}C_{M3} & A_{dc} \end{bmatrix}\begin{bmatrix} x_{M2} \\ x_{M3} \\ \delta v_{dc} \end{bmatrix} + \begin{bmatrix} B_{M2} & \mathbf{0}_{5,4} \\ \mathbf{0}_{5,4} & B_{M3} \\ B_{dc_1}D_{M2} & B_{dc_2}D_{M3} \end{bmatrix}\begin{bmatrix} u_{M2} \\ u_{M3} \end{bmatrix} + \begin{bmatrix} B_{T2} \\ \mathbf{0}_{5,1} \\ B_{dc_1}D_{T2} \end{bmatrix}\delta T^*_{e2}\,. \tag{2.123}$$

Finally, we incorporate the voltage control block into the system state-space model, i.e., we use equations (2.12) and (2.13). Hence, the torque commands are no longer

[14]Recall that $\delta T^*_{e3} = 0$.

explicit inputs, and the integrator z_v is appended to the vector of state variables. Thus we obtain

$$\underbrace{\frac{d}{dt}\begin{bmatrix} x_{M2} \\ x_{M3} \\ \delta v_{dc} \\ \delta z_v \end{bmatrix}}_{x_S} = \underbrace{\begin{bmatrix} A_{M2} & \mathbf{0}_5 & B_{T2}D_{vc_1} & B_{T2}C_{vc} \\ \mathbf{0}_5 & A_{M3} & \mathbf{0}_{5,1} & \mathbf{0}_{5,1} \\ B_{dc_1}C_{M2} & B_{dc_2}C_{M3} & A_{dc}+B_{dc_1}D_{T2}D_{vc_1} & B_{dc_1}D_{T2}C_{vc} \\ \mathbf{0}_{1,5} & \mathbf{0}_{1,5} & B_{vc} & 0 \end{bmatrix}}_{A_S} \begin{bmatrix} x_{M2} \\ x_{M3} \\ \delta v_{dc} \\ \delta z_v \end{bmatrix} +$$

$$\underbrace{\begin{bmatrix} B_{M2}+\begin{bmatrix} B_{T2}D_{vc_2} & \mathbf{0}_{5,3} \end{bmatrix} & \begin{bmatrix} B_{T2}D_{vc_3} & \mathbf{0}_{5,3} \end{bmatrix} \\ \mathbf{0}_{5,4} & B_{M3} \\ B_{dc_1}D_{M2}+\begin{bmatrix} B_{dc_1}D_{T2}D_{vc_2} & \mathbf{0}_{1,3} \end{bmatrix} & B_{dc_2}D_{M3}+\begin{bmatrix} B_{dc_1}D_{T2}D_{vc_3} & \mathbf{0}_{1,3} \end{bmatrix} \\ \mathbf{0}_{1,4} & \mathbf{0}_{1,4} \end{bmatrix}}_{B_S} \underbrace{\begin{bmatrix} u_{M2} \\ u_{M3} \end{bmatrix}}_{u_S} . \tag{2.124}$$

The output of the system is the dc-link voltage oscillation, which is one of the system states:

$$\underbrace{\delta v_{dc}}_{y_S} = \underbrace{\begin{bmatrix} \mathbf{0}_{1,10} & 1 & 0 \end{bmatrix}}_{C_S} \begin{bmatrix} x_{M2} \\ x_{M3} \\ \delta v_{dc} \\ \delta z_v \end{bmatrix} + \underbrace{\begin{bmatrix} \mathbf{0}_{1,8} \end{bmatrix}}_{D_S} \begin{bmatrix} u_{M2} \\ u_{M3} \end{bmatrix} . \tag{2.125}$$

Hence, the state-space model for the entire system has been formulated as the 12-order dynamic system

$$\frac{d}{dt}x_S = A_S\, x_S + B_S\, u_S \tag{2.126}$$

$$y_S = C_S\, x_S + D_S\, u_S\,. \tag{2.127}$$

2.8.2 Model 2: Alternative Formulation of System Equations with Position Error as an Input Disturbance

Depending on the signal processing algorithm used for estimating the speed from position signal, it is not always necessary that the ideal mathematical relation $\frac{d}{dt}e_\theta =$

$\delta\hat{\omega}_r - \delta\omega_r$, used in the previous section, will hold. For instance, the estimated rotor speed may be low-pass filtered, thereby leading to very precise rotor speed estimation (at least in the steady state), whereas resolver error may still remain significant. To account for this, we decouple the input disturbances $(e_\theta, \delta\hat{\omega}_r, \delta\omega_r)$. A modified state-space model where the position error (e_θ) is treated as an input disturbance (i.e., no longer a state variable) is set forth.

Equations (2.116) and (2.117) can be rewritten as follows, where the states x_M, inputs/disturbances u_M, and system matrices A_M, B_M, C_M, and D_M have been re-defined:

$$\underbrace{\frac{d}{dt}\begin{bmatrix}\delta i_{qd}\\ \delta z_{qd}\end{bmatrix}}_{x_M} = \underbrace{\begin{bmatrix}A_m + B_m(E_{cr} - D_{cr}) & B_m\\ -B_{cr} & \mathbf{0}_2\end{bmatrix}}_{A_M}\begin{bmatrix}\delta i_{qd}\\ \delta z_{qd}\end{bmatrix} + \underbrace{\begin{bmatrix}B_m F_{cr} & E_m & B_m\left[(E_{cr} - D_{cr})F_3 + G_3\right] & -B_m\\ \mathbf{0}_{2,1} & \mathbf{0}_{2,1} & -B_{cr}F_3 & \mathbf{0}_2\end{bmatrix}}_{B_M}\underbrace{\begin{bmatrix}\delta\hat{\omega}_r\\ \delta\omega_r\\ e_\theta\\ \delta v_{qdh}\end{bmatrix}}_{u_M} + \underbrace{\begin{bmatrix}B_m D_{cr} M\\ B_{cr} M\end{bmatrix}}_{B_T}\delta T_e^* \tag{2.128}$$

$$y_M = \delta P = \underbrace{\begin{bmatrix}C_m + D_m(E_{cr} - D_{cr}) & D_m\end{bmatrix}}_{C_M}\underbrace{\begin{bmatrix}\delta i_{qd}\\ \delta z_{qd}\end{bmatrix}}_{x_M} + \underbrace{\begin{bmatrix}D_m F_{cr} & 0 & D_m[(E_{cr} - D_{cr})F_3 + G_3] & \mathbf{0}_{1,2}\end{bmatrix}}_{D_M}\underbrace{\begin{bmatrix}\delta\hat{\omega}_r\\ \delta\omega_r\\ e_\theta\\ \delta v_{qdh}\end{bmatrix}}_{u_M} + \underbrace{\begin{bmatrix}D_m D_{cr} M\end{bmatrix}}_{D_T}\delta T_e^* \,. \tag{2.129}$$

The system state-space model is obtained as explained in section 2.8.1:

$$\underbrace{\frac{d}{dt}\begin{bmatrix} x_{M2} \\ x_{M3} \\ \delta v_{dc} \\ \delta z_v \end{bmatrix}}_{x_S} = \underbrace{\begin{bmatrix} A_{M2} & \mathbf{0}_4 & B_{T2}D_{vc_1} & B_{T2}C_{vc} \\ \mathbf{0}_4 & A_{M3} & \mathbf{0}_{4,1} & \mathbf{0}_{4,1} \\ B_{dc_1}C_{M2} & B_{dc_2}C_{M3} & A_{dc} + B_{dc_1}D_{T2}D_{vc_1} & B_{dc_1}D_{T2}C_{vc} \\ \mathbf{0}_{1,4} & \mathbf{0}_{1,4} & B_{vc} & 0 \end{bmatrix}}_{A_S} \begin{bmatrix} x_{M2} \\ x_{M3} \\ \delta v_{dc} \\ \delta z_v \end{bmatrix} +$$

$$\underbrace{\begin{bmatrix} B_{M2} + \begin{bmatrix} B_{T2}D_{vc_2} & \mathbf{0}_{4,4} \end{bmatrix} & \begin{bmatrix} B_{T2}D_{vc_3} & \mathbf{0}_{4,4} \end{bmatrix} \\ \mathbf{0}_{4,5} & B_{M3} \\ B_{dc_1}D_{M2} + \begin{bmatrix} B_{dc_1}D_{T2}D_{vc_2} & \mathbf{0}_{1,4} \end{bmatrix} & B_{dc_2}D_{M3} + \begin{bmatrix} B_{dc_1}D_{T2}D_{vc_3} & \mathbf{0}_{1,4} \end{bmatrix} \\ \mathbf{0}_{1,5} & \mathbf{0}_{1,5} \end{bmatrix}}_{B_S} \underbrace{\begin{bmatrix} u_{M2} \\ u_{M3} \end{bmatrix}}_{u_S} \tag{2.130}$$

$$\underbrace{\delta v_{dc}}_{y_S} = \underbrace{\begin{bmatrix} \mathbf{0}_{1,8} & 1 & 0 \end{bmatrix}}_{C_S} \begin{bmatrix} x_{M2} \\ x_{M3} \\ \delta v_{dc} \\ \delta z_v \end{bmatrix} + \underbrace{\begin{bmatrix} \mathbf{0}_{1,10} \end{bmatrix}}_{D_S} \begin{bmatrix} u_{M2} \\ u_{M3} \end{bmatrix} . \tag{2.131}$$

Now, this is a 10^{th}-order dynamic system with 10 inputs.

2.9 Frequency Response Analysis

The impact of each input disturbance on the dc-link can be analyzed in the frequency domain based on the state-space models described in previous section. From basics of linear system control theory, a transfer function matrix is obtained by taking a Laplace transform with zero initial conditions as follows [20]:

$$H(s) = C_S(sI - A_S)^{-1}B_S + D_S \, . \tag{2.132}$$

For Model 1, $H(s)$ is a 1×8 matrix obtained from (2.126) and (2.127), with each element representing a transfer function

$$H_i(s) = \frac{\delta v_{dc}}{u_{S,i}}, \quad i = 1, 2, \ldots, 8 \, . \tag{2.133}$$

For instance, the transfer functions related to disturbances originating from machine 2 are

$$H_1(s) = \frac{\delta v_{dc}(s)}{\delta \hat{\omega}_{r2}(s)}, \quad H_2(s) = \frac{\delta v_{dc}(s)}{\delta \omega_{r2}(s)}, \quad H_3(s) = \frac{\delta v_{dc}(s)}{\delta v_{qh2}(s)}, \quad H_4(s) = \frac{\delta v_{dc}(s)}{\delta v_{dh2}(s)}\,. \tag{2.134}$$

Similarly for Model 2, $H(s)$ is a 1×10 matrix defined using (2.130) and (2.131). For example, the transfer functions of interest for studying the impact of rotor position and speed disturbances from machine 2 are

$$H_1(s) = \frac{\delta v_{dc}(s)}{\delta \hat{\omega}_{r2}(s)}, \quad H_2(s) = \frac{\delta v_{dc}(s)}{\delta \omega_{r2}(s)}, \quad H_3(s) = \frac{\delta v_{dc}(s)}{e_{\theta 2}(s)}\,. \tag{2.135}$$

2.10 Selection of Control Gains in CVCR

This section discusses the selection of CVCR controller gains considering a simplified system model. The state-space equations of the CVCR are simplified assuming that the estimated and actual qd currents are the same ($i_{qd} = \hat{i}_{qd}$) and neglecting the oscillations in estimated speed. From (2.59) and (2.60), we obtain the simplified equations:

$$\frac{d}{dt}\begin{bmatrix}\delta z_q \\ \delta z_d\end{bmatrix} = \begin{bmatrix}B_{cr} & -B_{cr}\end{bmatrix}\begin{bmatrix}\delta i_q^* \\ \delta i_d^* \\ \delta i_q \\ \delta i_d\end{bmatrix} \tag{2.136}$$

$$\begin{bmatrix}\delta v_q^* \\ \delta v_d^*\end{bmatrix} = C_{cr}\begin{bmatrix}\delta z_q \\ \delta z_d\end{bmatrix} + \begin{bmatrix}D_{cr} & (E_{cr} - D_{cr})\end{bmatrix}\begin{bmatrix}\delta i_q^* \\ \delta i_d^* \\ \delta i_q \\ \delta i_d\end{bmatrix}\,. \tag{2.137}$$

Similarly, the machine model is simplified by neglecting the cross-coupling inductances, spatial harmonics and oscillations in shaft speed. Also, the actual qd voltages are assumed to be equal to commanded qd voltages. The state-space equation (2.101) thus becomes

$$\frac{d}{dt}\begin{bmatrix}\delta i_q \\ \delta i_d\end{bmatrix} = A_m\begin{bmatrix}\delta i_q \\ \delta i_d\end{bmatrix} + B_m\begin{bmatrix}\delta v_q^* \\ \delta v_d^*\end{bmatrix} \tag{2.138}$$

where A_m and B_m are

$$A_m = \begin{bmatrix} \frac{-r_s}{L_{qq}} & \frac{-\omega_{r0}L_{dd}}{L_{qq}} \\ \frac{\omega_{r0}L_{qq}}{L_{dd}} & \frac{-r_s}{L_{dd}} \end{bmatrix}, \; B_m = \begin{bmatrix} \frac{1}{L_{qq}} & 0 \\ 0 & \frac{1}{L_{dd}} \end{bmatrix}. \tag{2.139}$$

Substituting (2.137) in (2.138) yields

$$\frac{d}{dt}\delta i_{qd} = \Big[A_m + B_m(E_{cr} - D_{cr})\Big]\,\delta i_{qd} + B_m C_{cr}\delta z_{qd} + B_m D_{cr}\delta i^*_{qd}\,. \tag{2.140}$$

Combining (2.136) and (2.140), we get the simplified state-space system model

$$\frac{d}{dt}\underbrace{\begin{bmatrix}\delta i_{qd}\\ \delta z_{qd}\end{bmatrix}}_{x_S} = \underbrace{\begin{bmatrix} A_m + B_m(E_{cr} - D_{cr}) & B_m C_{cr} \\ -B_{cr} & \mathbf{0}_2 \end{bmatrix}}_{A_S}\begin{bmatrix}\delta i_{qd}\\ \delta z_{qd}\end{bmatrix} + \underbrace{\begin{bmatrix} B_m D_{cr} \\ B_{cr}\end{bmatrix}}_{B_S}\underbrace{\begin{bmatrix}\delta i^*_{qd}\end{bmatrix}}_{u_S}. \tag{2.141}$$

The machine output qd currents are given by

$$\underbrace{\delta i_{qd}}_{y_S} = \underbrace{\begin{bmatrix}\mathbf{I}_2 & \mathbf{0}_2\end{bmatrix}}_{C_S}\begin{bmatrix}\delta i_{qd}\\ \delta z_{qd}\end{bmatrix}. \tag{2.142}$$

The 2×2 transfer function matrix $H(s)$ for the above state-space model is derived using (2.132). The elements of $H(s)$ matrix are

$$\frac{\delta i_q}{\delta i^*_q} = \frac{h_{1,1}(s)}{\text{den}(s)},\; \frac{\delta i_q}{\delta i^*_d} = \frac{h_{1,2}(s)}{\text{den}(s)},\; \frac{\delta i_d}{\delta i^*_q} = \frac{h_{2,1}(s)}{\text{den}(s)},\; \frac{\delta i_d}{\delta i^*_d} = \frac{h_{2,2}(s)}{\text{den}(s)} \tag{2.143}$$

where

$$\begin{aligned} h_{1,1}(s) = {} & L_{dd}K_{pq}s^3 + [(r_s + R_v)K_{pq} + L_{dd}K_{iq} + K_{pd}K_{pq}]s^2 + \\ & [(r_s + R_v)K_{iq} + \omega_{r0}^2 L_{dd}K_{pq} + K_{pd}K_{iq} + K_{pq}K_{id}]s + \omega_{r0}^2 K_{pd}K_{pq} + K_{id}K_{iq} \end{aligned} \tag{2.144}$$

$$h_{1,2}(s) = [(r_s + R_v)K_{pd} - K_{id}L_{dd}]\omega_{r0}s \tag{2.145}$$

$$h_{2,1}(s) = [K_{iq}L_{qq} - (r_s + R_v)K_{pq}]\omega_{r0}s \tag{2.146}$$

$$\begin{aligned} h_{2,2}(s) = {} & L_{qq}K_{pd}s^3 + [(r_s + R_v)K_{pd} + L_{qq}K_{id} + K_{pd}K_{pq}]s^2 + \\ & [(r_s + R_v)K_{id} + \omega_{r0}^2 L_{qq}K_{pd} + K_{pd}K_{iq} + K_{pq}K_{id}]s + \omega_{r0}^2 K_{pd}K_{pq} + K_{id}K_{iq} \end{aligned} \tag{2.147}$$

$$\begin{aligned}\text{den}(s) = {} & L_{dd}L_{qq}s^4 + [(r_s + R_v)(L_{dd} + L_{qq}) + L_{dd}K_{pq} + L_{qq}K_{pd}]s^3 + \\ & [(r_s + R_v)(K_{pd} + K_{pq}) + (r_s + R_v)^2 + L_{dd}L_{qq}\omega_{r0}^2 + L_{dd}K_{iq} + L_{qq}K_{id} + K_{pd}K_{pq}]s^2 + \\ & [(r_s+R_v)(K_{id}+K_{iq})+\omega_{r0}^2(L_{dd}K_{pq}+L_{qq}K_{pd})+K_{pd}K_{iq}+K_{pq}K_{id}]s+\omega_{r0}^2K_{pd}K_{pq}+K_{id}K_{iq}\end{aligned} \tag{2.148}$$

The PI gains are selected as follows [21]:

$$K_{pd} = \omega_{bi}L_{dd}, K_{id} = \omega_{bi}(r_s + R_v), K_{pq} = \omega_{bi}L_{qq}, K_{iq} = \omega_{bi}(r_s + R_v)\,. \tag{2.149}$$

This choice decouples the qd axes, i.e., $h_{1,2}(s) = h_{2,1}(s) = 0$, and also reduces the polynomials in (2.144)–(2.148) to

$$h_{1,1}(s) = h_{2,2}(s) = \left[\left(s + \frac{r_s + R_v}{L_{dd}}\right)\left(s + \frac{r_s + R_v}{L_{qq}}\right) + \omega_{r0}^2\right](s + \omega_{bi})\omega_{bi}L_{qq}L_{dd} \tag{2.150}$$

$$\text{den}(s) = \left[\left(s + \frac{r_s + R_v}{L_{dd}}\right)\left(s + \frac{r_s + R_v}{L_{qq}}\right) + \omega_{r0}^2\right](s + \omega_{bi})^2L_{qq}L_{dd}\,. \tag{2.151}$$

The transfer functions are thus reduced to first-order responses,

$$\frac{\delta i_q}{\delta i_q^*} = \frac{\delta i_d}{\delta i_d^*} = \frac{\omega_{bi}}{s + \omega_{bi}} \tag{2.152}$$

where ω_{bi} is the bandwidth of the current regulator.

3. IMPACT OF DISTURBANCES: NUMERICAL RESULTS

In this section, we illustrate the impact of the various disturbances (i.e., the components of u_S in (2.124) and (2.130)) on the dc-link voltage using the state-space model that was derived in the previous section. The results are obtained in the frequency domain, as explained in Section 2.9.

3.1 Frequency Sweeps

The first set of results is intended to show the effect of position error and shaft oscillations on dc-link voltage. To this end, six different operating points are selected; they are listed in Table 3.1. The impact of each input disturbance on the dc-link is observed via frequency response (Bode) plots. The theoretical analysis of Section 1.1 as well as experimental results indicate that the errors in estimated rotor position and speed are commonly encountered at fundamental and second harmonics; therefore, these particular frequencies are highlighted.

Analyses are conducted for both Model 1 and Model 2, and the results are shown in Figs. 3.1–3.6 and Figs. 3.7–3.12, respectively. Results for both versions of the voltage controller (see Section 2.2) are included. These results are generated by considering $R_v = 5r_s$ and $\omega_{bi} = 2\pi 80$ Hz.

In the formulation of Model 1, the estimated rotor speed is assumed to be directly tied to the estimated rotor angle (e.g., through some ideal speed estimation algorithm). In this case:

1. In the presence of shaft oscillations without position error ($e_\theta = 0$), we have $\delta\hat{\omega}_r = \delta\omega_r$. Due to linearity of the small-signal dynamic system, the dc-link oscillations can be found by superposition. For example, for oscillations occurring

Table 3.1
Operating Points

Case Study	Machine 2 Speed	Machine 3 Speed	Load Torque	Electrical Power Absorbed by Traction Drive from DC-Link
1	1000 rpm	1000 rpm	50 Nm	5.65 kW
2	3000 rpm	3000 rpm	100 Nm	34 kW
3	6000 rpm	6000 rpm	150 Nm	103.5 kW
4	9000 rpm	9000 rpm	150 Nm	163 kW
5	3500 rpm	5000 rpm	150 Nm	84.2 kW
6	5400 rpm	9000 rpm	100 Nm	109.6 kW

in the shaft speed of machine 2, the dc-link voltage oscillation can be found using (2.134):

$$\delta v_{dc}(s) = [H_1(s) + H_2(s)]\, \delta\omega_{r2}(s) \tag{3.1}$$

Results considering oscillations of unit magnitude (1 rpm) are shown in Figs. 3.1(a), 3.1(b), 3.2(a), 3.2(b), ... , 3.6(a), 3.6(b).

2. In the absence of actual shaft oscillations but in the presence of position error, we have $\delta\hat{\omega}_r = \frac{d}{dt}e_\theta$. For example, for oscillations occurring in the estimated speed of machine 2, (2.134) yields

$$\delta v_{dc}(s) = H_1(s)\, \delta\hat{\omega}_{r2}(s) = H_1(s)\, s e_{\theta 2}(s)\,. \tag{3.2}$$

The results shown in Figs. 3.1(c), 3.1(d), ... , 3.6(c), 3.6(d) correspond to a 1° position error magnitude (setting $e_\theta = \frac{\pi}{180}\angle\underline{0}$).

For Model 2, the impact of unit magnitude (1 rpm) shaft oscillations is shown in Figs. 3.7(a), 3.7(b), ... , 3.12(b), 3.12(b). The results in Figs. 3.7(c), 3.7(d), ... , 3.12(c),

3.12(d) illustrate the effect of unit magnitude (1 rpm) oscillations in estimated speed. Similarly, the influence of 1° position error is seen in Figs. 3.7(e), 3.7(f), . . . , 3.12(e), 3.12(f).

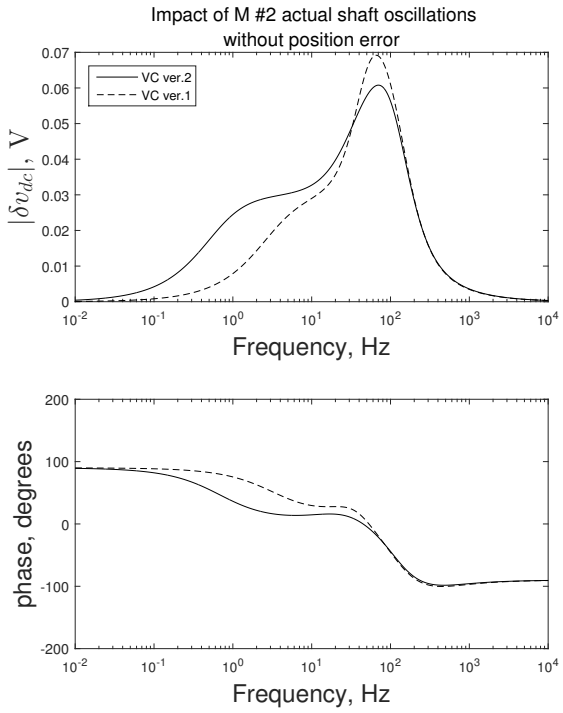

(a)

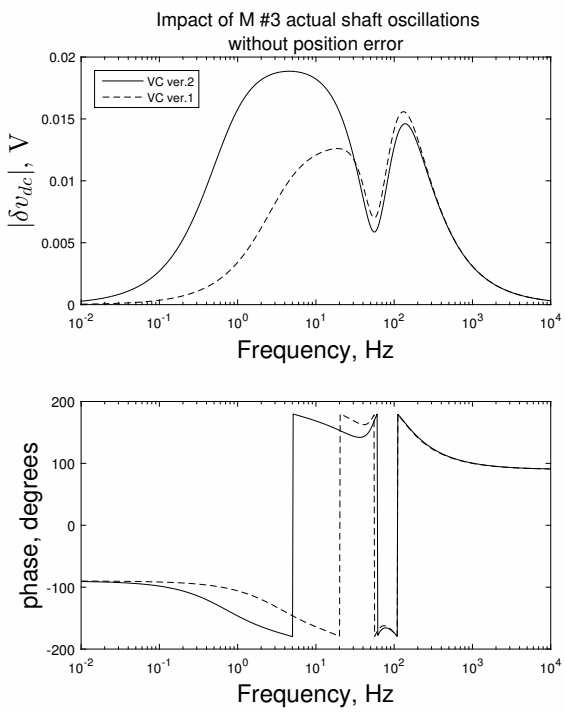

(b)

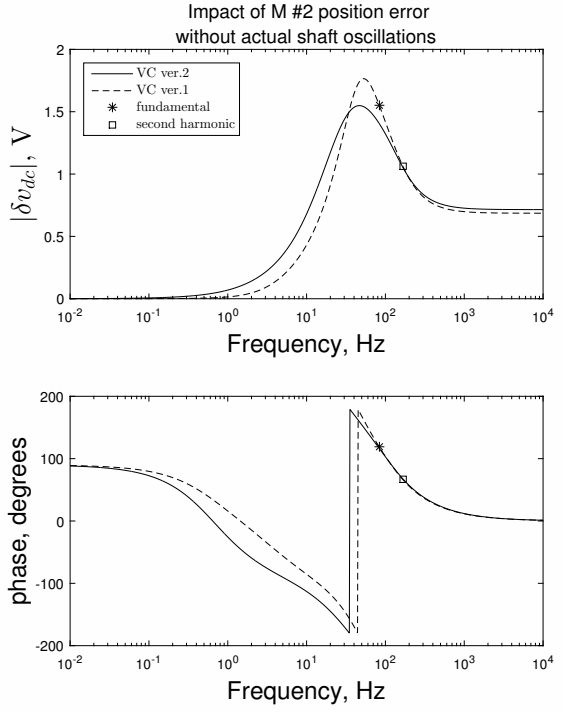

(c)

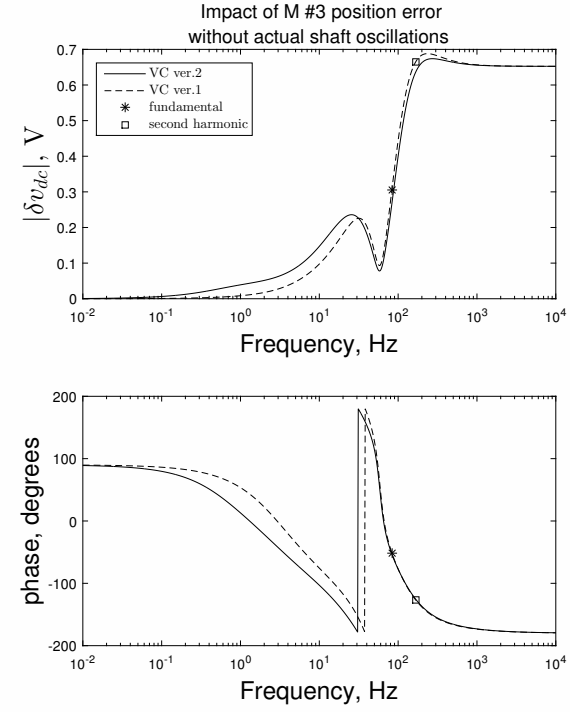

(d)

Fig. 3.1. Bode plots for case study 1 (Model 1).

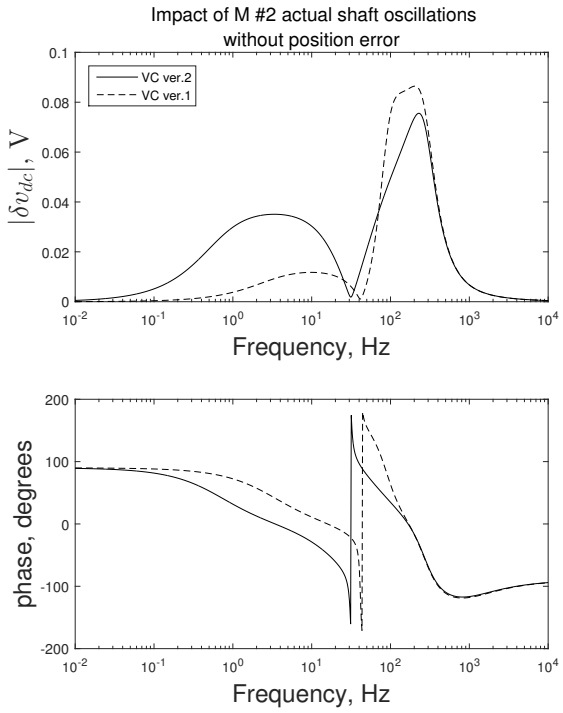

(a)

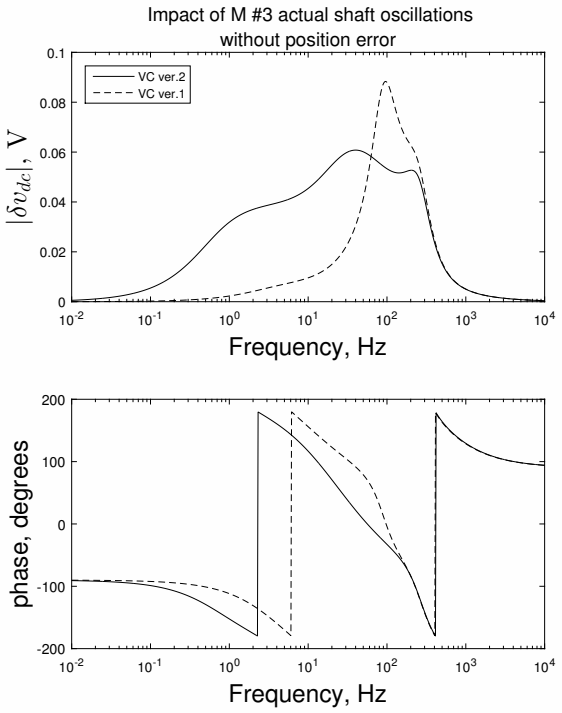

(b)

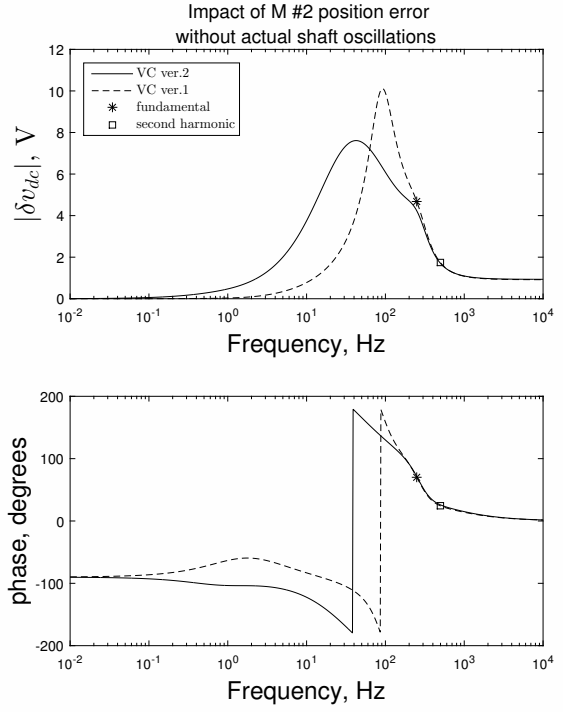

(c)

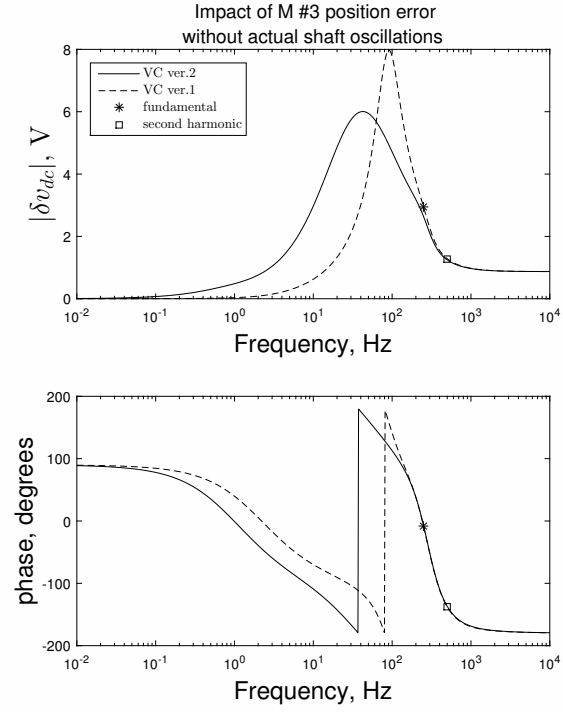

(d)

Fig. 3.2. Bode plots for case study 2 (Model 1).

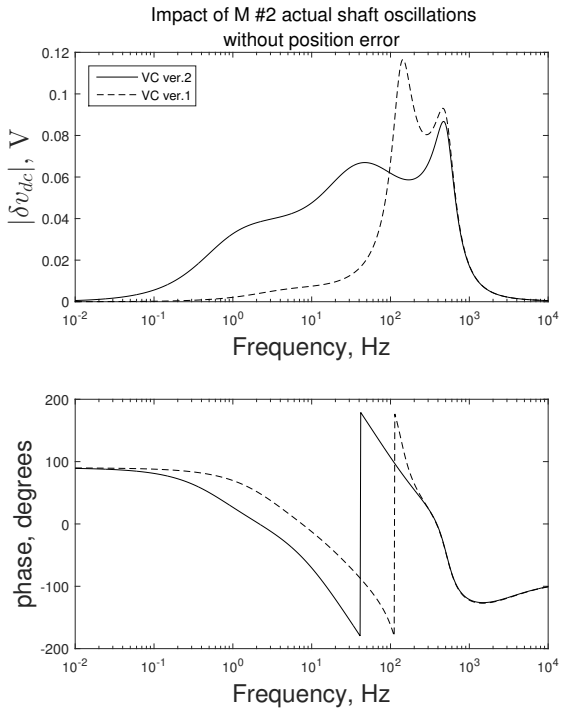

(a)

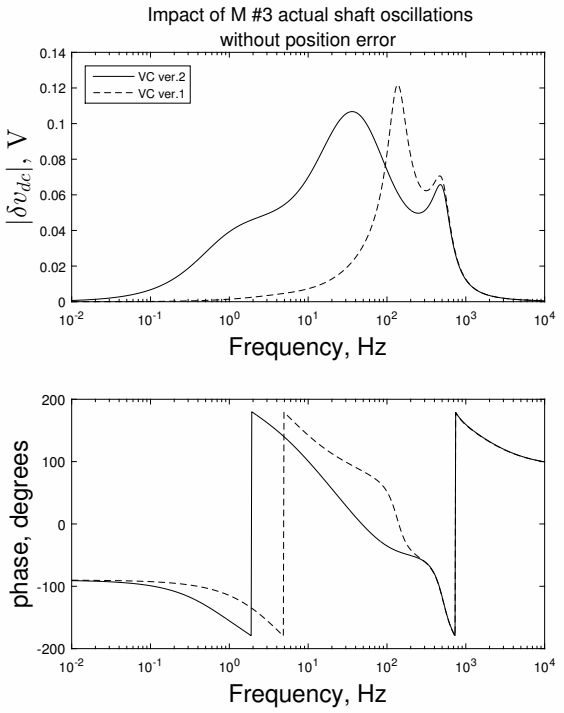

(b)

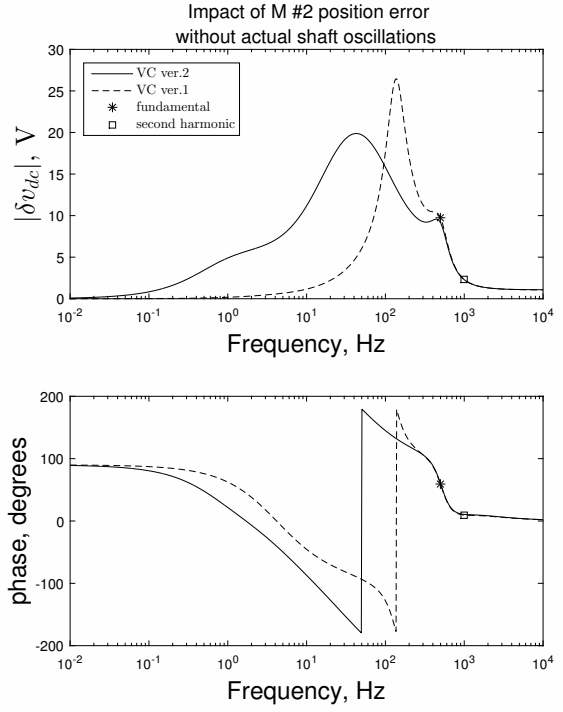

(c)

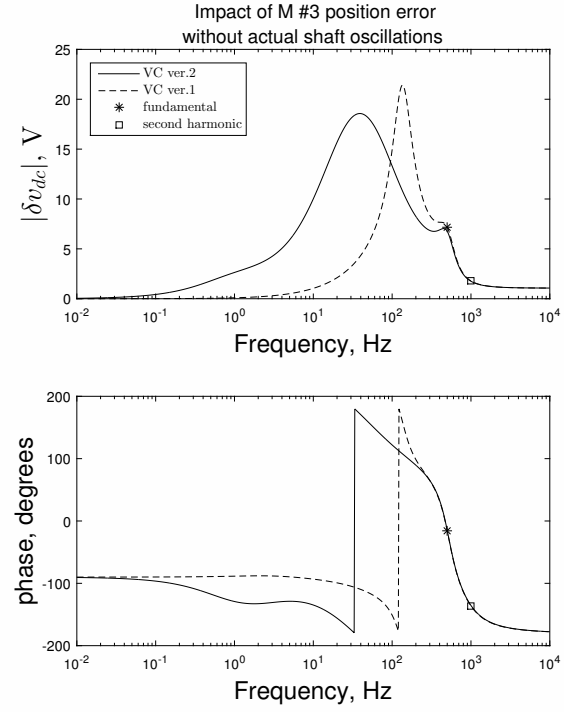

(d)

Fig. 3.3. Bode plots for case study 3 (Model 1).

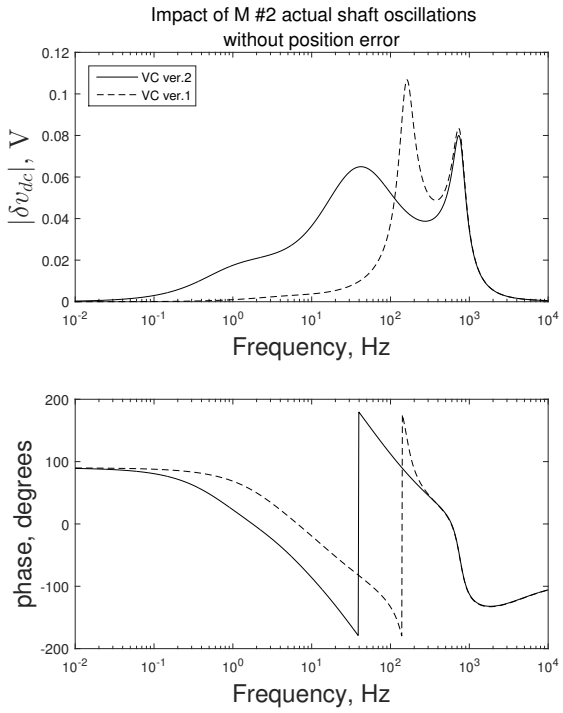

(a)

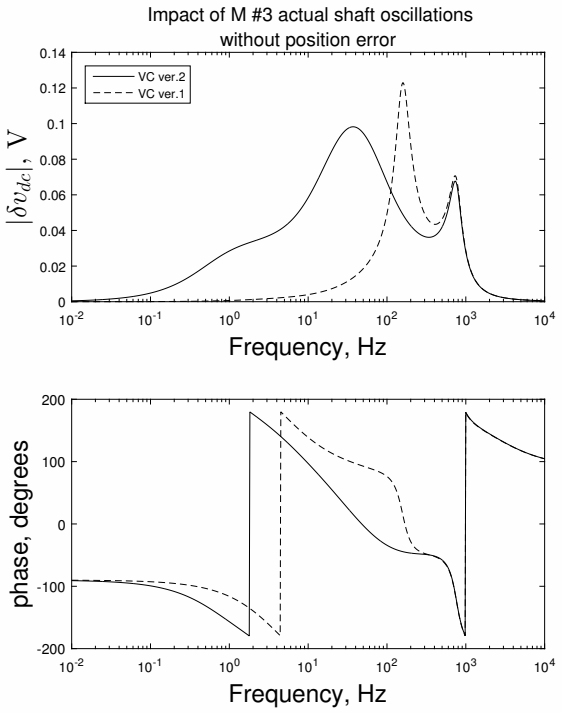

(b)

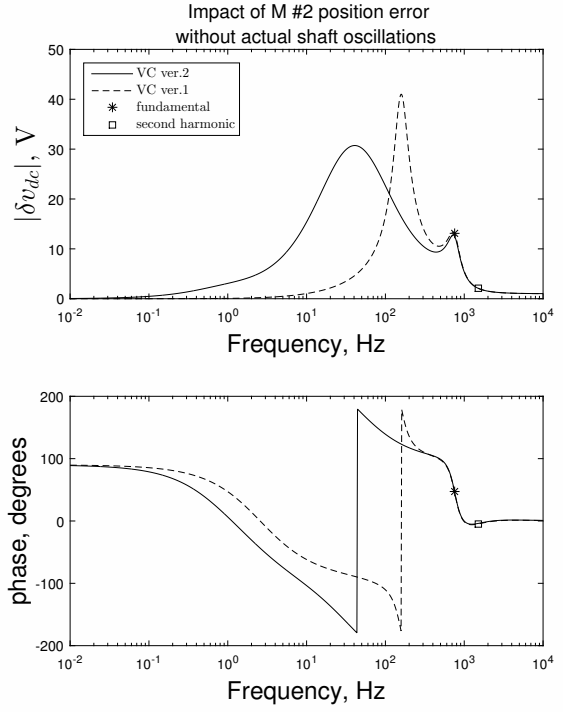

(c)

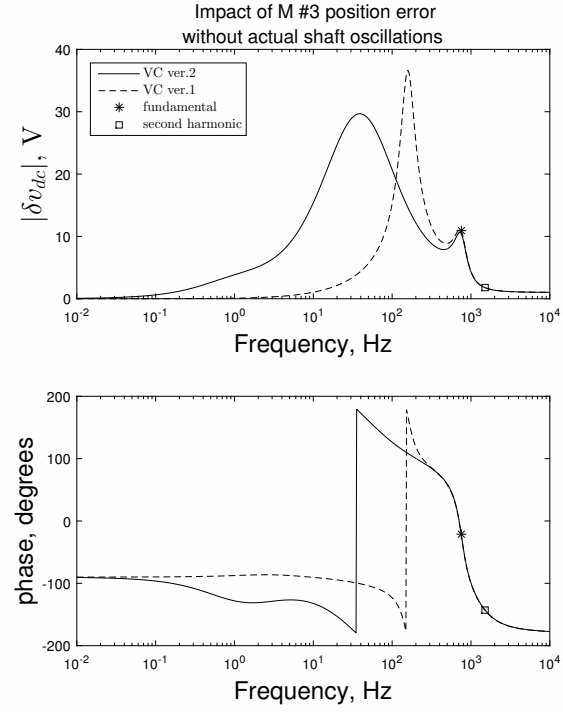

(d)

Fig. 3.4. Bode plots for case study 4 (Model 1).

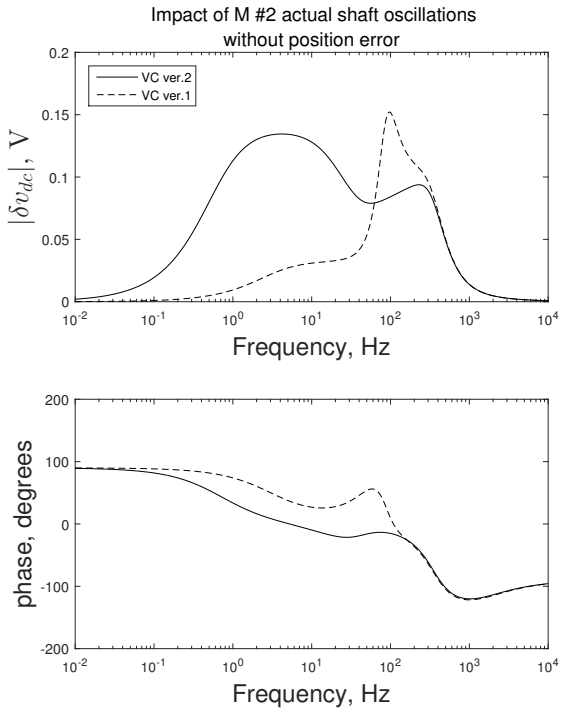

(a)

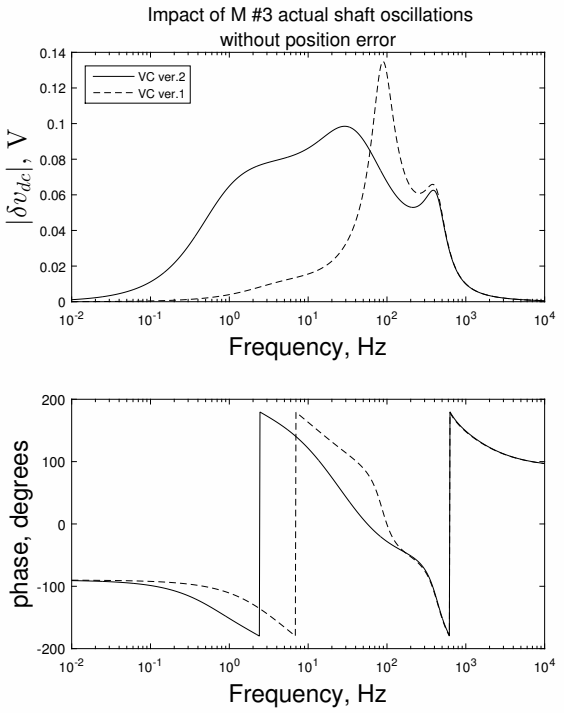

(b)

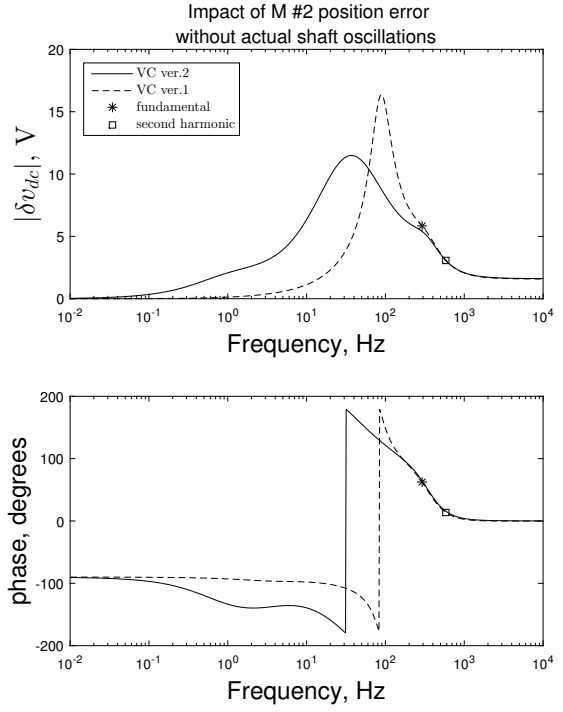

(c)

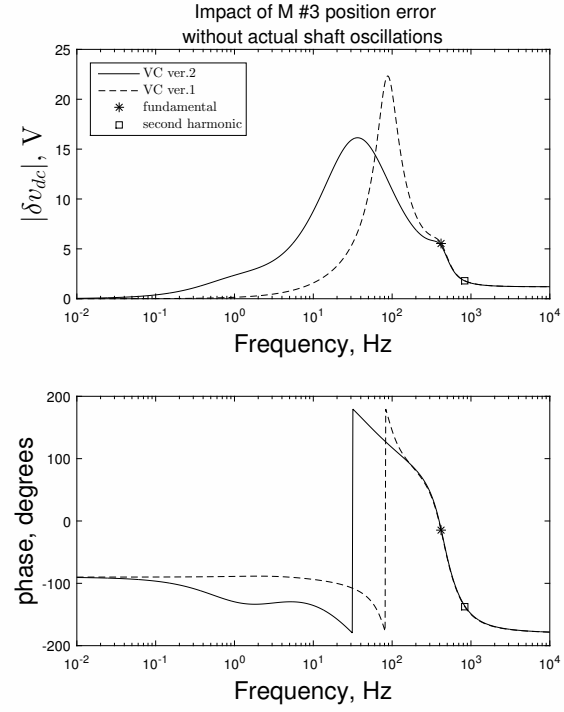

(d)

Fig. 3.5. Bode plots for case study 5 (Model 1).

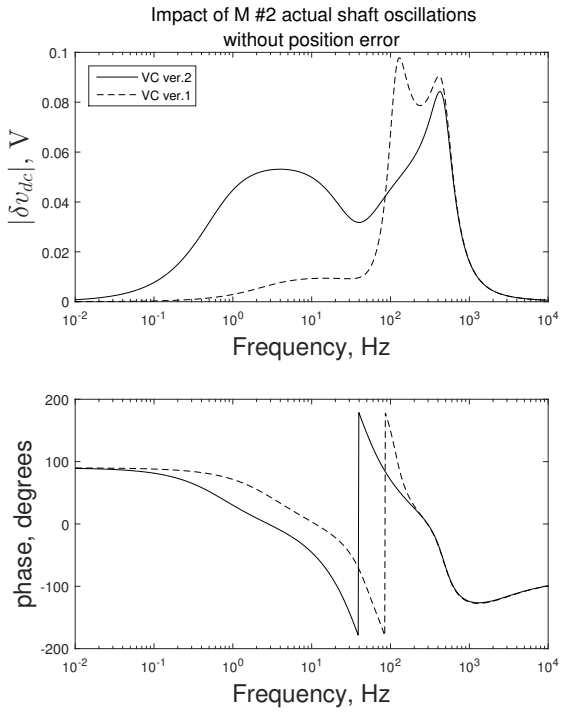

(a)

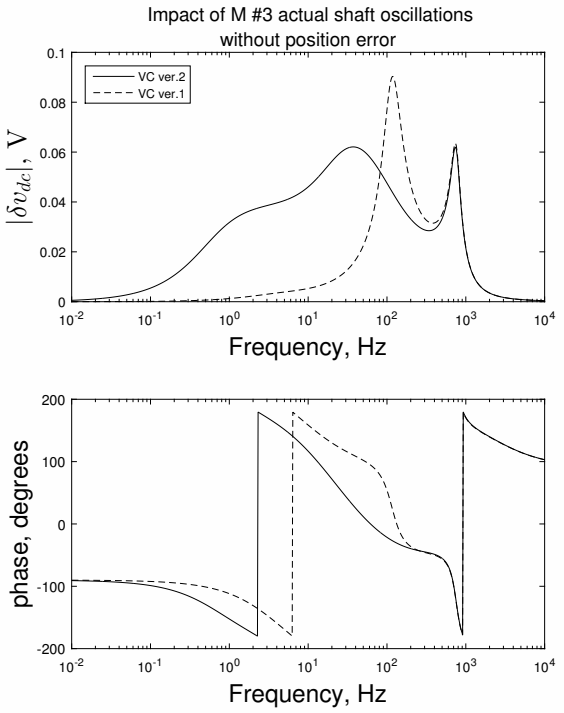

(b)

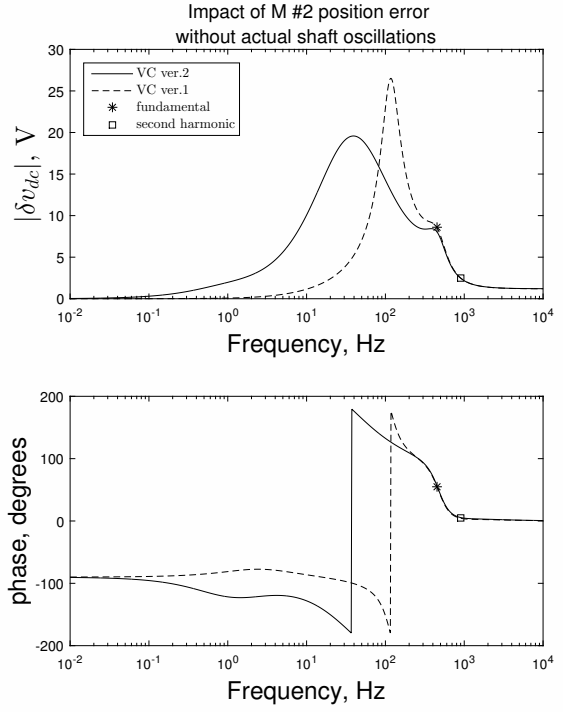

(c)

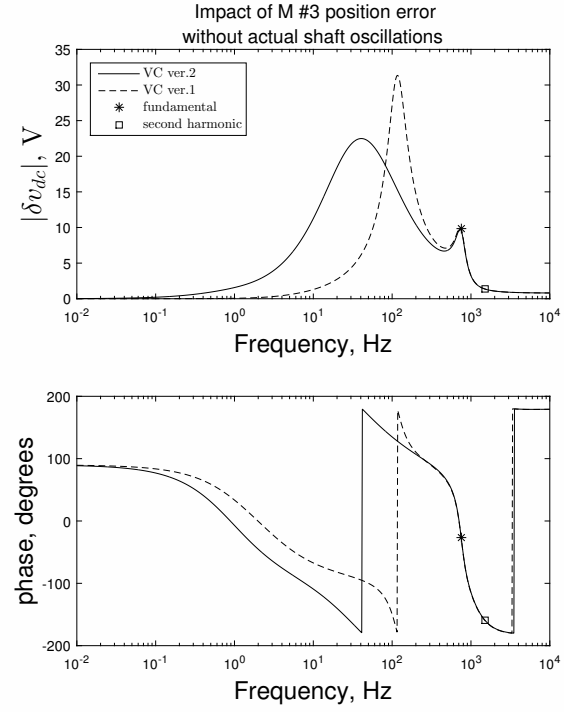

(d)

Fig. 3.6. Bode plots for case study 6 (Model 1).

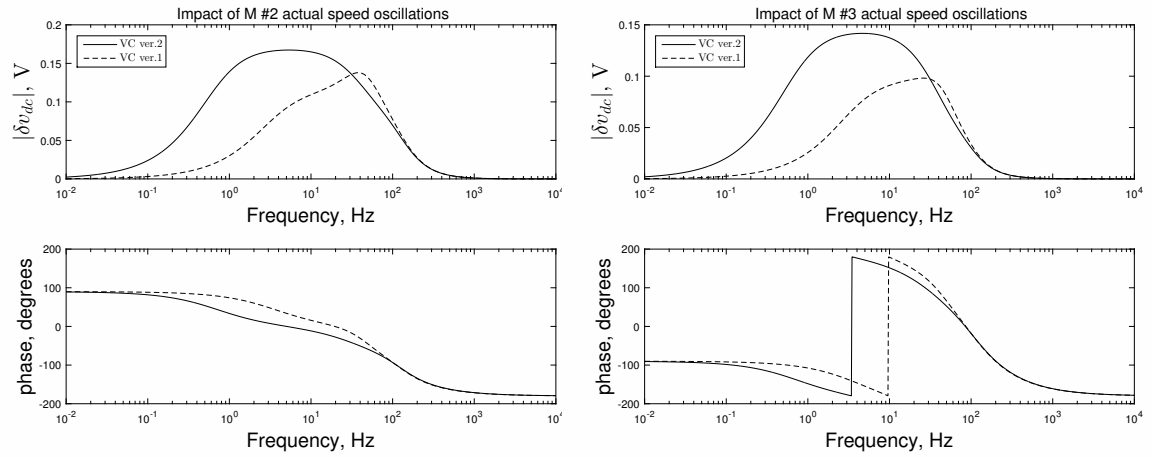

(a)

(b)

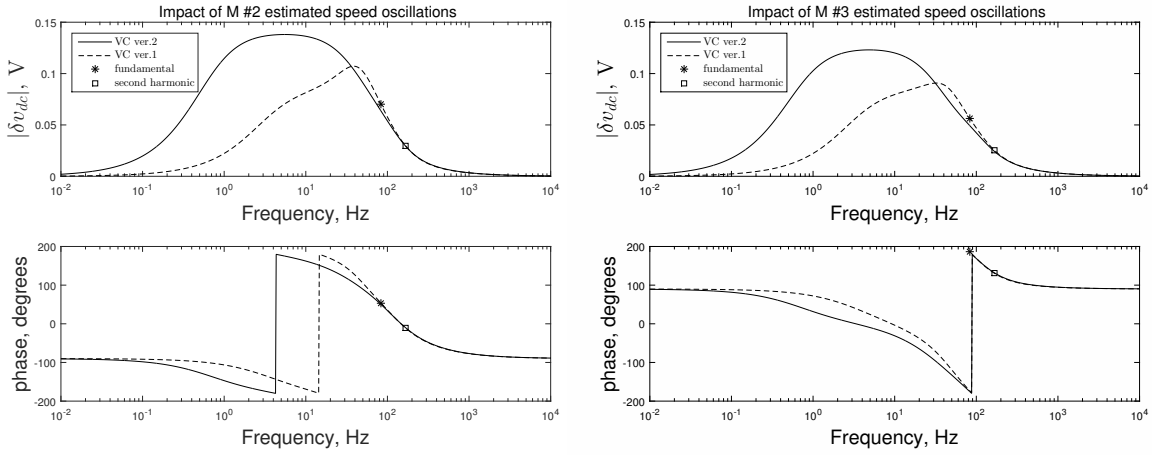

(c)

(d)

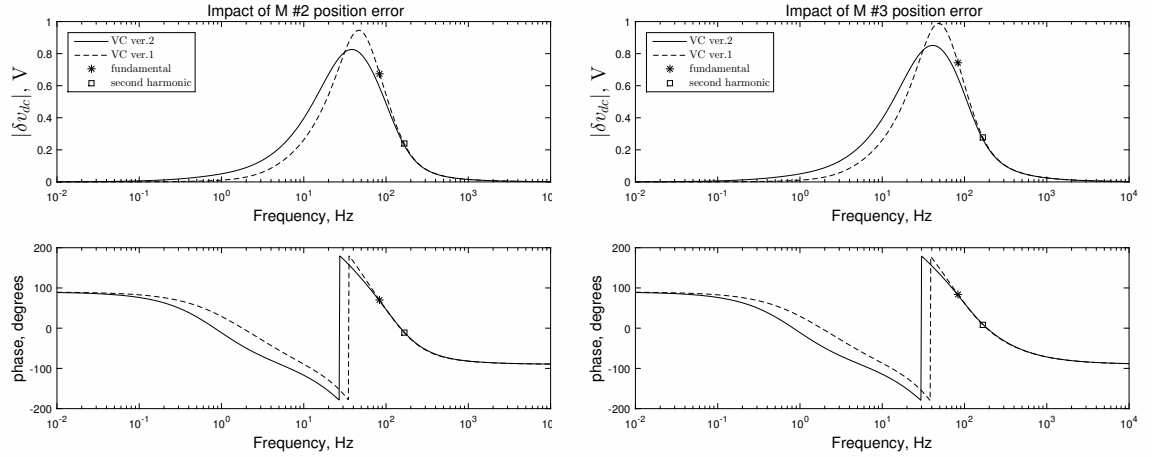

(e)

(f)

Fig. 3.7. Bode plots for case study 1 (Model 2).

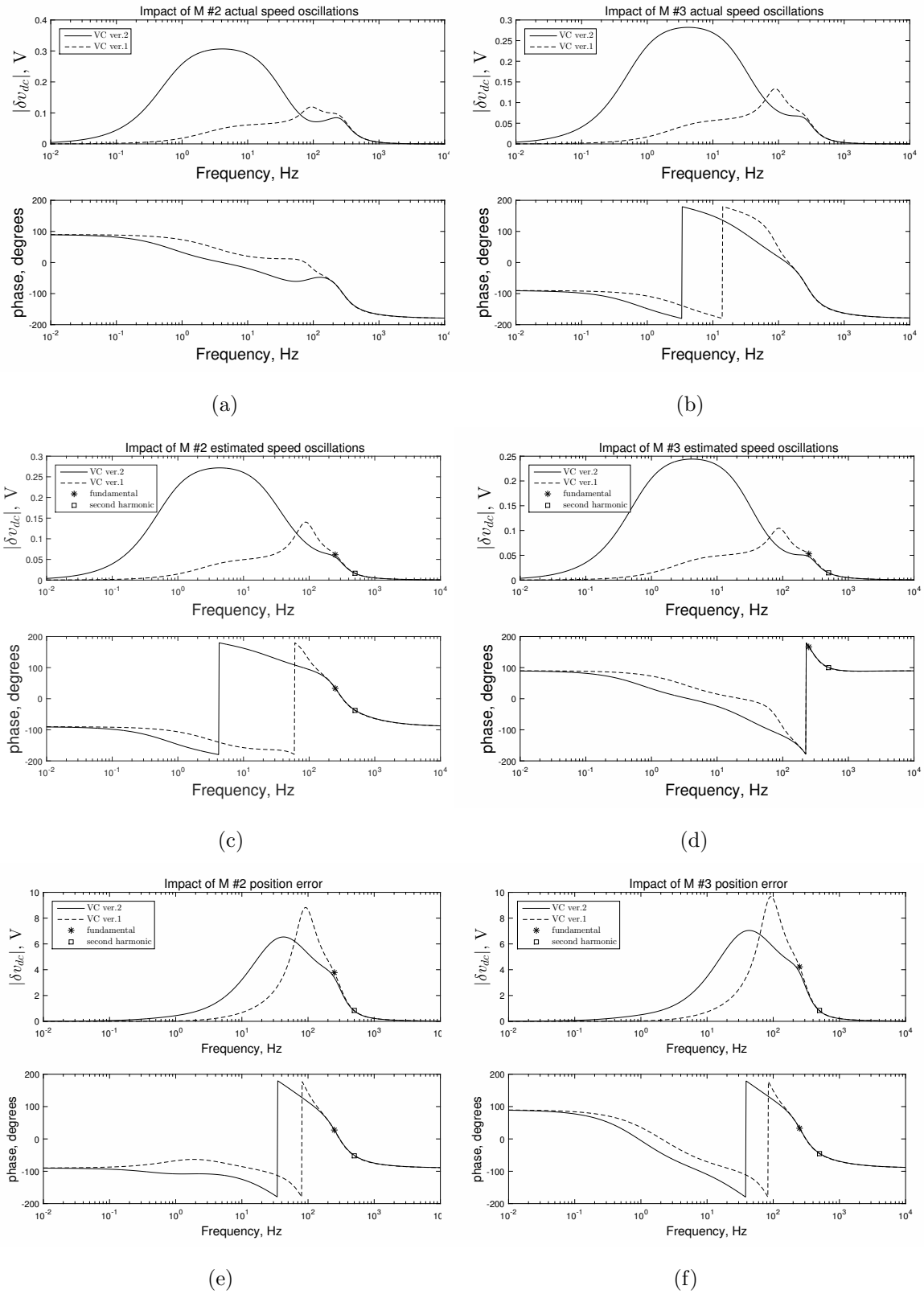

Fig. 3.8. Bode plots for case study 2 (Model 2).

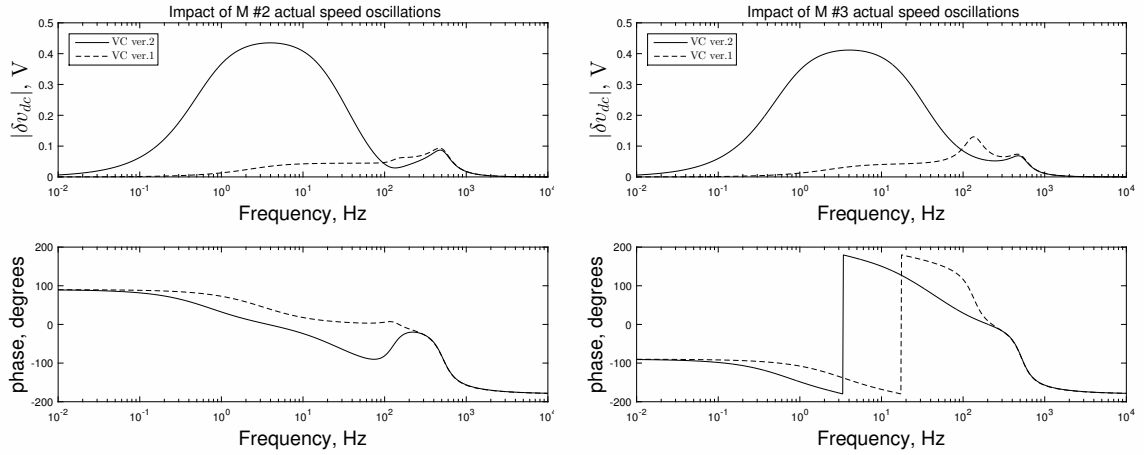

(a)

(b)

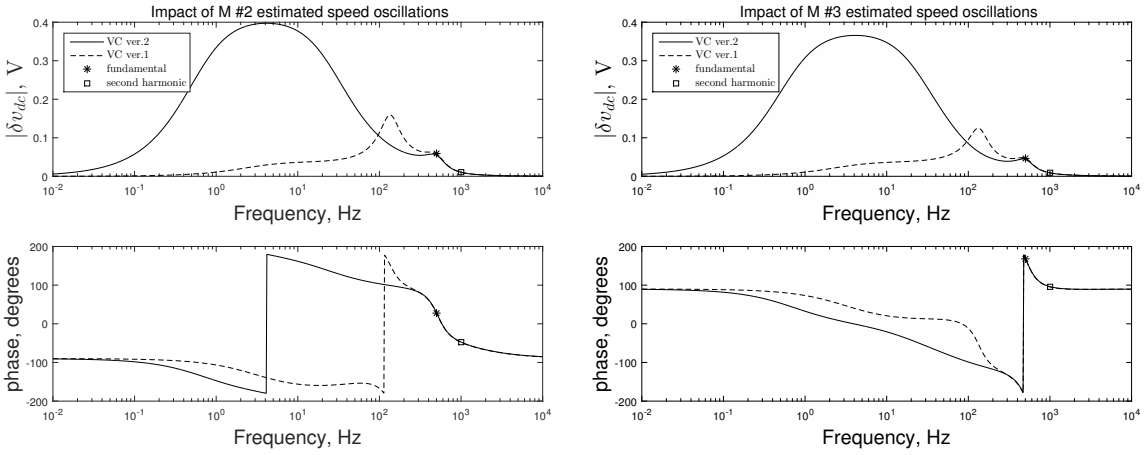

(c)

(d)

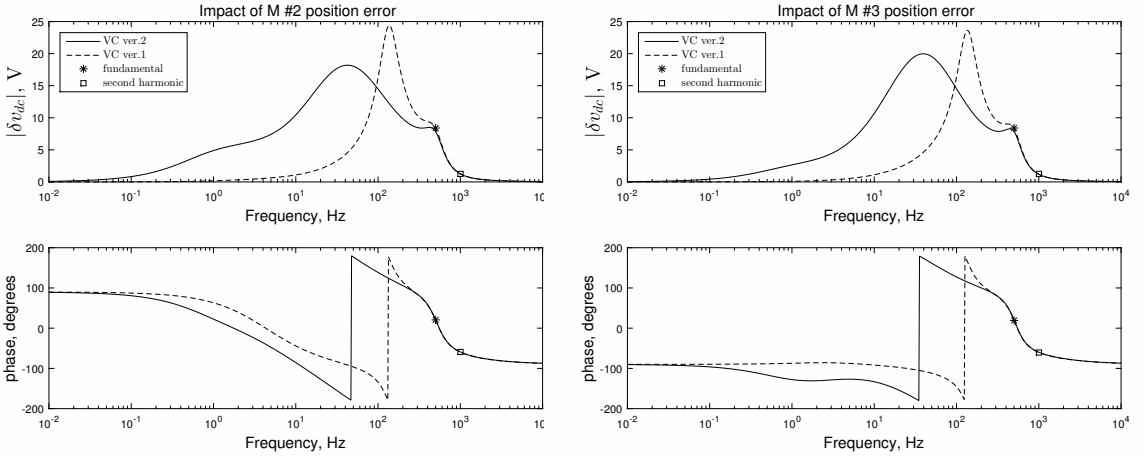

(e)

(f)

Fig. 3.9. Bode plots for case study 3 (Model 2).

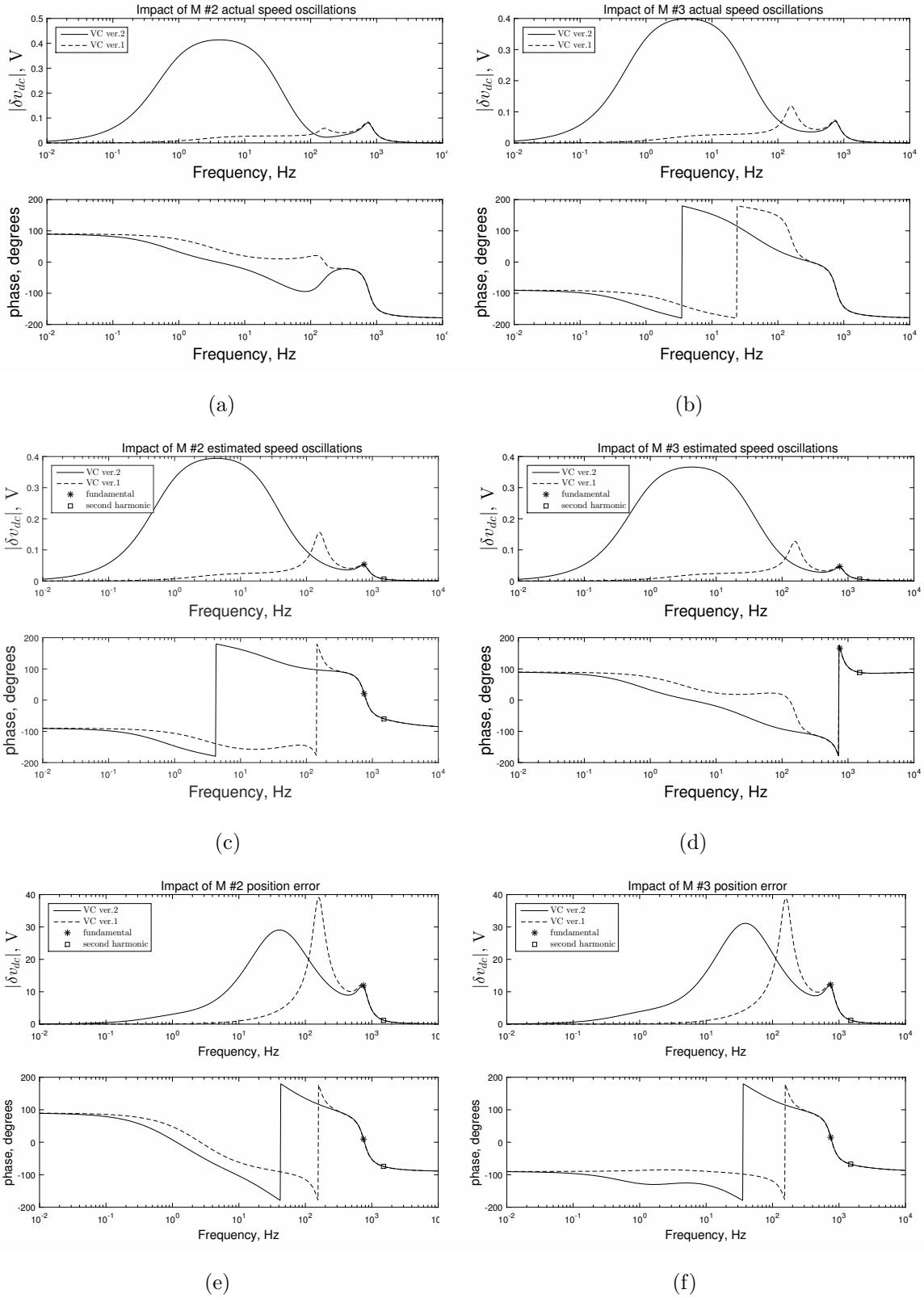

Fig. 3.10. Bode plots for case study 4 (Model 2).

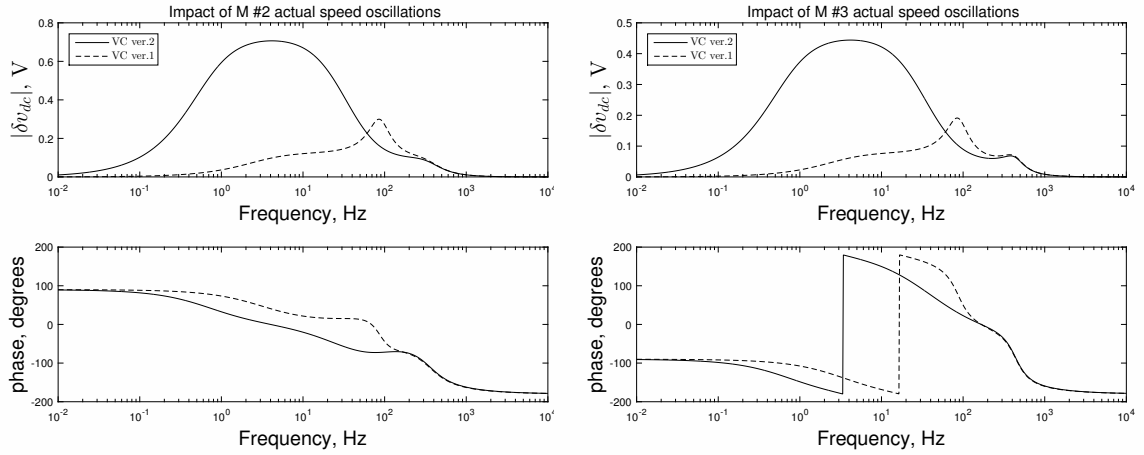

(a)

(b)

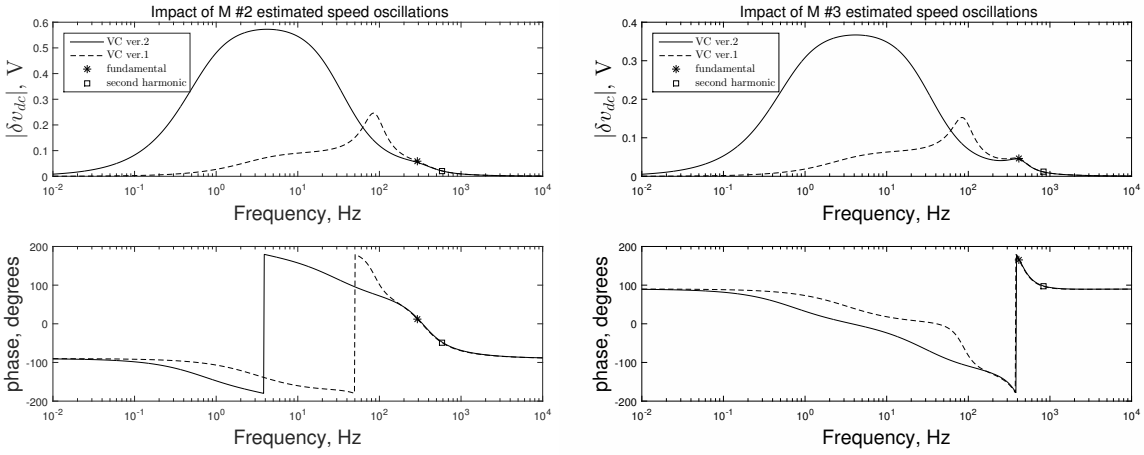

(c)

(d)

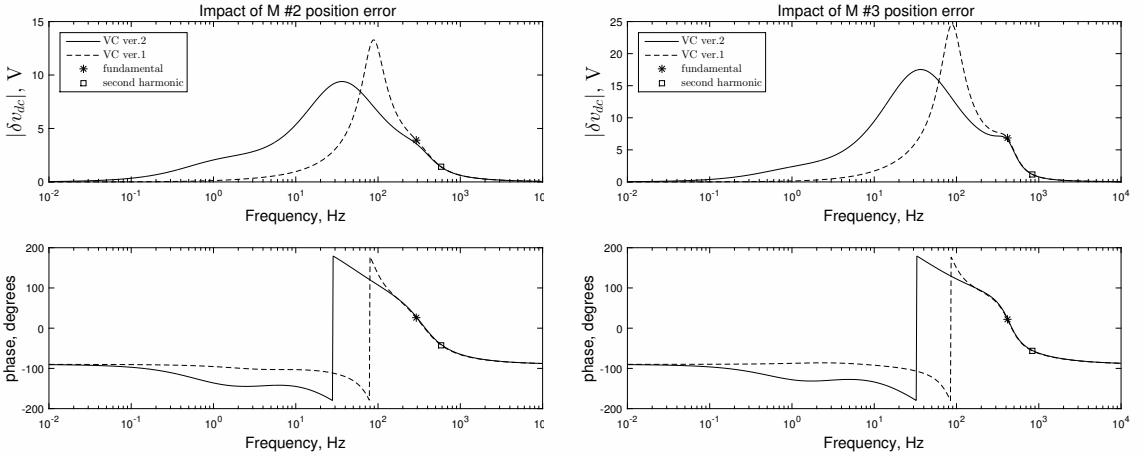

(e)

(f)

Fig. 3.11. Bode plots for case study 5 (Model 2).

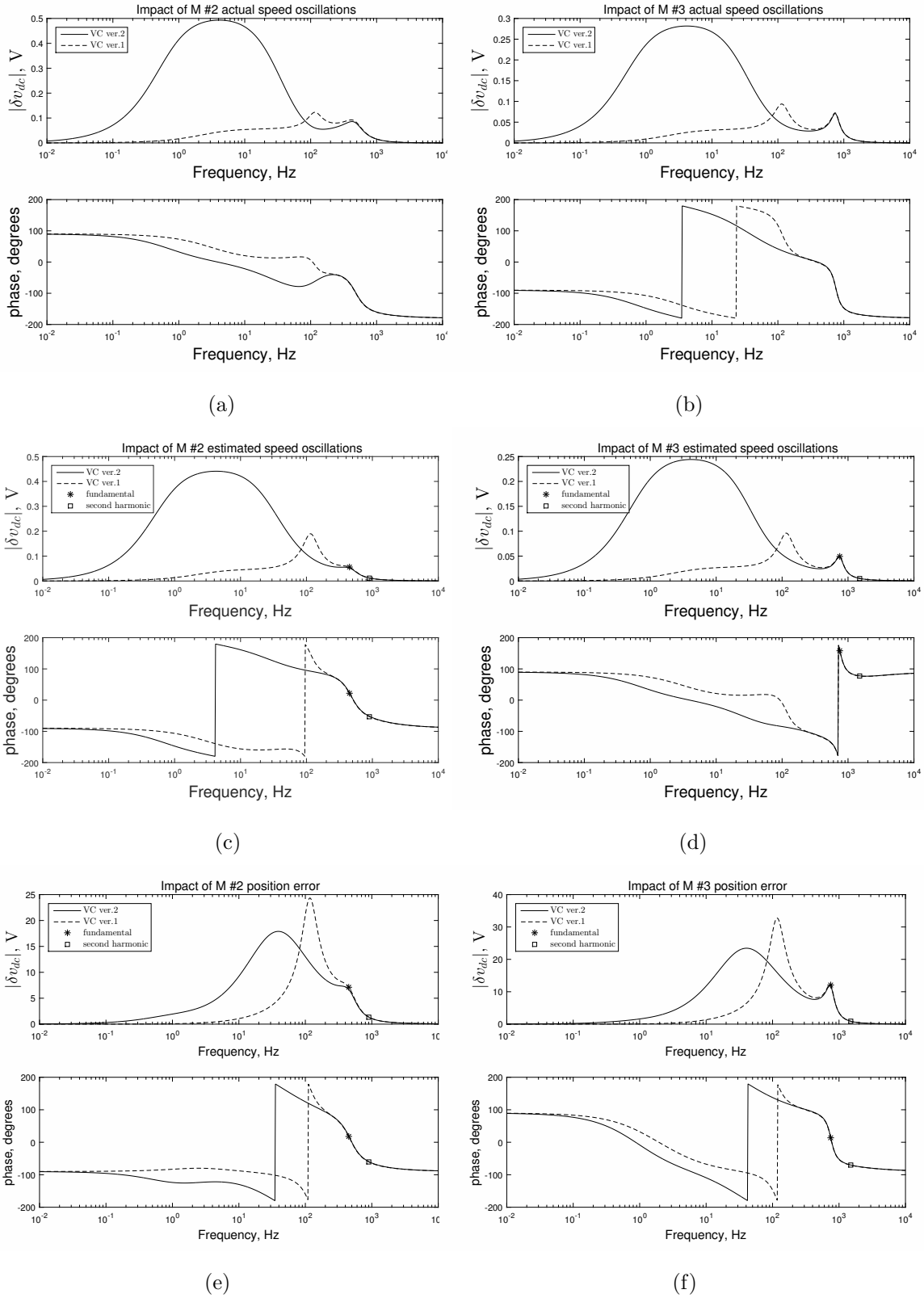

Fig. 3.12. Bode plots for case study 6 (Model 2).

3.2 Impact of Position Error Over Operating Range

The second set of results shows the impact of position error over a wide operating range, which is obtained by varying load torque and speed (assuming both machines have the same rpm). They are conducted for Model 2 with version 1 of voltage controller and setting all other disturbances to zero. For example, for position error occurring in the resolver of machine 2, (2.135) yields

$$\delta v_{dc}(s) = H_3(s)\, e_{\theta 2}(s)\,. \tag{3.3}$$

The analysis is performed assuming a 1° position error magnitude occurring either at the fundamental or at the second harmonic. The results are depicted in Fig. 3.13 over a range of rotor speed from 2000 to 9000 rpm in steps of 500 rpm. The load torque at each speed is varied in steps of 10 Nm starting from 50 Nm and ending at the maximum possible torque at that particular speed. (The upper bound for torque is determined by the motor characterization data range; see Appendix A for details.)

3.3 Impact of Slot Harmonics Over Operating Range

Thirdly, we investigate the impact of the slot harmonics on the dc-link voltage oscillations. The operating range is identical to the one described in the previous subsection (Sec. 3.2). The test is conducted for Model 2 with version 1 of voltage controller. The back-emf time-domain waveforms corresponding to the slot harmonics are obtained from (2.99) and (2.100) for any given speed. For example, the impact of machine-2 slot harmonics on the dc-link voltage is computed by superposition using (2.134)[1],

$$\delta v_{dc}(s) = H_3(s)\, \delta v_{qh2}(s) + H_4(s)\, \delta v_{dh2}(s)\,. \tag{3.4}$$

As the machine considered in this case study has 12 slots per pole pair, the dominant slot harmonics appear at the 6^{th} and 12^{th} order. The impact of these harmonics is

[1]Note that the impact of slot harmonics on dc link is same for both Model 1 and Model 2.

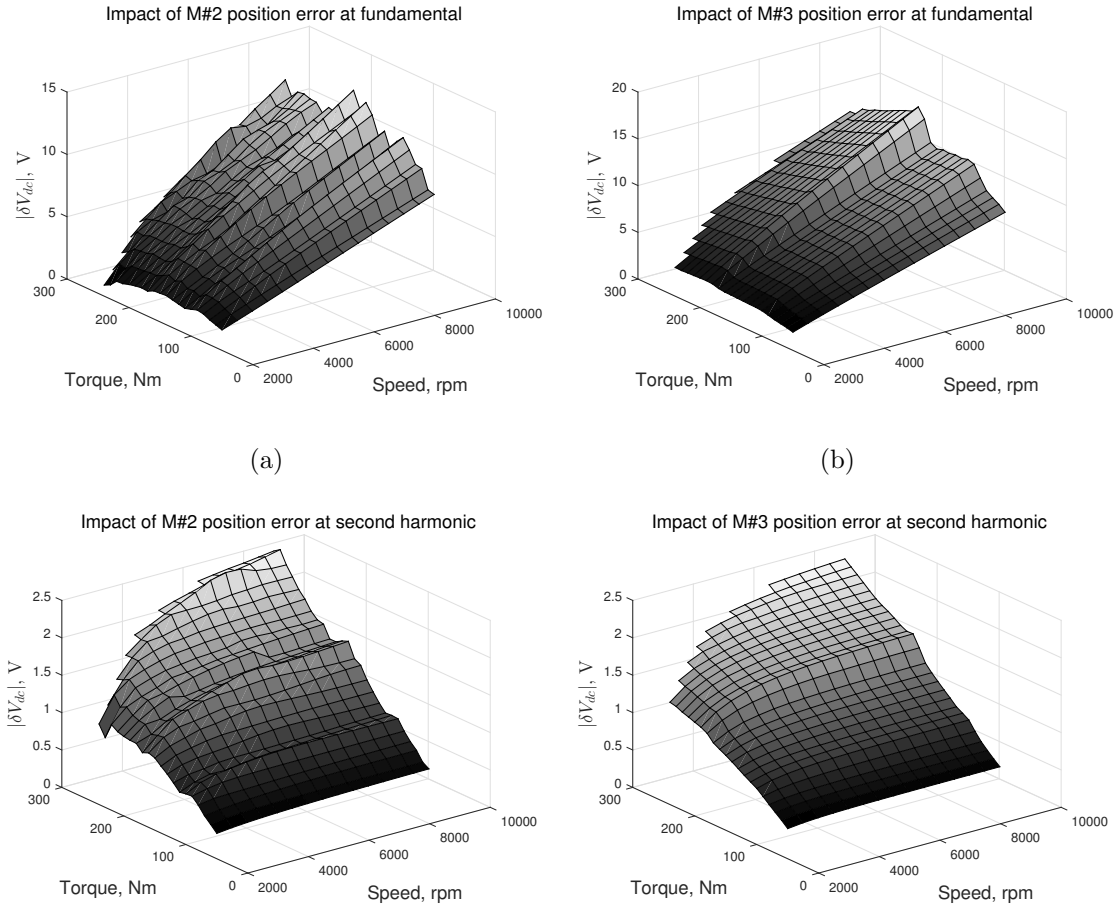

Fig. 3.13. Variation of dc-link oscillations for 1° position error over an operating range ($R_v = 5r_s, \omega_{bi} = 2\pi 80$ Hz).

shown in Fig. 3.14. It can be observed that the slot harmonic impact is insignificant, since the dc-link voltage ripple does not exceed 0.4 V over the operating range.

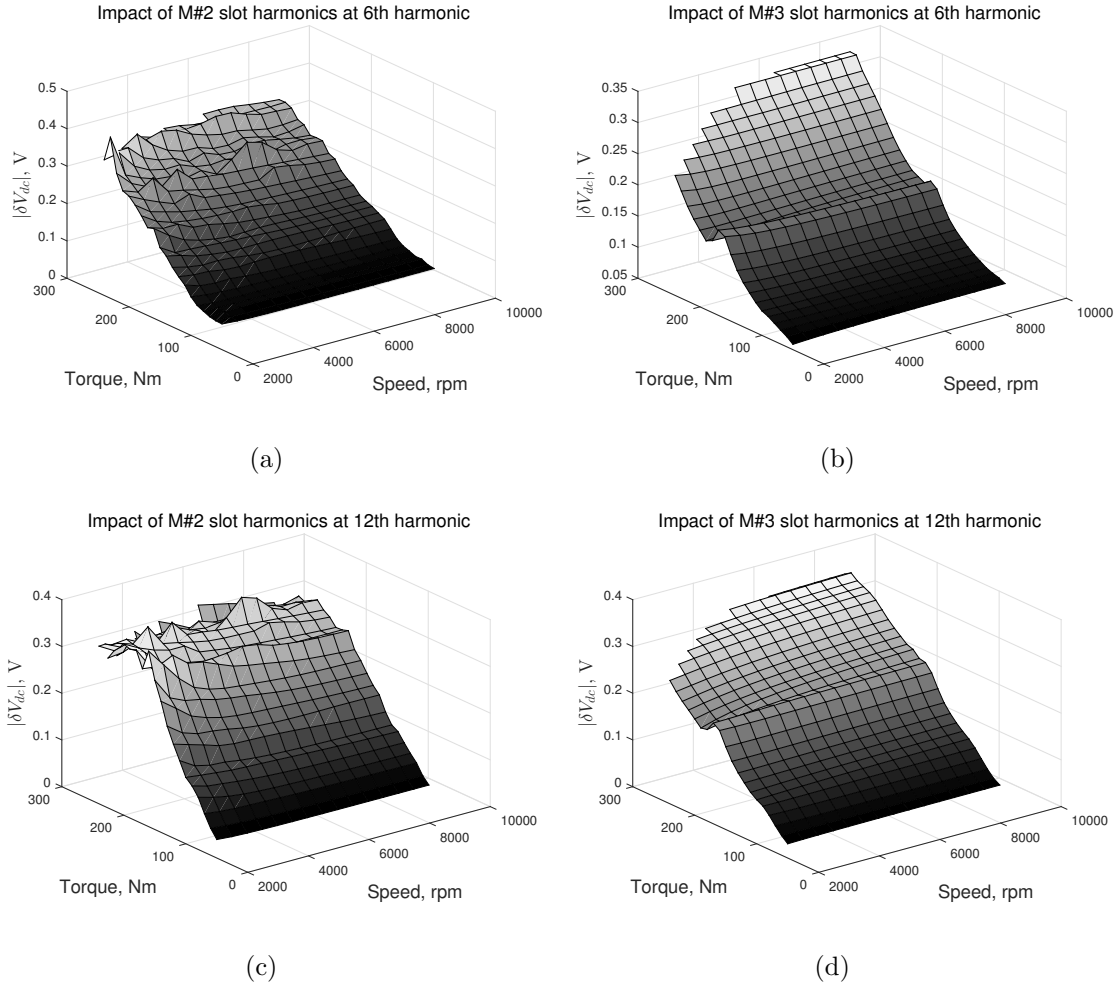

Fig. 3.14. Impact of slot harmonics on dc-link voltage oscillations over an operating range.

4. TECHNIQUES TO MITIGATE DC-LINK OSCILLATIONS

4.1 Elimination of Position Error

Position error commonly occurs at fundamental and second harmonic due to imperfections in resolver manufacturing as discussed in Section 1.1. It can be inferred from Fig. 3.13 that the position error has significant effect on dc-link voltage at these particular frequencies over the entire operating range. One of the potential ways to reduce these oscillations is to eliminate the position error at the source itself.

4.1.1 Elimination of Fundamental Position Error

This section sets forth a resolver position error elimination technique assuming that only a fundamental component in position error exists. This situation is illustrated in Fig. 4.1, where $\theta_r = 2\pi t$ rad, corresponding to a constant rotor speed of 2π rad/s, with $\alpha = 0.52$ rad and $\beta = 0.3$ rad. In general, the measured position signal can be represented as

$$\hat{\theta}_r = \theta_r + \underbrace{\alpha \cos\theta_r + \beta \sin\theta_r}_{\epsilon} \tag{4.1}$$

where ϵ is measurement error. The proposed algorithm first computes the coefficients α and β. Then, the position error is estimated and subtracted from the estimated position signal in order to obtain a corrected position signal.

To find the coefficients α and β, we first compute

$$\cos\hat{\theta}_r = \cos(\theta_r + \epsilon) = \cos\theta_r \cos\epsilon - \sin\theta_r \sin\epsilon\,. \tag{4.2}$$

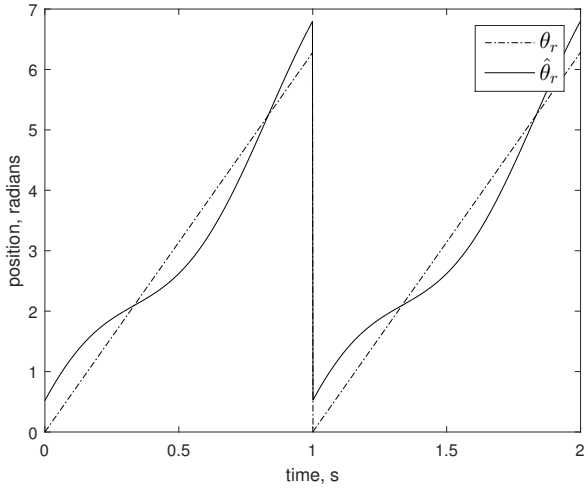

Fig. 4.1. Position signal variation example.

As ϵ is very small, the following approximations are valid: $\cos\epsilon \approx 1$ and $\sin\epsilon \approx \epsilon$. The above equation reduces to

$$\cos\hat{\theta}_r \approx \cos\theta_r - \epsilon \sin\theta_r \,. \tag{4.3}$$

Substituting ϵ from (4.1) results in

$$\cos\hat{\theta}_r \approx \cos\theta_r - (\alpha\cos\theta_r + \beta\sin\theta_r)\sin\theta_r \,. \tag{4.4}$$

Using trigonometric identities from Appendix C,

$$\cos\hat{\theta}_r \approx \cos\theta_r - \frac{\alpha}{2}\sin 2\theta_r - \frac{\beta}{2}(1-\cos 2\theta_r) \,. \tag{4.5}$$

Similarly, computing $\sin\hat{\theta}_r$ with the above approximations yields

$$\sin\hat{\theta}_r = \sin\theta_r\cos\epsilon + \cos\theta_r\sin\epsilon \approx \sin\theta_r + \epsilon\cos\theta_r \tag{4.6}$$

$$\sin\hat{\theta}_r \approx \sin\theta_r + (\alpha\cos\theta_r + \beta\sin\theta_r)\cos\theta_r \tag{4.7}$$

$$\sin\hat{\theta}_r \approx \sin\theta_r + \frac{\alpha}{2}(1+\cos 2\theta_r) + \frac{\beta}{2}\sin 2\theta_r \tag{4.8}$$

The coefficients α and β are obtained by low-pass filtering the signals from equations (4.8) and (4.5), respectively, to eliminate all oscillatory zero-mean components, i.e.,

$$\alpha = 2\ f_{\text{LPF}}\left(\sin\hat{\theta}_r\right) \tag{4.9}$$

$$\beta = -2\ f_{\text{LPF}}\left(\cos\hat{\theta}_r\right) \tag{4.10}$$

where f_{LPF} represents a low-pass filter function. For example, a first-order low-pass filter with time constant τ is expressed in the frequency domain as: $f_{\text{LPF}}(x) = x/(\tau s + 1)$. Note that this method will work properly during operation under constant rotor speed, which eliminates the time-average of $\sin\theta_r$, $\cos\theta_r$, $\sin 2\theta_r$, and $\cos 2\theta_r$. For more details see Sec. 4.1.5. Also, while implementing this method in hardware, we should limit the values of α and β to around 0.0349 rad (which corresponds to a 2° position error). Otherwise, these variables could integrate to high values (e.g., while the motor is at standstill), thus leading to instability (e.g., during motor start-up).

After the coefficients are calculated, the position error can be estimated as $\hat{\epsilon} \approx \alpha\cos\hat{\theta}_r + \beta\sin\hat{\theta}_r$. This approximation is valid because

$$\hat{\epsilon} = \alpha\cos(\theta_r + \epsilon) + \beta\sin(\theta_r + \epsilon) \tag{4.11}$$

$$\approx \alpha(\cos\theta_r + \epsilon\sin\theta_r) + \beta(\sin\theta_r + \epsilon\cos\theta_r)\,. \tag{4.12}$$

Substituting ϵ from (4.1), we get

$$\hat{\epsilon} \approx \alpha\cos\theta_r + \beta\sin\theta_r + \underbrace{\frac{\alpha^2+\beta^2}{2}\sin 2\theta_r + \alpha\beta}_{<<1} \approx \epsilon\,. \tag{4.13}$$

The position signal is corrected by subtracting the estimated error from the estimated position:

$$\hat{\hat{\theta}}_r = \hat{\theta}_r - \hat{\epsilon} \tag{4.14}$$

$$= \hat{\theta}_r - \alpha\cos\hat{\theta}_r - \beta\sin\hat{\theta}_r\,. \tag{4.15}$$

It should be noted that the α, β coefficients converge depending on the time constant of the low-pass filter. Hence, the estimated position signal is gradually corrected at the same rate.

4.1.2 Extension to Eliminate any Harmonic

The above algorithm may be extended to eliminate any desired harmonic component occurring in the position error. Suppose that the estimated position signal is expressed as

$$\hat{\theta}_r = \theta_r + \underbrace{\sum_{x \in X} \alpha_x \cos x\theta_r + \beta_x \sin x\theta_r}_{\epsilon} \tag{4.16}$$

where x represents the harmonic number of a particular error component, and X is the set of harmonics, e.g., $X = \{1, 2, \ldots\}$, which do not necessarily have to be of integer order.

To eliminate the y^{th} harmonic component from this position signal, we compute $\cos y\hat{\theta}_r$ and $\sin y\hat{\theta}_r$ with the approximations $\cos y\epsilon \approx 1$ and $\sin y\epsilon \approx y\epsilon$:

$$\begin{aligned}
\cos y\hat{\theta}_r &\approx \cos y\theta_r - y\epsilon \sin y\theta_r && (4.17)\\
&\approx \cos y\theta_r - y \sum_x \alpha_x \sin y\theta_r \cos x\theta_r + \beta_x \sin y\theta_r \sin x\theta_r && (4.18)\\
&\approx \cos y\theta_r - y \sum_x \frac{\alpha_x}{2} \left[\sin(x+y)\theta_r + \sin(y-x)\theta_r\right] \\
&\qquad + \frac{\beta_x}{2} \left[\cos(x-y)\theta_r - \cos(x+y)\theta_r\right] . && (4.19)
\end{aligned}$$

The only dc component in the above expression corresponds to the term in the sum where x equals y. Therefore, we can express

$$\cos y\hat{\theta}_r \approx (\text{oscillatory terms}) - \frac{y\beta_x}{2} . \tag{4.20}$$

Similarly,

$$\begin{aligned}
\sin y\hat{\theta}_r &\approx \sin y\theta_r + y\epsilon \cos y\theta_r && (4.21)\\
&\approx \sin y\theta_r + y \sum_x \alpha_x \cos y\theta_r \cos x\theta_r + \beta_x \cos y\theta_r \sin x\theta_r && (4.22)\\
&\approx \sin y\theta_r + y \sum_x \frac{\alpha_x}{2} \left[\cos(x+y)\theta_r + \cos(x-y)\theta_r\right] \\
&\qquad + \frac{\beta_x}{2} \left[\sin(x+y)\theta_r + \sin(x-y)\theta_r\right] . && (4.23)
\end{aligned}$$

The only dc component appears when $x = y$ in the sum, so

$$\sin y\hat{\theta}_r \approx (\text{oscillatory terms}) + \frac{y\alpha_x}{2}\,. \tag{4.24}$$

Therefore, the coefficients of the y^{th} harmonic error in position can be computed by low-pass filtering $\cos y\hat{\theta}_r$ and $\sin y\hat{\theta}_r$:

$$\alpha_x = \frac{2}{y}\, f_{\text{LPF}}\left(\sin y\hat{\theta}_r\right) \tag{4.25}$$

$$\beta_x = -\frac{2}{y}\, f_{\text{LPF}}\left(\cos y\hat{\theta}_r\right) \tag{4.26}$$

The position error due to the y^{th} harmonic is then estimated by

$$\hat{\epsilon}_y \approx \alpha_y \cos y\hat{\theta}_r + \beta_y \sin y\hat{\theta}_r \tag{4.27}$$

which is subsequently subtracted from the original position signal. In general, the total position error can be estimated using

$$\hat{\epsilon} = \sum_{y\in Y} \hat{\epsilon}_y \tag{4.28}$$

where the set $Y \subset X$ contains the harmonics that are targeted. A block diagram representing elimination of fundamental and second harmonic error components is shown in Fig. 4.2.

4.1.3 Low-Pass Filter Bandwidth

This section discusses the selection of bandwidth of the low-pass filter. The frequency response of a first-order low-pass filter with bandwidth ω_{lpf}, which corresponds to a time constant $\tau = 1/\omega_{\text{lpf}}$, is shown in Fig. 4.3. As a rule of thumb, the bandwidth of the low-pass filter should be selected such that it is at least 10 times smaller than the minimum frequency of all components of interest in the position error that are to be eliminated. Of course, this depends on the lowest operating speed. This can be expressed as follows:

$$\omega_{\text{min}} > 10\omega_{\text{lpf}}\,. \tag{4.29}$$

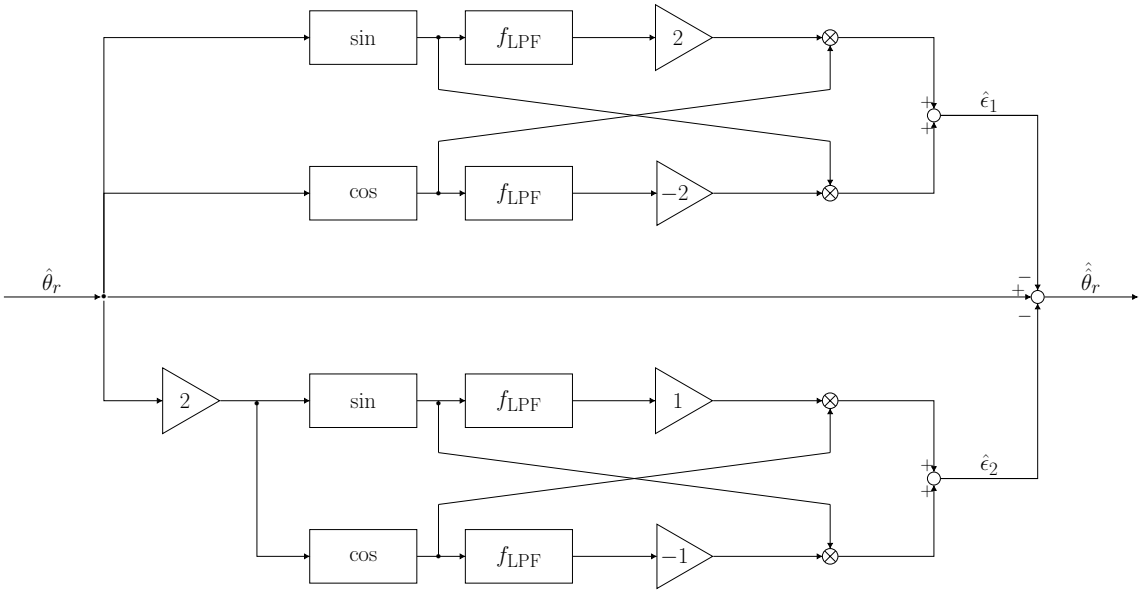

Fig. 4.2. Block diagram of position error elimination for 2 harmonics.

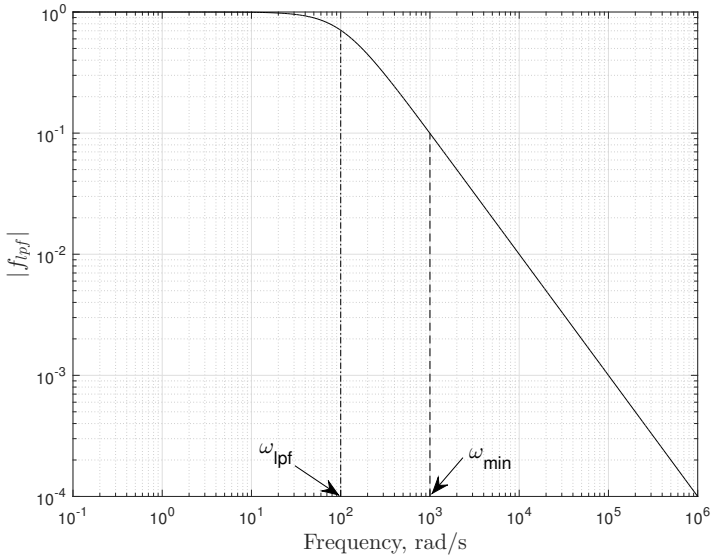

Fig. 4.3. Frequency response of a first-order low-pass filter.

4.1.4 Simulation Results

We illustrate the technique with a time-domain simulation study at an arbitrarily selected operating point. To focus solely on the impact of position error on dc-

link, all other disturbances are ignored. An operating point of 9000 rpm (equal for both machines) and 150 Nm load torque is considered. The speed corresponds to a fundamental frequency of 4.7 $\times 10^3$ rad/s (750 Hz). The test is conducted for Model 2 with version 1 of voltage controller. A position error in both machines (M2 and M3) is synthesized using the following (arbitrarily selected) values for the fundamental components: $\alpha_{M2} = 0.5°$, $\beta_{M2} = 1.5°$, $\alpha_{M3} = 1°$, and $\beta_{M3} = 2°$. The time constant of all low-pass filters is $\tau = 5$ s which corresponds to a bandwidth $\omega_{\text{lpf}} = 0.2$ rad/s. In this case, $\omega_{\min}/\omega_{\text{lpf}} = 2.3 \times 10^4$, and satisfies the condition (4.29). Figs. 4.4(a)–4.4(d) illustrate the convergence of coefficients α and β for both machines. Also, the positive impact of eliminating the position error on the dc-link voltage oscillations is observed in Fig. 4.5(a). A second study is performed using the same parameters as discussed above except the time constant of all low-pass filters, which is now 0.01 s. In this case, the ratio $\omega_{\min}/\omega_{\text{lpf}}$ is 47.1. The dc-link voltage oscillations for this case are observed in Fig. 4.5(b).

4.1.5 Impact of Rotor Shaft Oscillations

Let us suppose that rotor shaft oscillations are occurring at fundamental electrical frequency (induced by a position error at the same frequency). The rotor position can be expressed as

$$\theta_r = \theta_{r0} + \underbrace{\gamma \cos\theta_{r0} + \delta \sin\theta_{r0}}_{\delta\theta_r} . \tag{4.30}$$

The angle θ_{r0} corresponds to a linearly increasing angle due to a nominal constant rotor speed. Substituting the above equation in (4.8), we obtain

$$\sin\hat{\theta}_r \approx \sin\left(\theta_{r0} + \delta\theta_r\right) + \frac{\alpha}{2}\left[1 + \cos 2(\theta_{r0} + \delta\theta_r)\right] + \frac{\beta}{2}\sin 2(\theta_{r0} + \delta\theta_r) . \tag{4.31}$$

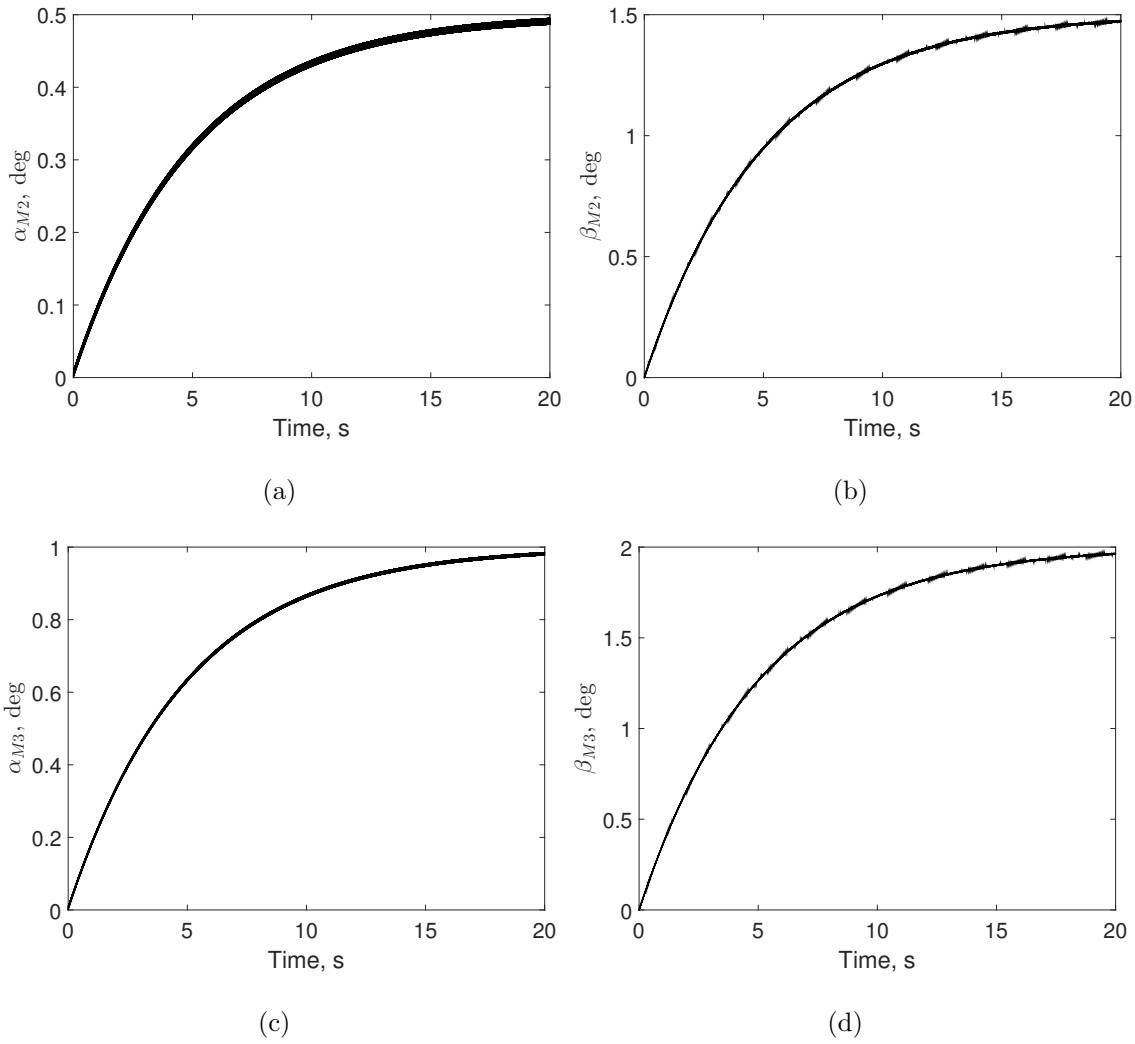

Fig. 4.4. Convergence of α and β in both machines.

Considering the small-angle approximations $\cos\delta\theta_r \approx 1$ and $\sin\delta\theta_r \approx \delta\theta_r$, and neglecting higher-order terms, leads to

$$\sin\hat{\theta}_r \approx \sin\theta_{r0} + \delta\theta_r\cos\theta_{r0} + \frac{\alpha}{2}(1+\cos 2\theta_{r0}) + \frac{\beta}{2}\sin 2\theta_{r0} \tag{4.32}$$

$$\approx \sin\theta_{r0} + (\gamma\cos\theta_{r0} + \delta\sin\theta_{r0})\cos\theta_{r0} + \frac{\alpha}{2}(1+\cos 2\theta_{r0}) + \frac{\beta}{2}\sin 2\theta_{r0} \tag{4.33}$$

$$\approx \sin\theta_{r0} + \frac{\gamma+\alpha}{2}(1+\cos 2\theta_{r0}) + \frac{\delta+\beta}{2}\sin 2\theta_{r0}\,. \tag{4.34}$$

It is observed that oscillations in rotor speed can affect the estimation of the α and β coefficients.

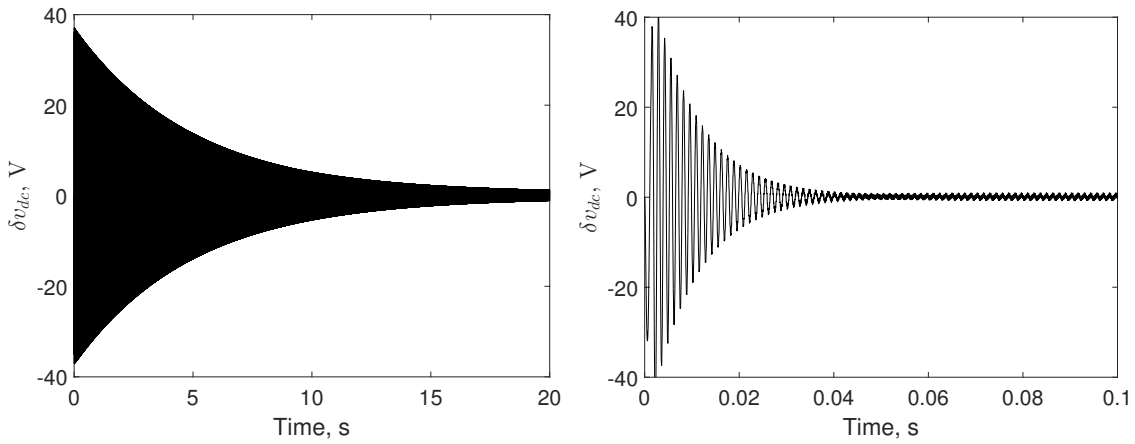

(a) $\tau = 5\ s$ (b) $\tau = 0.01\ s$

Fig. 4.5. Reduction of dc-link voltage oscillations.

We proceed to obtain approximate upper bounds for γ and δ, by estimating a maximum possible value of the amplitude of $\delta\theta_r$. The mechanical dynamics of the system are described by

$$T_e - T_l = J\frac{d}{dt}\omega_{rm} \tag{4.35}$$

where T_e is the electromagnetic torque, T_l is the load torque (assumed constant here), J is the moment of inertia, and ω_{rm} is the mechanical rotor speed. The small-signal version of the above equation is

$$\delta T_e = J\frac{d}{dt}\delta\omega_{rm}\,. \tag{4.36}$$

As the oscillations in the actual speed occur at fundamental electrical frequency, switching to the frequency domain yields (with slight abuse of notation)

$$\delta T_e = J\omega_e\delta\omega_{rm}e^{j\frac{\pi}{2}} \tag{4.37}$$

$$= J\omega_e^2\delta\theta_{rm}e^{j\pi} \tag{4.38}$$

$$= -\,J\omega_e^2\delta\theta_r\frac{1}{pp} \tag{4.39}$$

where $pp = 5$ represents the number of pole-pairs of the machine. The magnitude of $\delta\theta_r$ is, therefore,

$$|\delta\theta_r| = \frac{pp\ \delta T_e}{J\omega_e^2} \tag{4.40}$$

The machine in this case study has a rated torque of 350 Nm and a moment of inertia of drivetrain of approximately 0.3 kg·m^2. The oscillations in torque are assumed to be around 3% of the rated torque. We compute $\delta\theta_r$ considering a low speed of 500 rpm as a worst-case scenario. Substituting the aforementioned parameters in (4.40), we obtain $|\delta\theta_r| = 0.0026$ rad, which is approximately 7 times smaller than a typical position error magnitude (1°). Hence, it may be concluded that the impact of shaft oscillations is relatively small compared to the position error.

Note that the shaft oscillations are caused due to torque oscillations which in turn are due to the position error. Therefore, as the error in the position converges to zero, the shaft oscillations are also expected to converge to zero as well.

4.1.6 Experimental Results

For this experiment, the Machine 2 and Machine 3 are connected to a 700-V dc-link through a dual inverter. The test was conducted at an operating point running the Machine 2 and Machine 3 at a fundamental frequency of 400 Hz and 200 Hz, respectively. This test was focused on eliminating only the fundamental component of position error in both of the machines. Note that the speed estimation was still computed using the polluted position signal that contains the error. The time-domain dc-link voltage waveform with and without position error compensation is shown in Figs. 4.6(a) and 4.6(b). The spectrum of the dc-link voltage is observed in Figs. 4.6(c) and 4.6(d). The harmonic number in this figure corresponds to the harmonics of 200 Hz (speed of Machine 3).

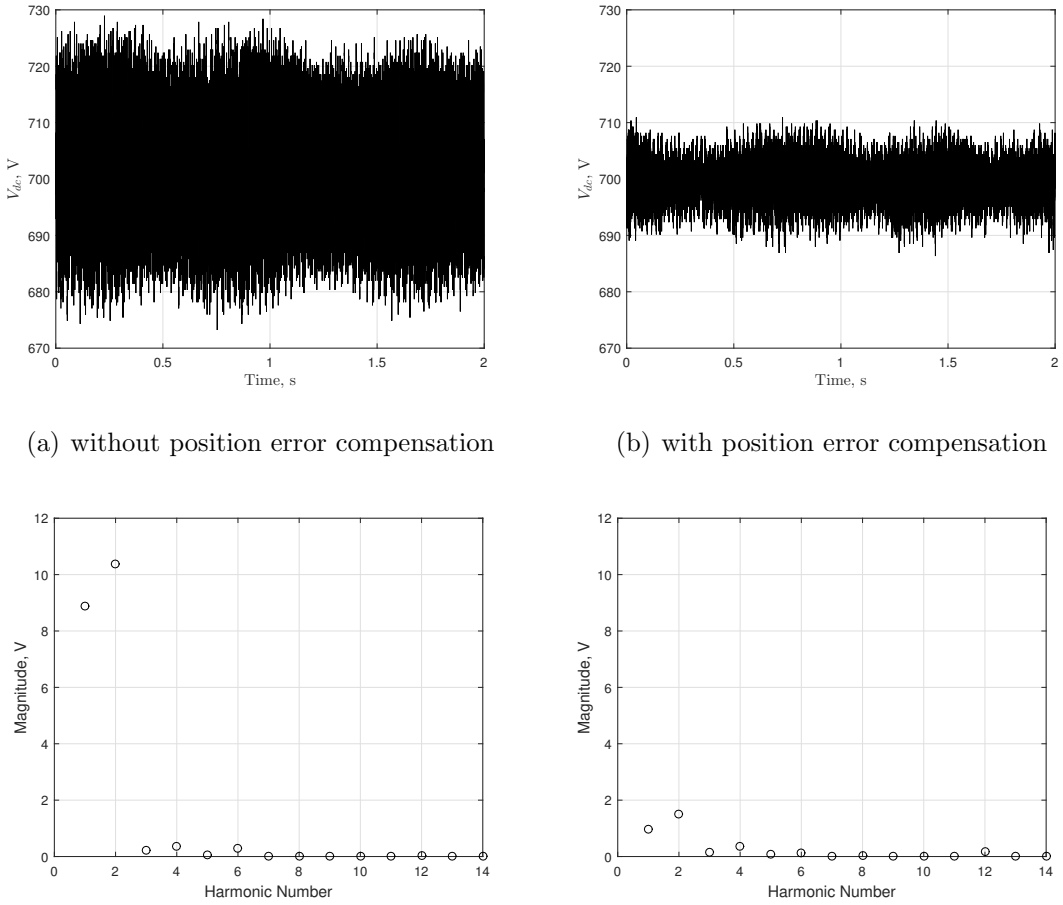

(a) without position error compensation

(b) with position error compensation

(c) without position error compensation

(d) with position error compensation

Fig. 4.6. Impact of position error elimination on dc-link (a), (b) time-domain waveform (c), (d) spectrum: experimental result.

4.2 Variation of Virtual Resistance in Current Regulator

Here, we analyze the impact of position error on dc-link voltage oscillations by varying R_v, which is a virtual resistance parameter used in the CVCR. The analysis is conducted using Model 2 with version 1 of the voltage controller.

4.2.1 Simulation Results

The first set of results shown in Fig. 4.7 are the frequency response plots for both machines 2 and 3 at an arbitrary selected operating point of 6000 rpm (the speeds of both machines are the same) and load torque of 150 Nm. R_v is increased from $5r_s$ to $20r_s$ in the controllers of both machines. Note that increasing R_v increases the integral gains K_{iqd} from (2.149). It is observed from these plots that increasing R_v reduces the dc-link voltage oscillations in the frequency range around the fundamental.

The second set of results is performed over a wide operating range. Rotor speed is the same for both machines, and varies from 2000 to 9000 rpm in steps of 500 rpm. The load torque at each speed is varied in steps of 10 Nm, starting from 50 Nm and ending at the maximum possible torque at that particular speed. The impact of 1° position error at fundamental in both machines is shown in Figs. 4.8(a)–4.8(b) and 4.8(c)–4.8(d) for $R_v = 10r_s$ and $R_v = 20r_s$, respectively. It is observed that the dc-link voltage oscillations reduce as R_v increases (cf. Fig. 3.13, p. 55).

4.2.2 Experimental Results

For this experiment, the Machine 2 (generator) and Machine 3 (motor) are connected to a 700-V dc-link through a dual inverter. The test was conducted at an operating point of 3000 rpm (the speeds of machines 2 and 3 are the same, and are controlled by machines 1 and 4) at 80 kW. The virtual resistance R_v is changed from a value of $4r_s$ to $20r_s$ in the controllers of both machines. The time-domain dc-link voltage waveform is shown in Figs. 4.9(a)–4.9(b). The data has been logged

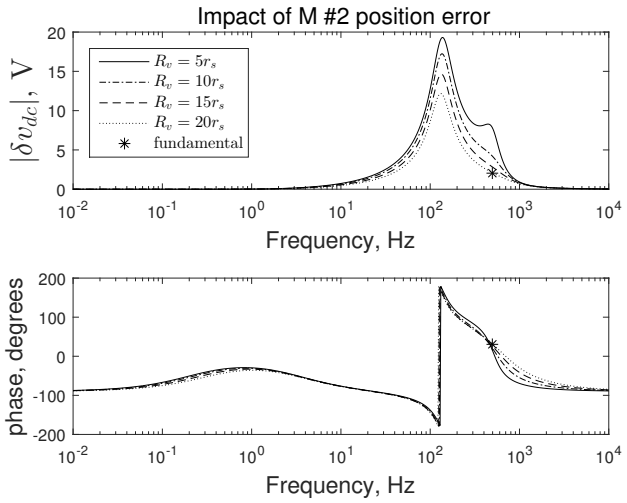

(a)

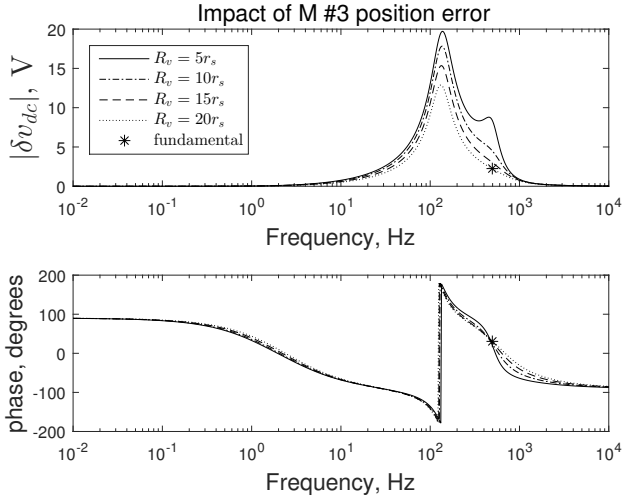

(b)

Fig. 4.7. Impact of increasing virtual resistance on dc-link.

using a Tektronix oscilloscope for 1 s. The spectrum of the dc-link voltage for these waveforms is shown in Figs. 4.9(c)–4.9(d). It can be observed that increasing R_v attenuates the dc-link voltage oscillations at a broad frequency range, as expected from the preceding theoretical analysis.

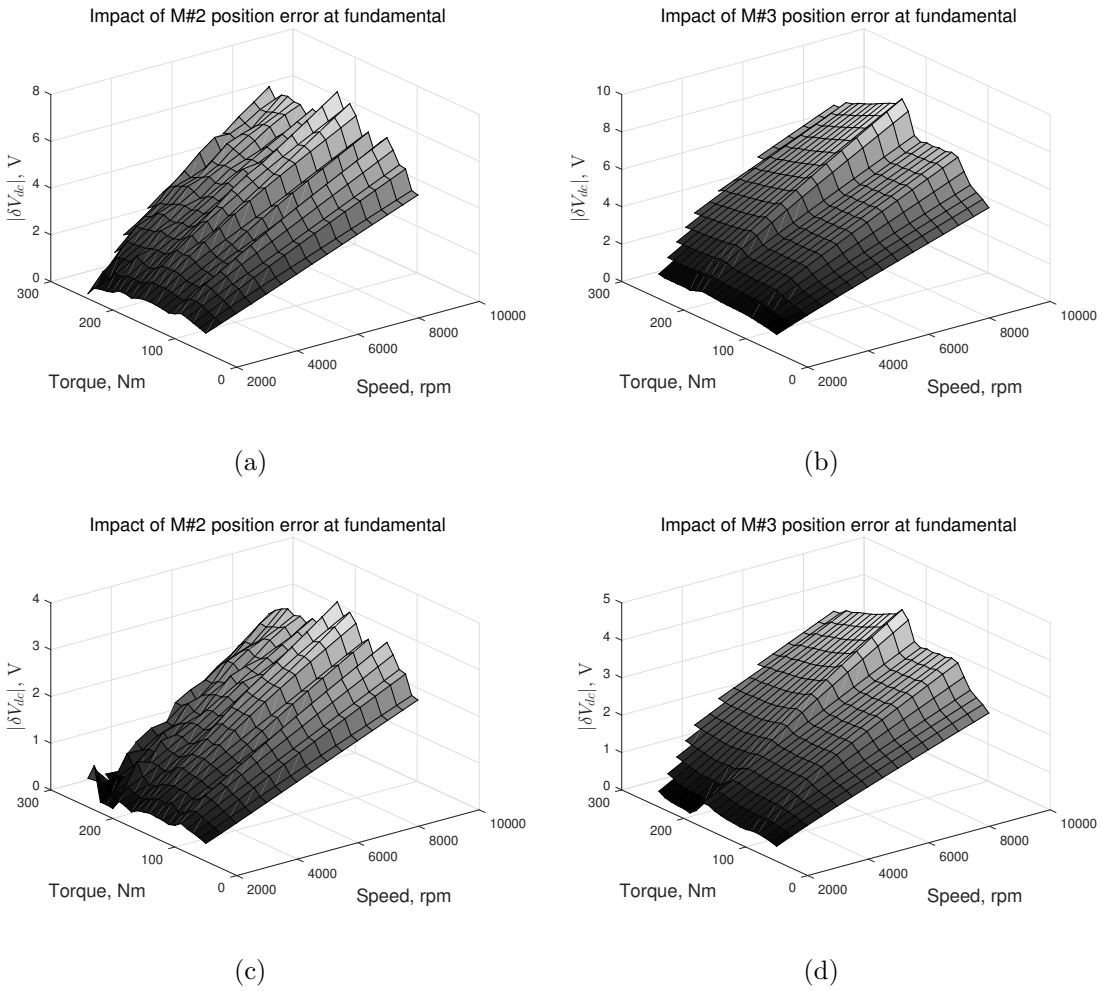

Fig. 4.8. Impact of position error on dc-link when $R_v = 10r_s$ in (a), (b) and $R_v = 20r_s$ in (c), (d).

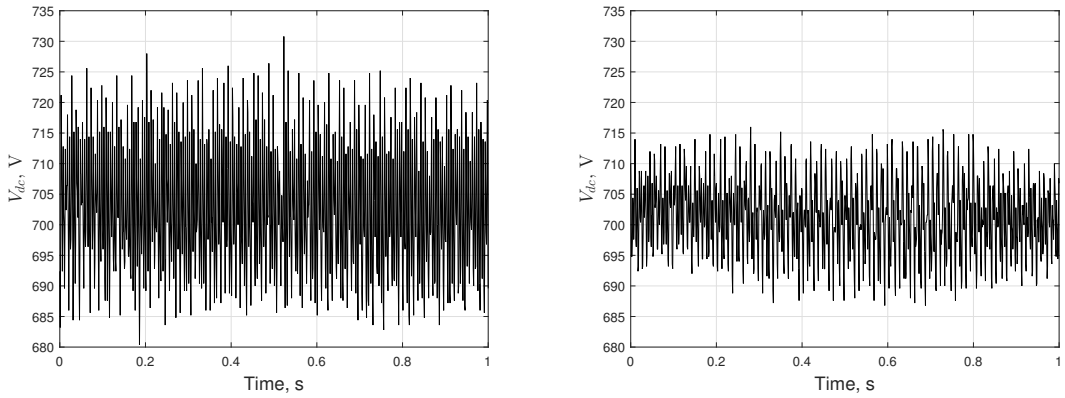

(a) $R_v = 4r_s$

(b) $R_v = 20r_s$

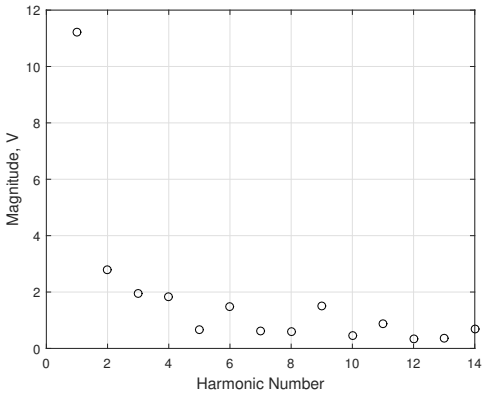

(c) $R_v = 4r_s$

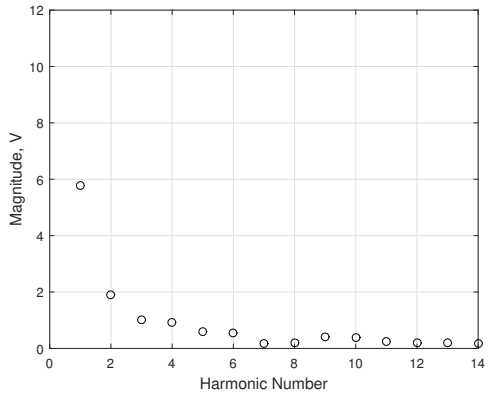

(d) $R_v = 20r_s$

Fig. 4.9. Dc-link voltage (a), (b) time-domain waveform (c), (d) spectrum: experimental result.

4.3 Variation of Current Regulator Bandwidth

In this section, we study the impact of varying the current regulator bandwidth ω_{bi} on the dc-link voltage oscillations. The position error magnitude is kept constant at 1°. The results are obtained using Model 2 with version 1 of the voltage controller.

4.3.1 Simulation Results

The first study is performed at an arbitrary operating point of 3000 rpm (250 Hz fundamental electrical frequency) and 240 Nm load torque. This first set of results is obtained by varying the current regulator bandwidth starting from 80 Hz to 800 Hz, i.e., a frequency that is substantially higher than the fundamental where the disturbance due to position error appears. Note that increasing ω_{bi} increases all the gains of CVCR per (2.149). A positive side-effect of increasing the inner-loop current control bandwidth is that it allows the version-1 voltage control to perform better at higher rotor speeds (see Sec. 2.2). It is observed from Figs. 4.10(a)-4.10(b) that the dc-link voltage oscillations reduce at a frequency range around the fundamental as ω_{bi} increases.

The second set of results in Fig. 4.11 shows the impact over a wide operating range. The bandwidth of the current regulator is set to 1500 Hz, which was chosen to be higher than the highest fundamental frequency in the considered operating range. It is observed that the oscillations reduce when ω_{bi} is increased (cf. Fig. 3.13, p. 55). However, there is a slight increase in dc-link voltage oscillations due to slot harmonics as shown in Fig. 4.12 (cf. Fig. 3.14, p. 56). This behavior can be explained using the transfer function of the tuned current regulator (2.152), p. 38. The increase in bandwidth allows the slot harmonics (especially at lower rotor speeds) to pass through the current regulator, thereby causing a slight increase in dc-link oscillations.

The third set of results is obtained by simulating a case where only the traction drive (Machine 3) is present, and is connected to a constant dc source through an

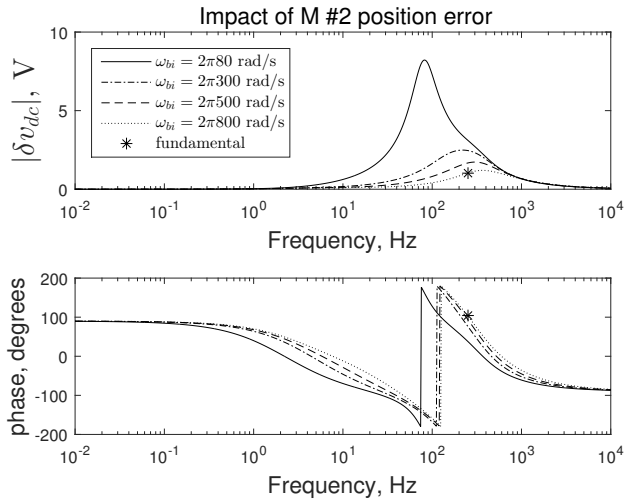

(a)

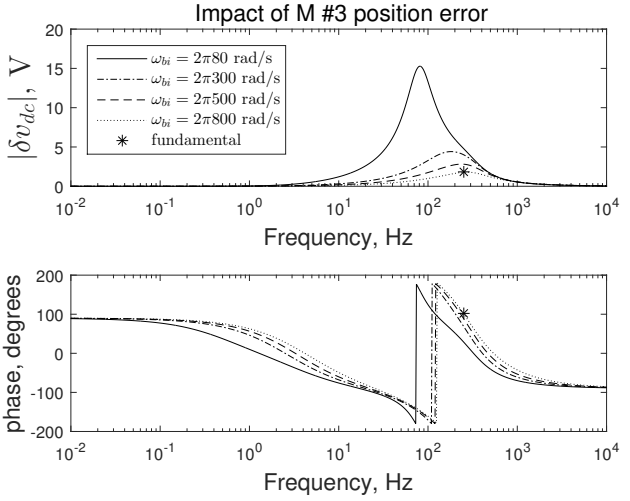

(b)

Fig. 4.10. Impact of current regulator bandwidth on dc-link voltage.

inverter. The selected operating point is 3000 rpm at a load torque of 240 Nm. The power at the machine terminals is

$$P_3 = \frac{3}{2}\left[(v^*_{q30} + \delta v_{q3})(i^*_{q30} + \delta i_{q3}) + (v^*_{d30} + \delta v_{d3})(i^*_{d30} + \delta i_{d3})\right] \tag{4.41}$$

where the equilibrium values of qd voltages and currents are obtained using the initialization process described in Appendix A, and the time-domain δv_{qd} and δi_{qd} are

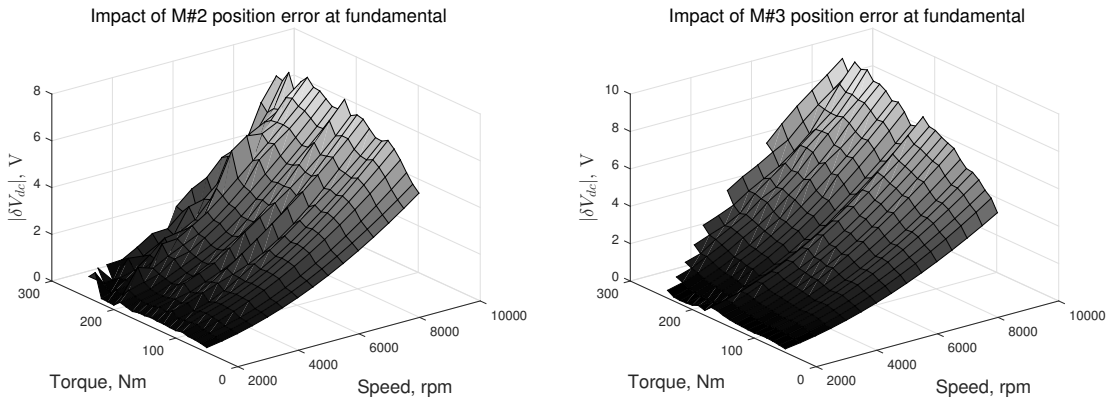

(a) (b)

Fig. 4.11. Impact of position error on dc-link voltage oscillations when current regulator bandwidth is 1500 Hz.

obtained by running the small-signal model in Simulink. A 1° position error is introduced at the fundamental. The spectrum of oscillatory power components at the machine terminals is observed in Fig. 4.13(a). The oscillations in power at fundamental are due to the encoder position error, whereas oscillations of 6^{th} and 12^{th} order are due to the slot harmonics. However, harmonics of 2^{nd}, 5^{th}, 7^{th}, 11^{th}, and 13^{th} order are also observed. This can be explained using (4.41). The interactions between fundamental component and 6^{th} order in voltages and currents leads to 5^{th} and 7^{th} order power components. Similarly, interactions between fundamental and 12^{th} order in voltages and currents leads to 11^{th} and 13^{th} order power components. The oscillations at second harmonic occur due to the interaction of fundamental components in voltages and currents. It is observed that by increasing ω_{bi}, the oscillations in power reduce by a factor of 2–4 at the fundamental frequency; however, the slot harmonics generally increase by a factor of approximately 2. Recall that these power oscillations cause the oscillations on dc-link voltage per (2.4), p. 13. Fig. 4.3.1 depicts the power spectrum when a 1° position error is introduced simultaneously at both the fundamental and second harmonic. The interaction between 2^{nd} order and slot harmonics leads to harmonics of 4^{th}, 8^{th}, and 10^{th} order.

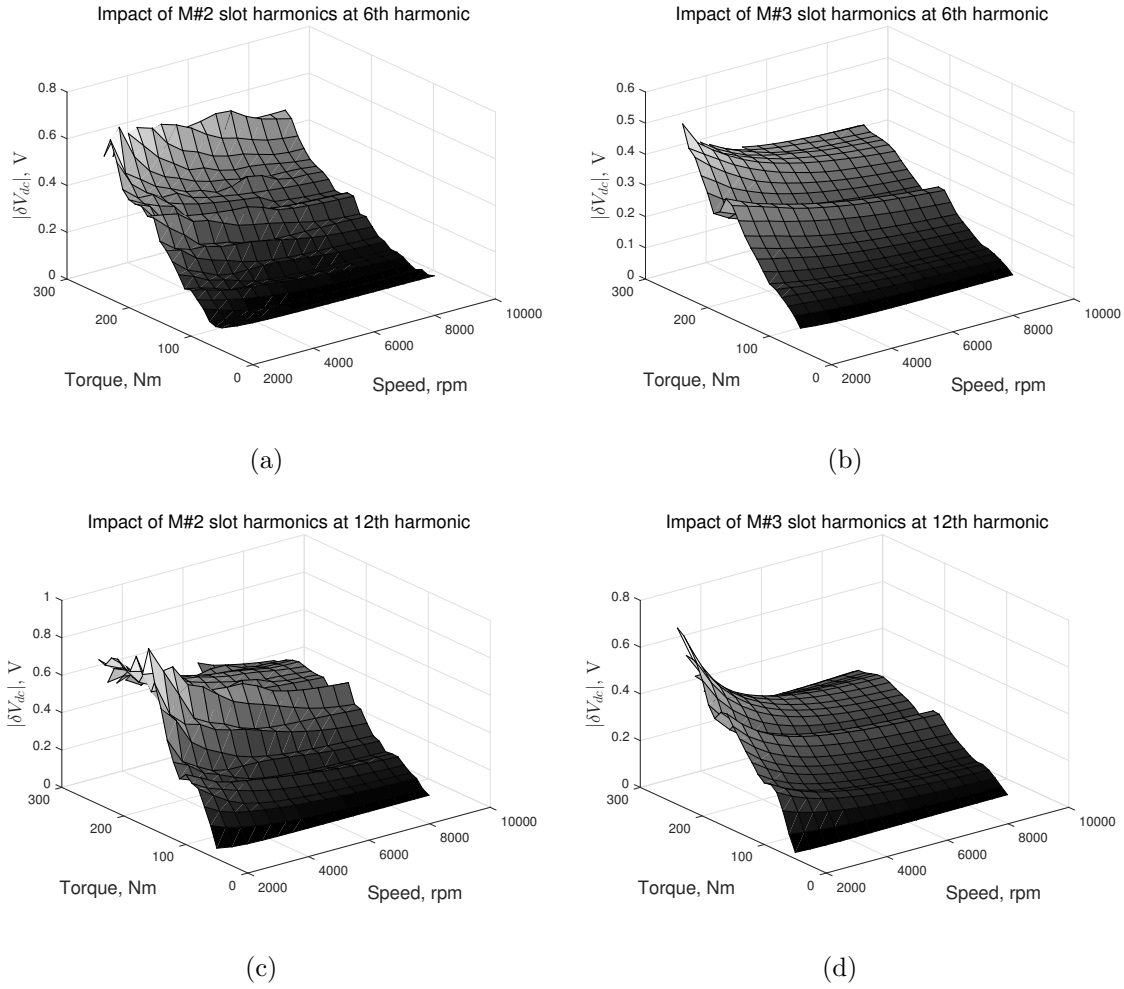

Fig. 4.12. Impact of slot harmonics on dc-link voltage oscillations when current regulator bandwidth is 1500 Hz.

4.3.2 Experimental Results

To verify the impact of changing the current regulator bandwidth experimentally, tests were performed using only a traction drive (Machine 3) connected to a 700-V dc-supply through an inverter. The test was performed at a fundamental frequency of 200 Hz with 240 Nm of load torque (generated by the Machine 3). Here, the three phase voltages and currents are logged to compute the instantaneous power. Note that the phase voltages are logged without filtering any higher harmonics. Three tests are performed at the same operating point by setting the bandwidth of the

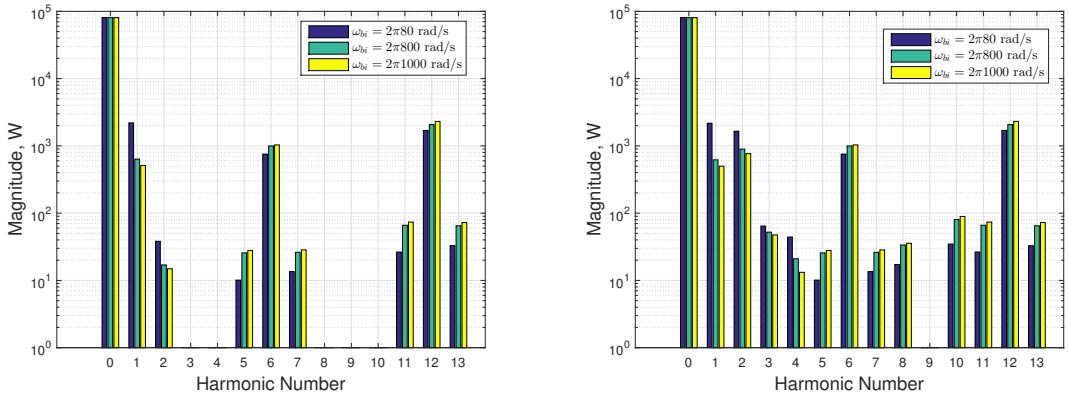

(a)

Fig. 4.13. Power spectrum with increasing ω_{bi} when position error is (a) only at fundamental (b) at both fundamental and second harmonic.

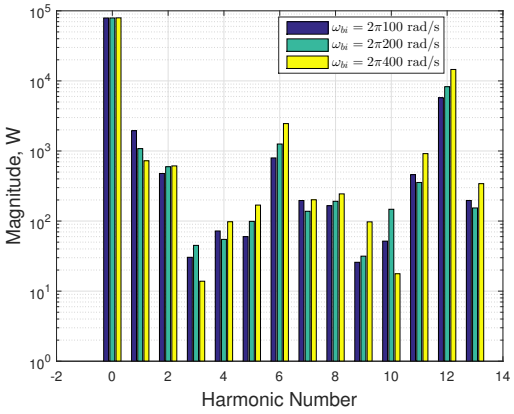

Fig. 4.14. Impact of increasing ω_{bi}: experimental result.

current regulator to 100 Hz, 200 Hz, and 400 Hz. The spectrum of the power at the machine terminals for these three cases is shown in Fig. 4.14. It is observed that the fundamental component in the power reduces at the cost of increasing components at higher frequencies, as expected from the simulation results.

5. CONCLUSIONS

This research has set forth three methods to address the problem of dc-link voltage oscillations caused by VR resolvers. The techniques proposed herein to reduce the impact of position error are not specific to any particular manufacturing imperfection in the resolver. Comparing with the earlier works [15], [16] in this domain, the proposed techniques are easier to implement as they do not involve any modifications to be performed in the R/D, and also do not require LUT methods. A notable advantage of the position error elimination technique is that it can be employed to eliminate any desired harmonic component present in the position error. In addition, the proposed methods of eliminating the position error and increasing the virtual resistance can be implemented simultaneously for more efficient reduction of dc-link oscillations.

Though this research was mainly focused on mitigating the dc-link oscillations caused solely due to resolver error, the impact of other possible external disturbances on the system has been analyzed, and it has been concluded that the position error has the most significant impact compared to other disturbances.

The approach followed in this work suggests several research avenues. A further improvement is to model the inverter, Machine 1 (prime mover) and Machine 4 (load) for more accurate analysis, as this work assumes an average-value model and models only Machine 2, Machine 3, and the dc-link. The position errors in all four machines can be accounted to observe the dc-link oscillations. It would be interesting to observe the impact of torque oscillations due to resolver error and also compute the rotor shaft oscillations using the mechanical dynamics of the system. Ultimately, the rotor shaft oscillations can be tied to resolver error for a more precise analysis.

The method of varying virtual resistance can be investigated a little further with respect to its limitations. Increasing the virtual resistance of current regulator to a

very large value shifts the poles of the regulator to far left side of s-plane. This might introduce high frequency components into the system. So, one could concentrate on analyzing the impact of noise obtained from the measurements on the dc-link voltage.

In regard with the practical implementation of the proposed techniques, a thorough validation should be done by conducting the tests over the entire operating range.

LIST OF REFERENCES

LIST OF REFERENCES

[1] D. Murthy-Bellur, E. Ayana, S. Kunin, B. Palmer, and S. Varigonda, "WBG inverter for commercial power generation and vehicle electrification," in *2015 IEEE International Workshop on Integrated Power Packaging (IWIPP)*, pp. 36–39, May 2015.

[2] A. Murray, B. Hare, and A. Hirao, "Resolver position sensing system with integrated fault detection for automotive applications," in *Proceedings of IEEE Sensors*, vol. 2, pp. 864–869 vol.2, 2002.

[3] D. Hanselman, "Resolver signal requirements for high accuracy resolver-to-digital conversion," in *, 15th Annual Conference of IEEE Industrial Electronics Society*, pp. 486–493 vol.2, Nov. 1989.

[4] T. Emura, L. Wang, M. Yamanaka, and H. Nakamura, "A high-precision positioning servo controller based on phase/frequency detecting technique of two-phase-type PLL," *IEEE Transactions on Industrial Electronics*, vol. 47, pp. 1298–1306, Dec. 2000.

[5] R. Hoseinnezhad, "Position sensing in brake-by-wire callipers using resolvers," *IEEE Transactions on Vehicular Technology*, vol. 55, pp. 924–932, May 2006.

[6] Q. Lin, T. Li, and Z. Zhou, "Error Analysis and Compensation of the Orthogonal Magnetic Encoder," in *2011 First International Conference on Instrumentation, Measurement, Computer, Communication and Control*, pp. 11–14, Oct. 2011.

[7] R. Ramakrishnan, A. Gebregergis, M. Islam, and T. Sebastian, "Effect of position sensor error on the performance of PMSM drives for low torque ripple applications," in *2013 International Electric Machines Drives Conference*, pp. 1166–1173, May 2013.

[8] X. Ge, Z. Q. Zhu, R. Ren, and J. T. Chen, "Analysis of Windings in Variable Reluctance Resolver," *IEEE Transactions on Magnetics*, vol. 51, pp. 1–10, May 2015.

[9] N. Hagiwara, Y. Suzuki, and H. Murase, "A method of improving the resolution and accuracy of rotary encoders using code compensation technique," in *[1991] Conference Record. IEEE Instrumentation and Measurement Technology Conference*, pp. 183–184, May 1991.

[10] D. C. Hanselman, "Techniques for improving resolver-to-digital conversion accuracy," *IEEE Transactions on Industrial Electronics*, vol. 38, pp. 501–504, Dec. 1991.

[11] K. K. Tan, H. X. Zhou, and T. H. Lee, "New interpolation method for quadrature encoder signals," *IEEE Transactions on Instrumentation and Measurement*, vol. 51, pp. 1073–1079, Oct. 2002.

[12] J.-C. Kim, J.-M. Kim, C.-U. Kim, and C. Choi, "Ultra precise position estimation of servomotor using analog quadrature encoders," in *Twenty-First Annual IEEE Applied Power Electronics Conference and Exposition, 2006. APEC '06.*, pp. 5 pp.–, Mar. 2006.

[13] S. H. Hwang, H. J. Kim, J. M. Kim, L. Liu, and H. Li, "Compensation of Amplitude Imbalance and Imperfect Quadrature in Resolver Signals for PMSM Drives," *IEEE Transactions on Industry Applications*, vol. 47, pp. 134–143, Jan. 2011.

[14] H. S. Mok, S. H. Kim, and Y. H. Cho, "Reduction of PMSM torque ripple caused by resolver position error," *Electronics Letters*, vol. 43, pp. 646–647, May 2007.

[15] N. Noori and D. A. Khaburi, "Diagnosis and compensation of amplitude imbalance, imperfect quadrant and offset in resolver signals," in *2016 7th Power Electronics and Drive Systems Technologies Conference (PEDSTC)*, pp. 76–81, Feb. 2016.

[16] J. Lara, J. Xu, and A. Chandra, "A Novel Algorithm Based on Polynomial Approximations for an Efficient Error Compensation of Magnetic Analog Encoders in PMSMs for EVs," *IEEE Transactions on Industrial Electronics*, vol. 63, pp. 3377–3388, June 2016.

[17] J. Wells and M. Amrhein, "Adaptive resolver compensation controller," Jan. 22 2009. WO Patent App. PCT/US2008/070,009.

[18] P. C. Krause, O. Wasynczuk, S. D. Sudhoff, and S. Pekarek, *Analysis of Electric Machinery and Drive Systems*. IEEE Press, Wiley, 2013.

[19] F. Briz, M. W. Degner, and R. D. Lorenz, "Analysis and design of current regulators using complex vectors," *IEEE Transactions on Industry Applications*, vol. 36, pp. 817–825, May 2000.

[20] P. J. Antsaklis and A. N. Michel, *Linear Systems*. New York: McGraw–Hill, 1997.

[21] H. Kim and R. D. Lorenz, "A virtual translation technique to improve current regulator for salient-pole AC machines," in *IEEE 35th Annual, Power Electronics Specialists Conference, PESC*, vol. 1, pp. 487–493 Vol.1, June 2004.

APPENDICES

A. MOTOR CHARACTERIZATION

The machine used in this research is a Remy HVH250-115D machine which is rated at 200 kW and 425 A rms stator current. This appendix sets forth a method to obtain the map of qd currents to stator flux linkages and electromagnetic torque. The method is based on running a series of simulations using a JMAG (FEA) machine model. First, we define an operating range in terms of qd currents. To obtain these, the machine is connected to three dc voltage sources of appropriate magnitude. The JMAG model is simulated using the calculated abc voltages as inputs, with the rotor locked at a particular position. We wait until the steady state is reached to extract the flux linkages and electromagnetic torque from the JMAG model. This process is repeated for all qd currents spanning the complete operating range and at all rotor positions spanning a complete electrical revolution.

A.1 Flux Linkage and Torque

The steady-state circuit representing a case where dc voltage sources are connected to the stator windings is shown in Fig. A.1. In the JMAG model, the motor is Y-connected without neutral wire. Here, we calculate the input dc voltages, E_1, E_2, and E_3, to obtain given qd currents. Applying Kirchhoff's voltage law twice, we get

$$\begin{bmatrix} 1 & -1 & 0 \\ 0 & 1 & -1 \\ 1 & 1 & 1 \end{bmatrix} \begin{bmatrix} v_{as} \\ v_{bs} \\ v_{cs} \end{bmatrix} = \begin{bmatrix} 1 & -1 & 0 \\ 0 & 1 & -1 \\ 0 & 0 & 0 \end{bmatrix} \begin{bmatrix} E_1 \\ E_2 \\ E_3 \end{bmatrix} \tag{A.1}$$

where we have also used the fact that the $v_{as} + v_{bs} + v_{cs} = 0$ in a Y-connected motor (this becomes the third equation). This leads to

$$v_{abcs} = \frac{1}{3}\begin{bmatrix} 2 & -1 & -1 \\ -1 & 2 & -1 \\ -1 & -1 & 2 \end{bmatrix} E_{123}\,. \tag{A.2}$$

The matrix in (A.2) is not invertible. But once we introduce an additional equation for the sum $E_1 + E_2 + E_3$, we can solve for the source voltages. In general, we are free to select sources such that $E_1 + E_2 + E_3 \neq 0$. Nevertheless, here, we choose $E_3 = -E_1 - E_2$. Manipulating the above equation using this relation yields

$$v_{abcs} = \begin{bmatrix} 1 & 0 \\ 0 & 1 \\ -1 & -1 \end{bmatrix} E_{12}\,. \tag{A.3}$$

Therefore, the input dc voltage sources to obtain desired qd currents are given by

$$E_1 = v_{as} = r_s\left[i_{qs}\cos\theta_r + i_{ds}\sin\theta_r\right] \tag{A.4}$$

$$E_2 = v_{bs} = r_s\left[i_{qs}\cos\left(\theta_r - 2\pi/3\right) + i_{ds}\sin\left(\theta_r - 2\pi/3\right)\right] \tag{A.5}$$

$$E_3 = v_{cs} = -v_{as} - v_{bs} \tag{A.6}$$

where we have applied the inverse qd transformation to obtain i_{as} and i_{bs}.

We run a series of JMAG studies with qd currents spanning the complete operating range and rotor position spanning an electrical revolution. The pseudo-code of this process is outlined below:

Specify coil temperature T_c and magnet temperature T_{pm}.
for (some value of $\theta_r \in \mathbf{\Theta}_r$)
  for (some value of $i_{qs} \in \mathbf{I}_{qs}$)
    for (some value of $i_{ds} \in \mathbf{I}_{ds}$)
      % using (A.4)-(A.6)
      $E_1 = v_{as} = r_s[i_{qs}\cos\theta_r + i_{ds}\sin\theta_r]$

$E_2 = v_{bs} = r_s[i_{qs}\cos(\theta_r - 2\pi/3) + i_{ds}\sin(\theta_r - 2\pi/3)]$

$E_3 = v_{cs} = -v_{as} - v_{bs}$

`sim('model')` % wait until dc steady state

% extract final values of λ_{abcs} from JMAG model

% transform into qd variables

$$\lambda_{qd}(i_q, i_d, \theta_r) = \tfrac{2}{3}\begin{bmatrix}\cos\theta_r & \cos(\theta_r - 2\pi/3) & \cos(\theta_r - 4\pi/3)\\ \sin\theta_r & \sin(\theta_r - 2\pi/3) & \sin(\theta_r - 4\pi/3)\end{bmatrix}\lambda_{abcs}$$

% extract $T_e(i_q, i_d, \theta_r)$ from JMAG model

$\boldsymbol{\Theta}_r$ is an $n \times 1$ vector of equally-spaced electrical rotor angles spanning the interval $[0, 2\pi)$. $\mathbf{I}_{qs}$ (Matlab symbol: `iqs_vec`) is a 93×1 vector of equally-spaced q-axis currents spanning an interval $[-460, 460]$ and $\mathbf{I}_{ds}$ (Matlab symbol: `ids_vec`) is a 69×1 vector of equally-spaced d-axis currents spanning an interval $[0, -680]$.

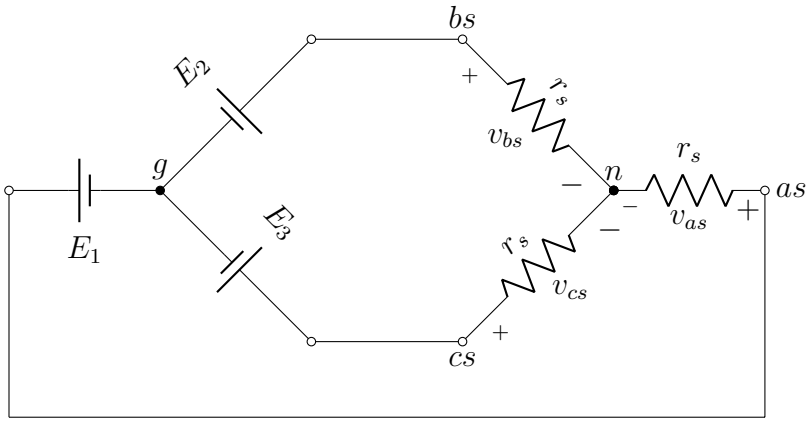

Fig. A.1. Steady-state circuit diagram of stator coils connected to three dc voltage sources.

The averages of qd-axis flux linkages $\bar{f}_{qd}(i_q, i_d)$ and electromagnetic torque $\overline{T}_e(i_q, i_d)$ (Matlab symbol: `Te_avg`) are obtained by taking the mean of $\lambda_{qd}(i_q, i_d, \theta_r)$ and $T_e(i_q, i_d, \theta_r)$ over an electrical revolution, for example:

$$\bar{f}_q(i_q, i_d) = \frac{1}{n} \sum_{k=1}^{n} \lambda_q(i_q, i_d, \theta_{r,k}) \,. \tag{A.7}$$

The variation of average flux linkages and electromagnetic torque with qd currents is shown in Fig. A.2.

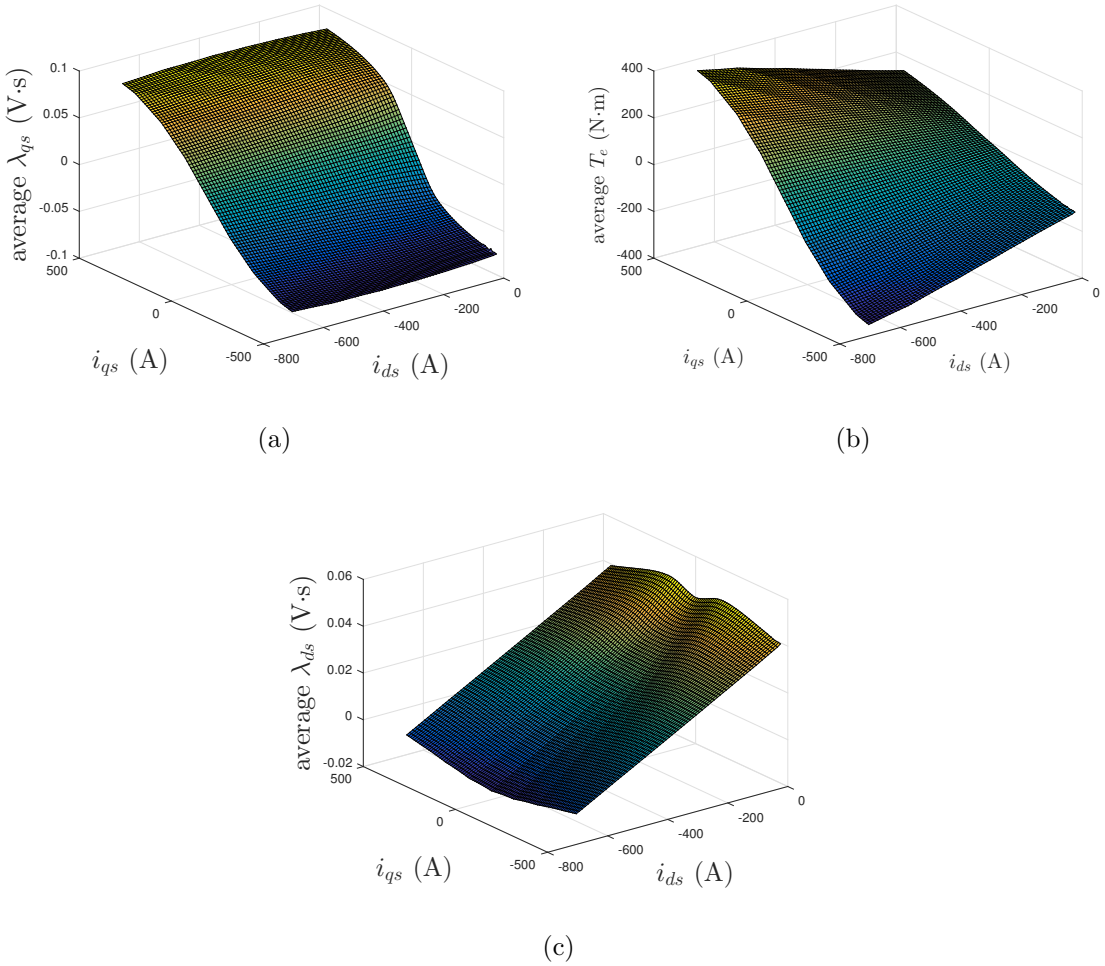

Fig. A.2. Average qd flux linkages and electromagnetic torque over the complete operating range.

A.2 Calculation of *qd* Current Commands

In this section, we outline the procedure for computing an optimum pair of *qd* currents that generate a given electromagnetic torque (T_e) at a particular rotor speed (ω_r). This yields the maximum torque per ampere (MTPA) curve. However, at higher speeds, the operation is constrained by voltage limits, and the obtained currents deviate from the nominal MTPA characteristic. The procedure is outlined as follows:

1. Extract pairs of *qd* currents (Matlab symbol: `iqd`) for the given torque (Matlab symbol: `Te`) using the torque map (obtained from motor characterization):

   `iqd = contour(ids_vec, iqs_vec, Te_avg, [Te Te])`.

2. Compute the corresponding *qd* voltages using the *qd* currents (obtained in above step) and the average flux-linkages (obtained from motor characterization): e.g, $v_q = r_s i_q + \omega_r \bar{f}_d(i_q, i_d)$.

3. Find the peak value of the stator current for all the pairs of *qd* currents lying on the contour:

   `Is_vec = sqrt(iq^2+id^2)`.

4. Find the pair of *qd* currents corresponding to the minimum peak stator current:

   `[Is_min,ind] = min(Is_vec)`;

   `iqd_mtpa = iqd(ind)`.

5. Identity the voltages v_{qdm} corresponding to `iqd_mtpa` and compute the peak value of the voltage: $v_s = \sqrt{v_{\text{qm}}^2 + v_{\text{dm}}^2}$.

6. Verify if this pair of *qd* currents (`iqd_mtpa`) satisfy the voltage constraint, i.e, $v_s <= v_{dc0}/\sqrt{3}$. Note that the *qd* voltages are computed in step (2).

   (a) If the voltage limit is satisfied, the optimum value of *qd* currents for the given speed and torque are the ones obtained in step 4.

   (b) If the voltage limit is violated, identify the `iqd` of smallest magnitude that satisfies the voltage constraint.

From the above study, we find the following:

1. Maximum allowable torque $T_{\max}$ (Matlab symbol: `Tmax`) vs. commanded rotor speed ω_r^* (Matlab symbol: `wrstar`) for MTPA control. The speed range provided is 500–10,000 rpm in steps of 500 rpm.
2. A 2-D mapping from commanded torque percentage $T_{e,pc}^*$ (Matlab symbol: `Testarpc`) and commanded rotor speed (`wrstar`), to commanded currents i_{qd}^* (Matlab symbols: `iqstar`, `idstar`, 2-D arrays). This mapping is based on the definition of commanded torque percentage,

$$T_{e,pc}^* = \frac{T_e^*}{T_{\max}(\omega_r^*)} \times 100 \tag{A.8}$$

   which is provided in steps of 2%.

A.3 Initialization Process

In this section, we describe the initialization process (in Matlab pseudo-code form) to compute steady-state values for any arbitrary operating point:

1. Input parameters: rotor speed of each machine and load torque (Matlab symbol: `Tload`) of motor 3.
2. Set parameters for both machines, e.g., resistance of coil, number of poles, etc., and for dc-link, e.g., capacitance.
3. Set the PI gains for CVCR in each machine (dependence on commanded speed).
4. Load steady-state data (section A.2) to set the operating points for each machine.
5. Compute equilibrium point for Machine 3:
   (a) Find $T_{\max,3}$ for the given commanded rotor speed ω_{r3}^* using linear interpolation:
   `Tmax3 = interp1(wrstar,Tmax,wr3star);`
   (b) Extract set of machine #3 MTPA currents $i_{qd3,mtpa}$ (Matlab symbols: `iq3_mtpa`, `id3_mtpa`, 1-D array) at the given commanded speed for the complete torque

range using 2-D linear interpolation:

```
torquepc = linspace(0,100,1000);
iq3_mtpa = interp2(wrstar,Testarpc,iqstar,wr3star,torquepc);
id3_mtpa = interp2(wrstar,Testarpc,idstar,wr3star,torquepc);
```

Also, compute the torque values $T_{3,mtpa}$ (Matlab symbol: `T3_mtpa`) for corresponding MTPA currents:

```
T3_mtpa = torquepc * Tmax3/100;
```

(c) Obtain polynomial g_{qd} functions (2.30)-(2.31) by curve fitting $i_{q3,mtpa}$ vs. $T_{3,mtpa}$ and $i_{d3,mtpa}$ vs. $T_{3,mtpa}$ for the given speed. [1] The following script for g_q is generated from the curve fitting toolbox in Matlab:

```
ft = fittype('poly4');
opts = fitoptions('Method','LinearLeastSquares');
opts.Lower = [-Inf -Inf -Inf -Inf 0];
opts.Upper = [Inf Inf Inf Inf 0];
[g_q, ~] = fit(T3_mtpa,iq3_mtpa,ft,opts);
coefs_q = coeffvalues(g_q);
```

Similarly, compute g_d.

(d) Find qd currents using g_{qd} functions based on load torque.

```
iq3_0 = polyval(coefs_q,Tload);
id3_0 = polyval(coefs_d,Tload);
```

(e) Compute qd voltages using currents and flux-linkages (obtained from JMAG parameter characterization study) and based on steady-state voltage equations, e.g, $v_{q0} = r_s i_{q0} + \omega_{r0} \bar{f}_d(i_{q0}, i_{d0})$.

(f) Compute stator power P_{30} using voltages and currents, e.g., $P_{30} = 1.5(v_{q0} i_{q0} + v_{d0} i_{d0})$.

6. Compute equilibrium point for Machine 2:

(a) Repeat step (5b) for `wr2star` to obtain MTPA currents and torques.

[1] $T_e^* = 0$ implies $i_q^* = 0$ and $i_d^* = 0$ for MTPA control at all commanded rotor speeds from steady-state data (section A.2).

(b) Power required by machine 2 is computed by $P_{20} = -P_{30}/\eta^2 - Gv_{dc0}^2/\eta$, where η is the efficiency of the inverter.

(c) A bisection algorithm is used to find the q-axis current that corresponds to P_{20}. First, we compute the d-axis current corresponding to a given q-axis current using the MTPA mapping $i_d^*(i_q^*)$:

`id2star = interp1(iq2_mtpa,id2_mtpa,iq2star);`

Then power is calculated similarly to (5e) and (5f). Hence, $P_{20} = f(i_{q2}^*)$, i.e., a single-variable function.

(d) The equilibrium value of torque T_{e20} is computed by

`Te2_0 = interp1(iq2_mtpa,T2_mtpa,iq2_0)`.

B. SYSTEM PARAMETERS

The following parameters are used in the simulations that were conducted to analyze the drivetrain.

Table B.1
List of System Parameters

Parameters	**Values**
Number of pole pairs ($pp_2 = pp_3$)	5
dc-link voltage (v_{dc0})	700 V
dc-link capacitance (C)	500 μF
dc-link admittance (G)	0.1 mS
Stator resistance (r_s)	0.0155 Ω
Virtual admittance (G_a)	1 mS
Permanent magnet flux linkage (λ_f)	0.0456 V·s
Voltage regulator bandwidth (ω_{bv}) (for version 2)	$2\pi 20$ rad/s
Efficiency of inverter (η)	0.95

C. TRIGNOMETRIC IDENTITIES

$$\cos A - \cos B = -2 \sin\left(\frac{A+B}{2}\right) \sin\left(\frac{A-B}{2}\right) \tag{C.1}$$

$$\sin A - \sin B = 2 \cos\left(\frac{A+B}{2}\right) \sin\left(\frac{A-B}{2}\right) \tag{C.2}$$

$$\cos A \cos B = \frac{1}{2}[\cos(A+B) + \cos(A-B)] \tag{C.3}$$

$$\sin A \cos B = \frac{1}{2}[\sin(A+B) + \sin(A-B)] \tag{C.4}$$

$$\sin A \sin B = \frac{1}{2}[\cos(A-B) - \cos(A+B)] \tag{C.5}$$